# Development of X-ray Reflectivity Imaging to Visualize Buried Functional Interfaces in Ultrathin Films

# Development of X-ray Reflectivity Imaging to Visualize Buried Functional Interfaces in Ultrathin Films

Jinxing Jiang

February 2017

# Development of X-ray Reflectivity Imaging to Visualize Buried Functional Interfaces in Ultrathin Films

Jinxing Jiang

Doctoral Program in Materials Science and Engineering

Submitted to the Graduate School of

Pure and Applied Sciences

in Partial Fulfillment of the Requirements

for the Degree of Doctor of Philosophy in

Engineering

at the

University of Tsukuba

# Acknowledgements

First and foremost I would like to express my sincere gratitude to my advisor Prof. Kenji Sakurai for the continuous support of my Ph.D. study, for his patience, motivation, enthusiasm and immense knowledge. He is such a great scientist and a wonderful mentor who has not only taught me to do researches, but also guided me to enjoy sciences. Prof. Kenji Sakurai always encouraged me to learn new knowledge, develop new instruments and do original works. Because of his support, I was able to attend plenty of domestic and international conferences and access to state-of-the-art facilities. Prof. Kenji Sakurai always motivated that excellence can be achieved by being pro-active and preparing experiments, presentations, and papers much ahead of time. His guidance helped me in all the time of research and preparation of this thesis.

My sincere thanks also go to the rest of my thesis committee Prof. Yoshihiko Takeda, Prof. Jie Tang, Prof. Akira Uedono and Prof. Wataru Yashiro, not only for their time, insightful comments and encouragement, but also for the hard questions which incented me to polish my thesis from various perspectives. Special thanks to Prof. Jie Tang, who firstly introduced me to my supervisor when I was seeking a Ph.D. position.

I gratefully acknowledge National Institute for Materials Science for providing the Graduate Research Assistantship, without this financial assistance I won't be able to come here to Japan to obtain my Ph.D. degree.

I would like to thank Dr. Keiichi Hirano who provided many supports and helped preparing X-ray reflectivity imaging experiments at BL14B, Photon Factory. I would also like to thank Dr. Mari Mizusawa from CROSS-Tokai, J-PARC who gave me many useful suggestions and encouragement.

Many thanks to the group members I have had pleasure to work with, Wenyang Zhao, Haruya Kobayashi, Yuwei Liu, Teerakorn Kongkaew, Megumi Iwamoto, Daniel Ginter, Yumi Katasyo, Suvdaa Chimed, Emmanuel Delattre, Kyle McElhinny, Bui Ha Ngoc, Dan Li, Yen Pham Duc Huyen, Honoka Obata. Life in Tsukuba became more colourful with such international labmates.

This thesis is especially dedicated to my family: To my parents Jingxi Jiang and Xuejun Wang, who have raised me, supported me and encouraged me to realize my dreams. To my wife Fen Xue, whose trust, love and support give me strength and sustain me throughout all the hardships.

# Abstract

The interfaces are omnipresent in nature and in many cases give the functions of materials. In order to understand the static structure or dynamic 'change' at the interfaces, visualization of those buried functional interfaces is of great importance. This thesis starts with the pattern formation at ultrathin films and the interfacial structure investigation between adhesives and adherends. Liesegang patterns have been successfully obtained in ultrathin films by temperature control and introduction of equilibrium water vapor in the sample environment. The adhesive / adherend interface structures have been proven to be accessible by X-ray reflectivity. In order to achieve comprehensive understanding, both materials researches urgently demand for an imaging technique to visualize heterogeneous interface. The second (main) part of this thesis is devoted to the details of the original X-ray reflectivity (XRI) imaging system including instrumentation and computer software development. (1) With a collimated monochromatic synchrotron X-ray beam of 0.05 mm (H) × 8 mm (V), the intensity profile of X-ray reflection projection has been taken at many different in-plane rotation angles, from 0 to 180 deg. We have succeeded in visualizing buried layers and interfaces of the 8 mm dia area with the spatial resolution of better than 20 micron. Because of the high brilliance of synchrotron radiation, the typical measuring time is shorter than 1 min. Three analytical cases have been discussed, i. imaging of a buried layer and interface covered by a protection layer, ii. distinguish of different local parts of different thickness in ultrathin film, and iii. selective imaging of specific metal in the thin film form. (2) In addition, we describe that by combining in-plane angle scan and grazing incident angle scan, it is possible to reconstruct a series of interface sensitive X-ray reflectivity images at different grazing incident angles (proportional to wavevector transfers). The physical meaning of a reconstructed X-ray reflectivity image at a specific wavevector transfer is the 2D reflectivity distribution of the sample, in that manner it is possible to retrieve the micro X-ray reflectivity (where the pixel size is in micro-scale) profiles at different local positions of the sample. (3) The instrumental details of a compact X-ray reflectivity imager employing laboratory micro focus X-ray source is also described. Though the power of X-ray source is only 15 W, it works well. The calibration of the system has been discussed, because it is particularly important for the present grazing incidence geometry. We also give a visualization example of the buried interface, physical meaning of the reconstructed image and discuss about possibilities of improvement.

# Contents

## Part II. Original X-ray reflectivity imaging technique

# List of Figures

# List of Tables

# Chapter 1 Introduction

The significance of interfaces cannot be overstated, with their ubiquity from hardware of the information age to the processes of life[1]. The unique molecular and atomic features of the interfaces between materials often control the useful functions of both naturally occurring and synthetic structures[2,3]. Interfaces play vital roles in various systems as diverse as the rate and specificity of electrochemical processes, the adhesive strength and conductivity of thin metal-film coatings on polymer in an electronic circuit component, the compatibility of a biological implant, the efficiency of a semiconductor transistor with a chemically modified interface, and the corrosion of a structural metal induced by its working environment. Understanding the static structure or dynamic 'change' at the interfaces will help us solve many problems such as to improve cycle life in batteries, to improve adhesion between composite materials, and even to mimic matter transportation through cell membrane.

Visualization of those buried functional interfaces is of great importance. X-ray reflectivity is a powerful technique for studying buried interfaces in ultrathin films[4–8]. Howbeit routine X-ray reflectivity assumes that the sample to be measured is in-plane homogeneous, which is not the case in many structures. In that manner imaging capabilities are essential for modern interfaces characterizations, yet only a few X-ray techniques[9–11] have been developed for imaging interfaces in past decades. In order to help to fill the blank, original X-ray reflectivity (XRI) imaging system including instrumentation and image reconstruction softwares has been developed by X-ray Physics Laboratory in NIMS.

The research aim of this PhD thesis is the development of the X-ray reflectivity imaging (XRI) technique, which is able to visualize buried functional interfaces in ultrathin films. The method is based on X-ray reflectivity (XR), which is powerful in characterizing and understanding interfacial structures in ultrathin films because X-rays are capable of penetrating through matter non-destructively and it have atomic scale in-depth resolution due to the small wavelength and the employment of interference effect. Compared with other imaging techniques, the novel XRI possesses large scale viewing area and tunable imaging depth fashion by introducing image reconstruction scheme to ordinary XR. The thesis is divided into two main parts. Part I is dedicated to the exploration of buried functional interfaces including two main chapters: Chapter 2, formation of ultrathin Liesegang pattern, which describes the method and mechanism to prepare the self-organized patterns in ultrathin films. Such nano rings fabrication in ultrathin films by self assembly scheme can be employed to prepare functional patterned interfacial structures; Chapter 3, The adhesive / adherend interface structures have been proven to be accessible by X-ray reflectivity. Part II is the main purpose of this PhD thesis, namely the development of the X-ray reflectivity imaging system that is suitable for non-destructive imaging of buried functional interfaces in ultrathin films including five main chapters: Chapter 4 describes the theoretical background of X-ray reflectivity imaging including short introduction of routine X-ray reflectivity, novel X-ray reflectivity imaging approach and algorithms for image reconstruction from projections ; Chapter 5 discusses X-ray reflectivity imaging implemented in synchrotron radiation X-rays covering the instrumentation and detailed

deomonstrations and discussions of XRI images; Chapter 6 describes that by combining in-plane angle scan and grazing incident angle scan, it is possible to reconstruct a series of interface sensitive X-ray reflectivity images with different in-depth sensitivity at different grazing incident angles; Chapter 7 gives the instrumental details of a compact X-ray reflectivity imager employing laboratory micro focus X-ray source. Chapter 8 summarizes the important findings of this thesis. There is also an appendix included listings python computer programs that have been used in corresponding chapters.

# Part I. Exploration of buried functional interfaces

By applying modern nanotechnology, researchers are creating many patterned interfaces to realize functional devices such as transistors, light emission diode, solar cells by either top down or bottom up methods. Self assembly is a promising bottom up technique that is economic and promising. On the other side of the coin, in many practical applications we prefer uniform interfaces and hetero structures at the interfaces like inclusions and defects shall be avoided. In this first part of the thesis, these two different cases are presented: the nano self assembled rings successfully fabricated in ultrathin films based on diffusion and reaction are introduced, and such structures is prefered to be the basis of functional patterned interfaces; practical functional adhesive interfaces studied by advanced X-ray scattering techniques are also discussed. Part I presents two examples of buried functional interfaces in thin films, which not only demonstrate the importance of buried interfaces, but also highlight the missing and necessity of interface sensitive imaging. Aiming at a powerful solution to many functional interfaces problems, the pupose of this PhD thesis is the development of the X-ray reflectivity imaging (XRI) technique to visualize buried functional interfaces, which contents are mainly included in Part II.

.

# Chapter 2 Formation of ultrathin Liesegang patterns

For many years, it has been believed that self-organized periodic ring structures known by the name of Liesegang patterns (LPs) are formed only in quite thick media, typically thicker than at least several microns. Actually growing LPs in ultrathin films is extremely difficult because of the drying of film and susceptibility to rapid capillary wetting. The present chapter reports how we successfully obtain LPs in ultrathin films of 65 nm thick. The key parameters are temperature control and the introduction of equilibrium water vapor in the sample environment. Atomic force microscope images clearly showed that the LPs are composed of 300 ~ 600 nm laterally coagulated particles. We have also evaluated the densities and thicknesses of the ultrathin films by X-ray reflectivity. During the present research, new patterns, which are different from ordinary LPs, have been discovered for the first time in the outermost part of the whole pattern. Studying LPs in ultrathin films may help to forge a better understanding of the mechanism underlying the intriguing phenomenon. Because of nanoscale scale thicknesses, self-organized periodic structures including so called LPs will open up new opportunities in nanotechnologies.

## 2.1 Introduction

Since German chemist Raphael Eduard Liesegang first discovered the intriguing phenomenon in 1896[12], Liesegang phenomenon, in which the coupling of diffusion (usually in a gel media) and reaction of participating chemicals (mostly in the form of co-precipitation) leads to the well-defined periodic bands of precipitation (Liesegang patterns), has attracted a considerable number of scientists from the fields of chemistry, geology, physics and biology because of its wide occurrence in nature[13–16]. Over the past century or so, a variety of patterns have been created and great efforts have been expended to unlock the mysteries of Liesegang patterns (LPs) by various chemical concentrations[17–19], gel media concentrations[19–22], gel degrees of cross-linking[23–25], electric fields[26–29] and others[30,31]. There is still much debate on the detailed mechanisms responsible for the underlying pattern-formation process. Taking this to the extreme limit by forming such patterns in ultrathin films may help to answer this lingering and controversial question. First of all, an ultrathin film is close to the ideal of 2D geometry and thus potentially avoids disturbance from other dimensions. Furthermore, it is easier to access the patterns in ultrathin films by surface characterization techniques such as atomic force microscopy[32] (AFM), total reflection X-ray fluorescence imaging[33,34] (TXRF-imaging) or grazing incidence small angle X-ray scattering[35] (GISAXS).

LPs are self-organized patterns, are easy to obtain, and have good potentials for application in the form of thin films. There have been many interesting experiments to apply these patterns in thin films including

fabrication of micro-optics[36], amplification and sensing[37,38], and preparation of micro- and nano-particles[39,40]. The gel thin films in these studies are in the order of 1 ~ 100 μm. Further downsizing to ultrathin films is promising and may open up new opportunities in nano technologies. However, according to the experiments of Bensemann[41], changes in the thickness of the gel had a pronounced effect on the periodicity of the patterns and for very thin gels ($d \approx 2$ $\mu$m), no periodic precipitation was observed. Growing such patterns in ultrathin films that are less than 1 μm thick has thus far been thought to be extremely difficult.

In this research, by controlling low temperature (5.0 ± 1.0 ℃) and introducing equilibrium water vapor to the sample environment, we successfully obtained the LPs in ultrathin films with a thickness down to 65 nm. In this chapter, we introduce this novel method and give an explanation of the mechanism of pattern formation in ultrathin films based on sol-coagulation and related scenarios.

## 2.2 Experimental Section

Ultrathin films of gelatin (Gelatin, Wako Pure Chemical Co. Ltd., Japan) containing the inner electrolyte (Potassium dichromate, Junsei Chemical Co. Ltd., ultra-pure: 99.5%) were prepared by the spin coating method. 10 g/L - 50 g/L water solution of gelatin with $K_2Cr_2O_7$ ( $m_{K2Cr2O7}$ / $m_{Gelatin}$ = 3 w %) was prepared via water dispersion and heated at 80 ℃ for 15 min. A 30 μl aliquot of the hot solution was pipetted onto a pre-cleaned Si (1 0 0) substrate (size: 10 mm × 10 mm) and immediately spin-coated at 2000 rpm for 20 s. The Si substrates were cleaned by several ultrasonic clean procedures: ultrasonic washing with acetone for 10 minutes followed by heated ultrasonication (55 ℃) in 1% $HNO_3$ for 30 minutes and then washed with distilled water. The procedures were repeated until the substrates surfaces were hydrophilic (because of the natural oxidized $SiO_2$ layer on the substrate surface). The outer solution (Silver nitrate, Junsei Chemical Co. Ltd., ultra-pure: 99.8%) was prepared by cold-dissolution and stored in a sealed beaker at 5.0 ± 1.0 ℃ with aluminum wrap to avoid reduction. Then the samples were processed to grow LPs by introducing the outer solution. FIG. 2.1 outlines the procedure: (a) 5 μl of cold silver nitrate solution was pipetted and softly dispensed onto the surface of ultrathin gelatin film doped with potassium dichromate; (b) thereafter the sample was safely brought into a well sealed sample case with a water droplet at the corner to provide equilibrium water vapor; (c) the sample was finally stored on the flat shelf of a refrigerator (5.0 ± 1.0 ℃) for 2 h or longer to produce the LPs.

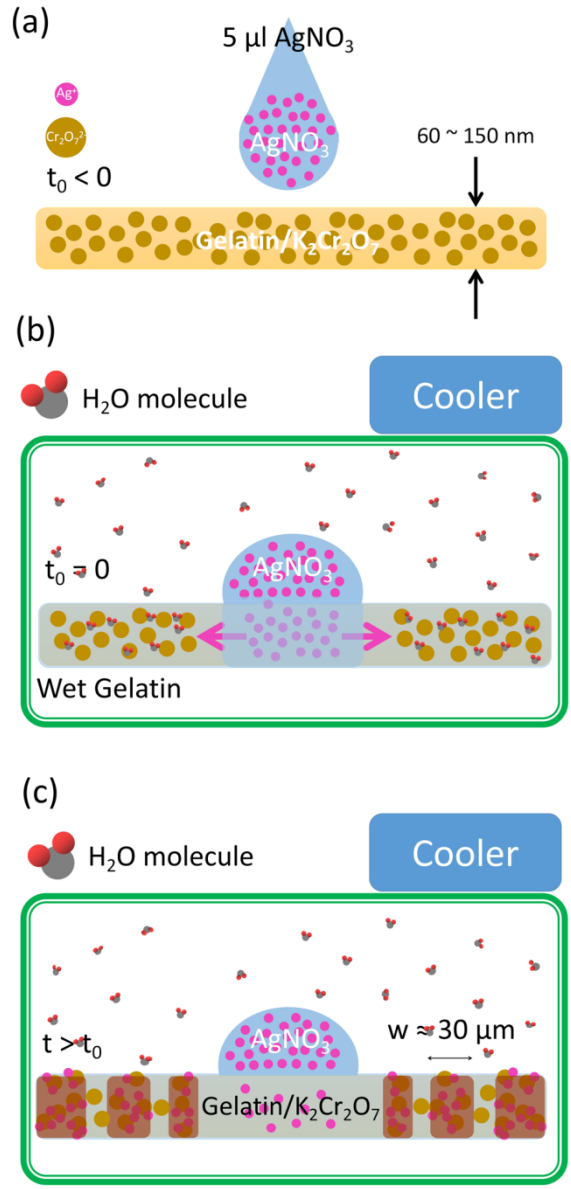


FIG. 2.1 Sketch of the experimental procedure of the Liesegang pattern (LP) formation in ultrathin film. (a) 5 µl of silver nitrate solution (0.5 mol/L) and cross-sectional view of the dry gelatin ultrathin film containing potassium dichromate ($m_{K2Cr2O7}$:$m_{gel}$= 3%). Small hot pink dots stand for the silver ions uniformly dispersed in the droplet; large orange dots represent the dichromate anions uniformly dispersed in the dry ultra gelatin thin film. (b) The sample was immediately brought into a well sealed sample case with controlled low temperature (5.0 ℃ ±1.0 ℃) and stable water vapor (equilibrium vapor at normal pressure, 5.0 ℃ ±1.0 ℃). (c) The sample case was then stored flat in the same condition to produce the LPs. The LPs appear after time t ≈ 2 h. Typical dimensions of LPs in ultrathin film are qualitatively illustrated.

The thicknesses of the ultrathin films of gelatin were evaluated by X-ray reflectivity (XRR) technique before the outer solution droplet was introduced. The contact angle measurement was conducted on the thick gelatin film (thickness of ~1 mm) to evaluate the surface nature of gelatin at different temperatures. The thick gelatin films were prepared by pouring the hot gelatin solution (50 g/L, 0.2 ml) onto the glass substrate (size: 20 mm × 20 mm). Fine structures of LPs were observed by tapping mode of atomic force microscopy (TM-AFM). For the TM-AFM, the Silicon Micro cantilever (OLYMPUS, OMCL-AC240TS-C2) vibrates at its resonant frequency (66.8 - 77.5 kHz, spring constant: 1.6 - 2.5 N/m) and maps the morphology of the sample by sensing the surface force.

## 2.3 Results and Discussions

### 2.3.1 Thickness of ultrathin gelatin film

The thickness of soft thin films could be obtained by X-ray reflectivity measurement[42]. Different gelatin concentration hot solutions were prepared to make gelatin films of varying thicknesses. X-ray reflectivity profiles (XRR) of the samples are shown in FIG. 2.2(a): red solid circle, 50 g/L; orange solid up-triangle, 25 g/L; green open star, 16 g/L; blue hollow up-triangle, 12 g/L; black open circle, 10 g/L. The period of interference fringes corresponds to the film thickness in a reciprocal relation. The thicknesses of the thin films were extracted by Fourier analysis as suggested in Ref. [43]. The first drops in the profiles near 3 mrad show the critical angles θc of the thin films, below which angles the X-rays undergo total reflection. The critical angles relate to the surface densities of films[44] by:

$$\theta_c = \sqrt{2\delta} = \sqrt{\frac{4\pi\rho r_0}{k^2}\left(1+\frac{f_1}{Z}\right)}$$

where δ is the deviation of refractive index n from unit [related to the scattering properties of the medium], k is the wavenumber [$k = 2\pi/\lambda$], ρ is the electron density of the medium, $r_0$ is the classical radius of an electron, $f_1$ and $f_2$ are the dispersion corrections for the gelatin, Z is the total atomic number. The parameters of gelatin used to analyze the data are summarized in Table 1. The thickness values and surface densities calculated from the critical angles are summarized in Table 2, and are also displayed in FIG. 2.2(b).

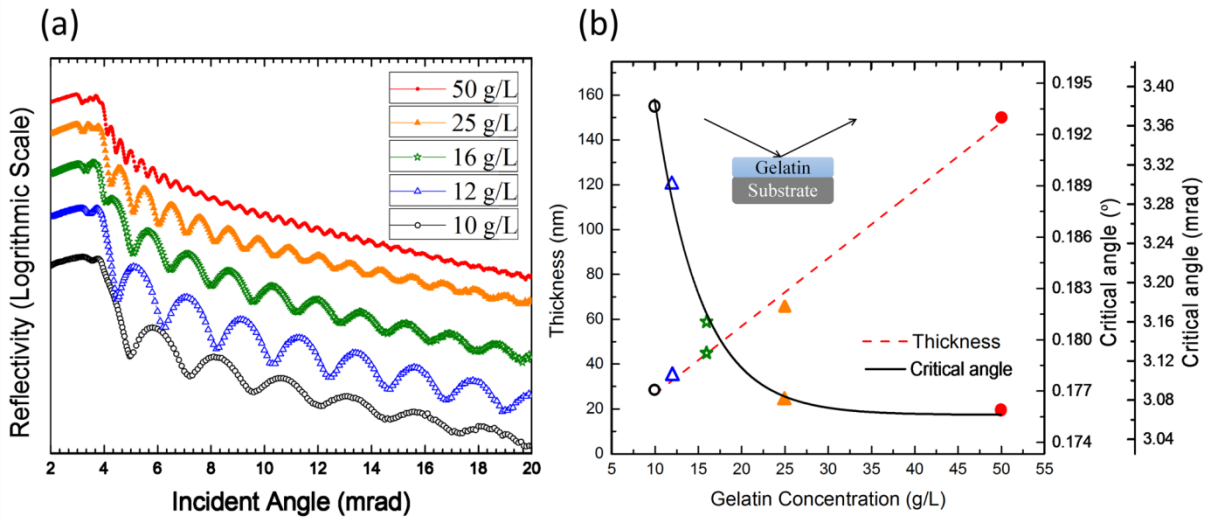


FIG. 2.2 (a) X-ray reflectivity profiles (XRR) of ultrathin films of dry gelatin prepared by different concentration hot solutions; red solid circle: 50 g/L, orange solid up-triangle: 25 g/L, green open star: 16 g/L, blue hollow up-triangle: 12 g/L, black open circle: 10 g/L. (b) Film thickness values extracted from XRR plotted as the gelatin concentration (left ordinate). Thickness follows a roughly linear relationship with the gelatin concentration. Critical angles profile of XRR [right ordinates, in unit of degree and mili-radian(mrad)] demonstrates a steep increase at around 25 g/L (from 50 g/L to 10 g/L).

The thickness increases roughly linearly with gelatin concentration, which is common in spin coating films. The critical angles (surface densities) of gelatin films with a thickness of 150.2 nm (Gelatin concentration: 50 g/L) to 65.4 nm (Gelatin concentration: 25 g/L) are around 3.08 mrad (mass density: 1.38 g/ml, typical value for bulk gelatin with humidity of 8% – 13% is: 1.3 g/ml - 1.4 g/ml.). However, when the thickness decreases further, the critical angle undergoes a steep increase; see FIG. 2.2(b). The surface density difference between the thin film with a thickness of d = 65.4 nm and that of d=29 nm is as large as 20 %. The surface densities of the thicker film show a relaxed value that is similar to bulk gelatin, while the surfaces of the thinner films ( < 65 nm) have much larger densities, probably experiencing more confinement from the substrate. The carbon plane of the gelatin chain near the substrate prefers to be parallel to the substrate[45,46] and because of this different conformation thinner films ( < 65 nm) have higher surface densities as the surface is much closer to the substrate compared with that of thicker film. It was reported[47] that the salt-doped thin gelatin film ( < 12 μm) has an anomalously low absorptivity of water due to the existence of a boundary layer near the substrate, whose physical properties are different from those of the bulk of the gel. In the XRR profiles measurement, we indirectly observed such a boundary layer near the substrate from the surface densities of gelatin thin films of different thicknesses. Introducing XRR is good as it measures the thickness very accurately (resolution to atomic scale) in a non-destructive manner.

TABLE 2.1 Summary of the atomic scattering factors and the dispersion corrections factors for the elements and typical repeating unit in gelatin when the X-ray wavelength is 1.54 Å. The one typical peptide sequence of gelatin [-Ala-Gly-Pro-Arg-Gly-Glu-4Hyp-Gly-Pro- (Ala = alanine; Gly = glycine; Pro = proline; Arg = arginine; Glu = glutamic acid; Hyp = hydroxyproline)] is seen as the repetition X-ray scattering unit.

| | C | H | N | O | $C_{35}H_{52}N_{12}O_{12}$ |
|---|---|---|---|---|---|
| Z | 6 | 1 | 7 | 8 | 442 |
| $f_1$ | 0.0168 | 0 | 0.0291 | 0.0464 | 1.494 |
| $f_2$ | 0.009 | 0 | 0.018 | 0.0322 | 0.9174 |

TABLE 2.2 Summary of the thicknesses, critical angles extracted from X-ray reflectivity profiles and surface densities of films prepared by hot solutions with different gelatin concentrations.

| Gelatin Concentration (g/L) | Thickness (nm) | Critical angle (mrad) | Surface Density (g/ml) |
|---|---|---|---|
| 50 | 150.2 | 3.07 | 1.38 |
| 25 | 65.4 | 3.08 | 1.39 |
| 16 | 45 | 3.16 | 1.46 |
| 12 | 34.5 | 3.3 | 1.59 |
| 10 | 29 | 3.38 | 1.67 |

### 2.3.2 Liesegang pattern formation

FIG. 2.3 shows the Optical microscopy images of LPs in ultrathin gelatin films with a thickness of 150 nm (gelatin concentration: 50 g/L) and 65 nm (gelatin concentration: 25 g/L) after 2 h of reaction and diffusion. The bright region is the source of outer solution silver nitrate in the form of a droplet, while the uniform dark area is the gelatin matrix doped with potassium dichromate. The yellow-green rings (only a quarter of rings shown in the images) are the LPs and the bold arrows indicate the moving direction of the reaction front. The LPs were well formed in both of the ultrathin gelatin films as shown in FIG. 2.3, with the precipitation bands of 10 ~ 50 μm in width. When the gelatin layer becomes very thin, it is thought to be extremely difficult to obtain LPs. Ref. [41] found that when the thickness is close to 2 μm, no LPs occur at all. The results we present in this chapter represent the thinnest film in which LPs have ever been reported to the best of our knowledge and it seems possible to go even further. Most previous reports[39,41,48,49] of LP formation in thin films (typically 1 ~ 100 μm) used the so-called WET stamping method (WETS) at room temperature to transfer the outer electrolyte into the gelatin matrix. We prepared the pattern by another method in a closed system with a low controlled temperature (5.0 ℃ ± 1.0 ℃) and stable water vapor pressure (equilibrium vapor at normal pressure, 5.0 ℃ ± 1.0 ℃), as shown in FIG. 2.1. By proposing this simple but feasible method, we can easily prepare LPs in ultrathin films (50 nm ~ 1000 nm) and can expect to obtain different sizes and morphologies.

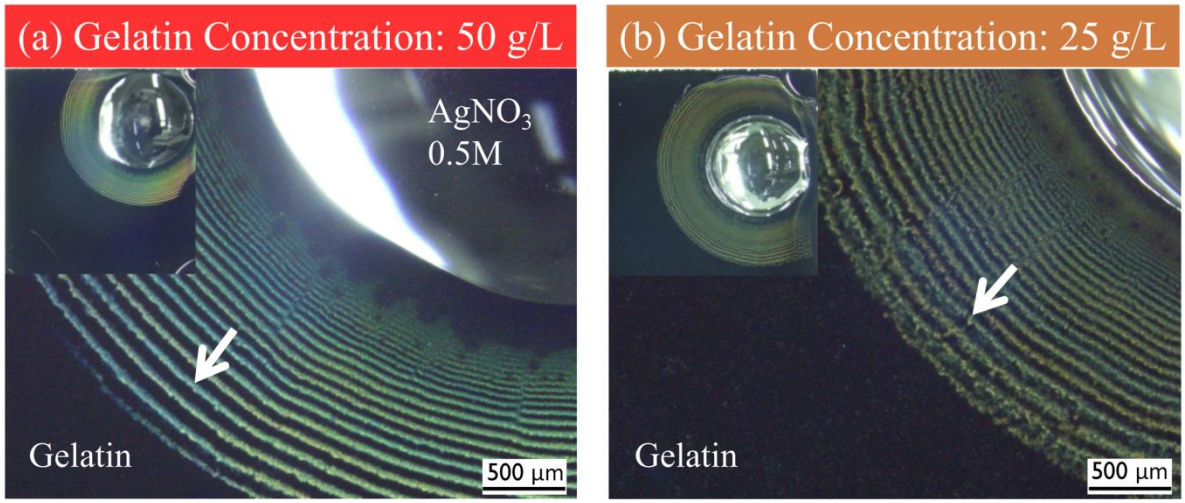


FIG. 2.3 Optical microscopy images of LP (rings) in the ultrathin gelatin films prepared from hot gelatin solution with the gelatin concentration of (a) 50 g/L and (b) 25 g/L. The bold arrows indicate the moving direction of the reaction front. Insets are the over view of the patterns. The silver nitrate solution droplet was dispensed onto the corner of each thin film to observe the outermost ring. Scale bar is 500 μm. The images were snapped 2 h after dispensing of the silver nitrate solution droplet.

To clarify the peculiarities of LPs in ultrathin films, we recalled the most famous feature of the pattern spacing law: for a given system and concentration of salts, the ratio of the distances $x_{n+1}$ to $x_n$ is constant for all bands ($p = x_{n+1} / x_n$), and p is the so called spacing coefficient[13]. FIG. 2.4(a) shows the measured distances of two consecutive rings from the junction of the silver nitrate droplet and the gelatin matrix, $x_{n+1}$ vs $x_n$, where n is the so-called band number starting from 1 with the nearest ring from the junction. The linearity of the plot confirms that the precipitation patterns obey the same spacing law as in ordinary LP systems: $x_{n+1} / x_n = 1.07$. In the micro films (15 ~ 120 μm), the spacing coefficient, p, increases linearly with increasing thickness d[41]. However, in our case, this rule doesn't apply and the spacing coefficients of two films with different thicknesses are the same. This implies that the initial concentrations of inner electrolyte for the two samples of differing thicknesses should be similar according to the Matalon-Packter law[17]: $p([A]_0,[B]_0) = F([B]_0) + G([B]_0)/[A]_0$, where $[A]_0$ ($[B]_0$) is the initial concentration of the outer (inner) electrolyte, and $F([B]_0)$ and $G([B]_0)$ are decreasing functions of $[B]_0$. This also indicates that the dry gelatin films with different thicknesses take up an amount of water proportional to the mass of gelatin. This seems intuitively true but it is not the case for the WET stamping of micro film reported by other researchers[14]. We conducted another experiment to study the influence of absorptivity of water on the pattern formation in ultrathin gelatin film: we prepared the experiment using the gelatin doped with the inner electrolyte with a mass ratio of inner electrolyte to gelatin: 6 w/w%. The spacing coefficients of two different thickness samples still share the similar value: p = 1.11, as shown in FIG. 2.4(b), (c). Compared with the control experiment, it is not surprising that the spacing coefficient changes with inner electrolyte concentration. However, we found that the spacing coefficient of the FIG. 2.4(b) ($m_{K2Cr2O7} : m_{gel}$ = 6 %) is surprisingly higher than that of FIG. 2.4(a) ($m_{K2Cr2O7} : m_{gel}$ = 3 %) {recall the Matalon - Packter law[17]: $p([A]_0,[B]_0) = F([B]_0) + G([B]_0)/[A]_0$}, which suggests that the gelatin doped with higher inner electrolyte to gelatin mass ratio tends to absorb more water[47]. The absorption of water does not only determine the concentration of inner electrolyte, but also influences the inherent properties of the gelatin network. Lagzi[20] experimentally found that the spacing coefficient increases linearly with the decrease in the concentration of the gelatin. Therefore, in case of the sample in FIG. 2.4(b), although the concentration of inner electrolyte may

increase and give a lower spacing coefficient, we got a higher spacing coefficient because the dry gelatin film absorbs more water [decrease in gelatin concentration, note the "gelatin concentration", which is proportional to the mass ratio of the pure gelatin to the wetted gelatin film, is different from the "gelatin concentration" used in ultrathin films preparation (water lost during spin-coating process) mentioned in Section 2.3.1] and provides the energy environment preferably leading to a much higher spacing coefficient'..

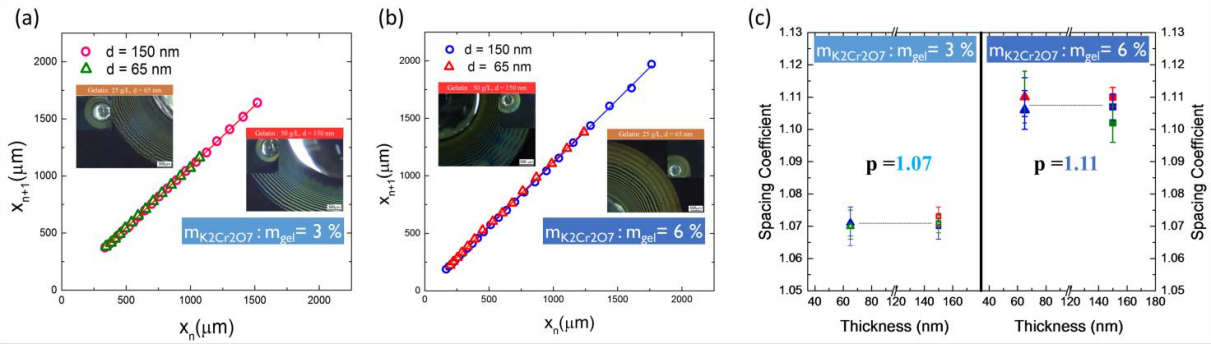


FIG. 2.4 Measured distances of two consecutive rings from the edge of the silver nitrate droplet, $x_{n+1}$ vs $x_n$. The linearity of the plot confirms that the precipitation patterns obey the same spacing law as in ordinary LP systems: $x_{n+1}$ vs $x_n$ = p, where p is the spacing coefficient (in the plot, p corresponds to the slope of the line). (a) $x_{n+1}$ vs $x_n$ plot of the LP formed in ultrathin films with thickness of 150 nm and 65 nm, where $m_{K2Cr2O7} : m_{gel}$= 3%. (b) $x_{n+1}$ vs $x_n$ plot of the LPs formed in ultrathin films with thickness of 150 nm and 65 nm, where $m_{K2Cr2O7} : m_{gel}$= 6%; only inner formed rings are counted, outer smeared patterns are neglected. (c) The spacing coefficients (p) of the samples with two different thicknesses d. For each sample, the spacing coefficient is the slope of linearly fitting $x_{n+1}$ vs $x_n$, with standard deviation (SD): slope ± SD; at each point, three samples are measured to check reproducibility and are plotted with different colors in the figure. The errors in the experimental graph are less than 2% of the p values. The spacing coefficients are both p = 1.07 for $m_{K2Cr2O7} : m_{gel}$= 3% and are plotted with hollow up-triangles (65 nm) and open rectangles (150 nm); The spacing coefficients are both p = 1.11 for $m_{K2Cr2O7} : m_{gel}$= 6% and are plotted with solid up-triangles (65 nm) and solid rectangles (150 nm).

### 2.3.3 Mechanism in ultrathin films

The mechanism responsible for LP formation is still under discussion and the models that try to explain the pattern formation can be divided into three main classes[50]: ion-product supersaturation[51–53], sol coagulation[18,54–59] and phase separation[60,61] theories. It is reasonable to assume that several mechanisms contribute to the LP formation. LPs appear through spatial redistribution of elements engined by diffusion and reaction; differences in theories arise from the details of treating the nucleation thresholds (the critical point at which precipitates form) and the growth kinetics of the precipitates. LPs are not always formed in such systems, since Liesegang pattern formation can transfer to crystal growth and/or uniform precipitation, which depends on the initial concentration of inner electrolyte, outer electrolyte and gelatin concentration[20–22]. The ultrathin gelatin films were prepared as dry films and lost water during the spin coating process. In addition, because of the ultrathin characteristics, the water inside the ultrathin films could evaporate very easily during the experiment. We need to consider the wetting process and maintenance of water during the experiment to help understand the mechanism, as the system needs an aqueous medium to transfer the outer ions and redistribute the intermediate particles. In addition, the transfer of species in the gelatin should be confined in the narrow tunnel of the cross-section of ultrathin film.

### 2.3.3.1 Wetting of gelatin film at 5.0 ± 1.0 ℃

A low temperature (5.0 ℃ ± 1.0 ℃) and controlled moisture are crucial for the success of LP formation in ultrathin films. To see the importance of low temperature, we made a comparison with the control experiment performed at room temperature [see FIG. 2.5 (e) and (f)].

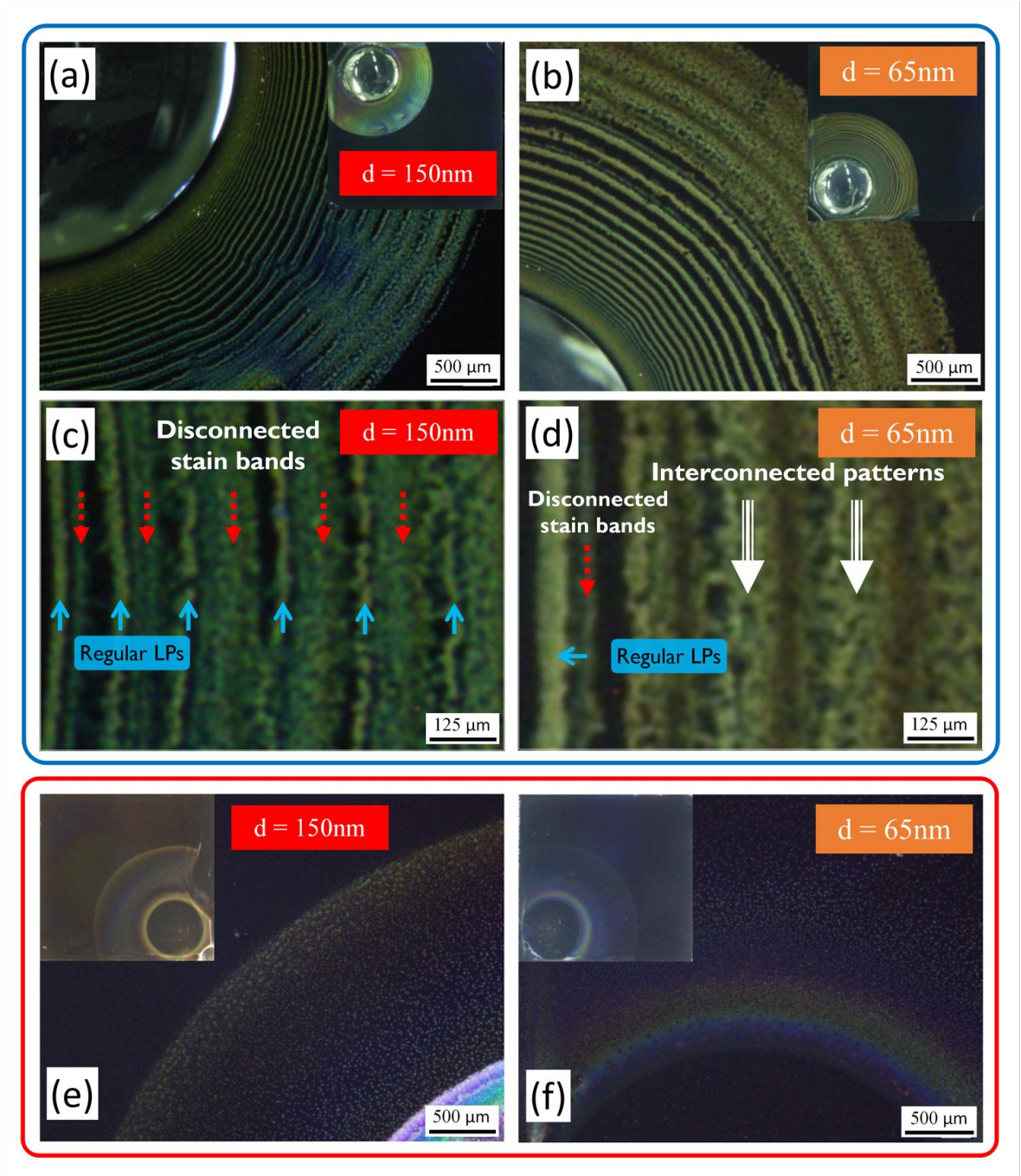


FIG. 2.5 Optical microscopy images of silver dichromate precipitation patterns formed at 5.0 ℃ ± 1.0 ℃ in ultrathin gelatin films with a thickness of (a) 150 nm, (b) 65 nm. Panels (c) and (d) show the disconnected stain bands and interconnected patterns area, which are the enlarged images of (a) and (b) respectively. The short solid blue arrows indicate the regular Liesegang patterns, long dashed red arrows indicate the disconnected stain bands between consecutive rings, and heavy triple solid line white arrows indicate the interconnected patterns. Optical microscopy images of silver dichromate precipitation patterns formed at 25.0 ℃ ± 2.0 ℃ in the ultrathin gelatin films with a thickness of (e) 150 nm, (f) 65 nm. The concentrations of the outer (silver nitrate) electrolyte is 0.5 mol/L, while the ratio of the inner electrolyte (potassium dichromate) to gelatin is

$m_{K2Cr2O7}$:$m_{gel}$= 6%. Insets are the overviews of the patterns. The silver nitrate solution droplet was dispensed onto the corner of each thin film to observe the outermost ring. The images were snapped 16 h after dispensing of the silver nitrate solution droplet.

When the outer solution of a chemical species A ($AgNO_3$) droplet is applied onto a thin layer of dry gelatin, doped with another chemical B ($K_2Cr_2O_7$), water and A are transported into the gel. Water from the droplet rapidly spreads into the dry gelatin by capillary wetting. For the case of water wetting a hydrophilic surface, the maximum velocity of the spreading front may be approximated by $V = \gamma\theta_E^3 / 9\sqrt{3}\eta l$ , where γ is the surface tension of the liquid, $\theta_E$ is the equilibrium contact angle, η is the dynamic viscosity of the liquid and l is a dimensionless parameter (typically l =15 ~ 20)[14]. Thus, for water (γ=70mJm$^{-2}$ and η~10$^{-3}$Pas) spreading towards an equilibrium contact angle of $\theta_E$ ~ 5°, the characteristic velocity is V ~ 100 μms$^{-1}$. For a substrate of 10 mm × 10 mm, it only needs 100 s to be completely wetted. The wetting process is very fast and the outer species A is also quickly sucked into the gel and reacts with inner species B. For the usual thin films (10 – 100 μm) by WETS, this hydrodynamic length is only for the top surface of the film and could be neglected. However, for the ultrathin films, the influence of such capillary wetting is fatal. No LPs form at room temperature because of such rapid wetting, as shown in FIG. 2.5 (e) and (f). In such cases, only ~ μm size aggregated particles formed, regardless of film thickness. The intermediate species (sol particles formed by $Ag^+$ and $Cr_2O_7^{2-}$ as described by sol coagulation theory) reached the threshold (flocculation point c* for induced sol coagulation theory[18] or spinodal value $c_s$ for spinodal phase transformation theory[60]) immediately after the reaction was triggered. All the intermediate species turned to precipitates at the same time showing the morphology of dispersed particles ( ~ μm) as a result of low absolute amount of the intermediate species in the ultrathin film.

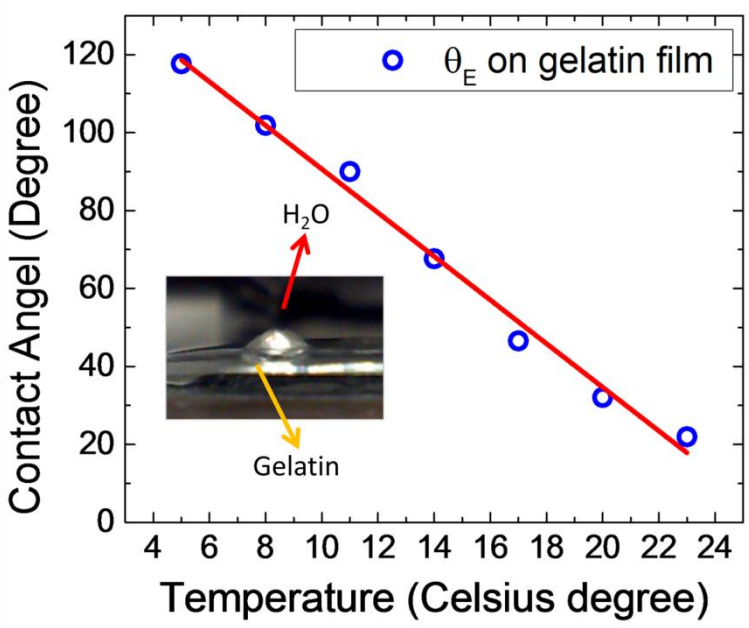


FIG. 2.6 Temperature-dependent contact angle measurements of gelatine films show the transition from hydrophilic to hydrophobic. The contact angle measurement was conducted on the thick gelatin films (~1 mm) to evaluate the surface nature of the hydrogel.

At a low temperature of 5.0 ± 1.0 ℃, the picture is totally different. FIG. 2.6 shows the temperature-dependent contact angle measurement on a wet gelatin film with a thickness of ~1 mm, revealing that the contact

angle decreases linearly with the temperature. This implies that the wet gelatin film surface turns from hydrophilic to hydrophobic at 5.0 ±1.0 ℃ compared with that at a higher temperature. The hydrophobic nature of gelatin film is rooted in the structure of the gelatin network. Gelatin is a protein rich in glycine, proline and hydroxyproline amino acids composed of carboxylic acid and amino groups. A gelatin hydrogel can be formed by physical cross-linking of carboxylic acid and amino groups on the polypeptides in water above a certain concentration (around 20 g/L) and below 30 ~ 35℃. During the process, polypeptides aggregate and undergo a conformational change from a random coil to a triple helix by hydrogen bonding. At the same time, intermolecular hydrogen bonds form between outward carboxylic acid and amino groups of the triple helixes. At room temperature, although the gelatin hydrogel is set and most of the carboxylic acid and amino groups form hydrogen bonding, there still exists a large number of carboxylic acid and amino groups that are not paired. The gelatin polymer network is highly hydrophilic and absorbs water through hydrogen bonds formed between water molecules and carboxylic acid and amino groups[62]. When the temperature decreases, the carboxylic acid and amino groups that do not pair at a higher temperature proceed to find the good conformation to form more hydrogen bonds and make the network much stiffer. As a result, the numbers of free carboxylic acid and amino groups decrease, with a more hydrophobic portion (non-polar) left on the surface. Since fewer outward free polar groups exist, we conclude that there is a smaller influence from capillary wetting at 5.0 ±1.0 ℃, which is of great importance to obtaining LPs in such an extreme system in ultrathin films.

In our system of LP formation in ultrathin films, water was supplied by vapor from outside of the films (the samples were kept in well sealed sample cases with a water droplet at the corner to produce equilibrium water vapor at 5.0 ±1.0 ℃, as displayed conceptually in FIG. 2.1). This amount of water helped keep the gelatin film wet in a soft way[63] and the cold temperature helped the droplets to stay in shape [Compare the insets of FIG. 2.5 (a) and FIG. 2.5 (e)]. As such, we can get rid of the complexity that diffusion of water brings when we consider the inner electrolyte concentration. As the water is supplied in the form of outside water vapor in the equilibrium state at the same temperature and ambient pressure during the experiment, we could assume the same initial concentration of inner electrolyte over the sample.

#### 2.3.3.2 Geometrical confinement and smeared structures

In the ultrathin system, the scenario of LP formation is modified to some extent by geometrical constraints. In thinner films (d=65 nm) [see FIG. 2.3(b)], the structure of the rings looks less defined and there exist some defects of disconnection in the rings further from the source droplet (porous ring). First of all, since the samples with different thicknesses show the same spacing feature (see FIG. 2.4), it is reasonable to deduce that the concentration of intermediate particles after the reaction front just before the formation of the nth ring is the same for two samples with different thicknesses. Thereby the absolute mass of silver dichromate to form the nth ring is proportional to the thickness d. There are smaller amounts of source materials (intermediate particles or sol particles) in the case of thinner film, so there is a greater possibility of forming disconnected rings (porous rings). On the other hand, the geometrical constraints could influence the growth of precipitates. With a thinner sample, the precipitates are in some degree confined by the thickness of thin films, thus tending to nucleate more and make the ring pattern much sparser.

The first point can be verified further by comparing the inner rings of the same thickness samples with different inner electrolyte "concentrations", as vividly shown in FIG. 2.7. The samples have the same thickness, but with different inner electrolyte "concentrations" [$m_{K2Cr2O7}$:$m_{gel}$= 3% for FIG. 2.7 (a) and $m_{K2Cr2O7}$:$m_{gel}$= 6% for FIG. 2.7 (b)]. Compared with FIG. 2.7 (a), the sample in FIG. 2.7 (b) has more inner electrolyte per unit volume. In the inner positions near the droplet, the outer electrolyte has a much higher concentration and thus the concentration of intermediate particles depends on the inner electrolyte. Because of the higher absolute amount of intermediate particles in FIG. 2.7 (b), the inner rings remain well defined even in ultrathin films with a thickness of d = 65 nm.

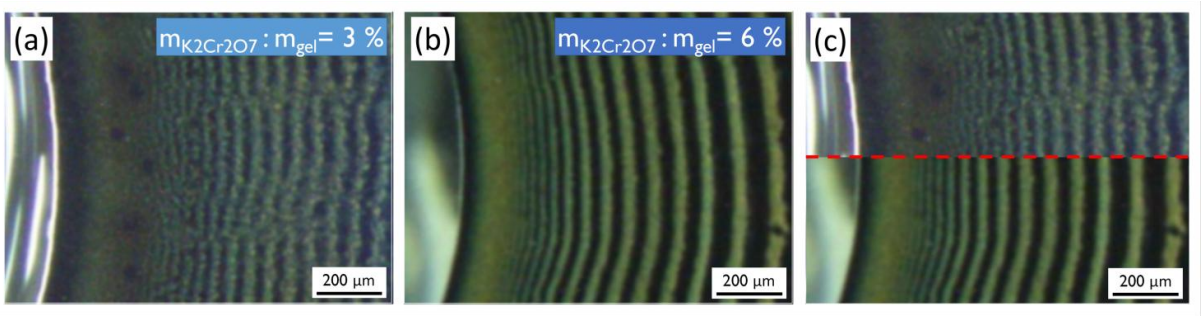


FIG. 2.7 Magnified optical microscopy images of LP (ring) in ultrathin gelatin films prepared from hot gelatin solution with the concentration of 25 g/L (thickness: 65 nm) and with different $m_{K2Cr2O7}$ / $m_{gel}$ ratio: (a) 3 % and (b) 6%. (c) Vividy overlap and comparison of the Liesegang patterns between the cases of (a) top half and (b) bottom half, where red dashed line indicates the boundary. Scale bar is 200 µm.

Other interesting structures are shown in FIG. 2.5 (c) and (d), which are the magnified images of the outer rings of FIG. 2.5 (a) and (b). The images were snapped 16 h after dispensing of the silver nitrate solution droplet. In such positions, either disconnected stain bands between the consecutive rings or interconnected patterns exist. In the thicker sample (d=150 nm), only stain band structures are observed, as shown in FIG. 2.5(c). However, both structures are observed in the thinner (d=65 nm) film, as shown in FIG. 2.5(d). When the outer electrolyte from the droplet diffused into a further out position, the concentration of the outer electrolyte became much lower as it is difficult for the ion supply to reach the further out position. As the outer electrolyte diffused outwards, the concentration of the outer electrolyte decreased so much that the threshold of precipitation was never reached until the samples were taken out from the sample cases into an ambient environment to conduct the optical microscope observation. When the samples were taken out, water in the sample evaporated immediately, thus increasing the local concentration and precipitates formed. However, as the samples dried out so quickly, the intermediate particles could not diffuse to the ring position and had to precipitate locally. In such a sense, the profile of the precipitates 'snapshot' was the concentration profile of the intermediate particles at the time when the sample was removed from the sample case. Thereby no well defined LPs formed, instead a secondary stain structure or smeared structure was left. Usually, such a smeared structure cannot be observed in the bulk experiment because such a structure does not form in a wet sample without a drying process (the intermediate particles are invisible to the eye). The length from the junction between the droplet and gelatin matrix to the outermost position of well-defined LPs is defined as the effective diffusion Length (EDL). Table 3 shows the effective diffusion lengths of different samples. The samples prepared under the exactly same conditions have different EDLs. However, the ratio of the area of EDL to the area of initial droplet of the samples prepared under the same condition [$m_{K2Cr2O7}$ / $m_{Gelatin}$ = 3 w/w %] is a constant, which indicates the

outer electrolyte diffusion profile is quite reproducible. The droplet size on the other hand depends on each experiment. Compared with $m_{K2Cr2O7}$ / $m_{Gelatin}$ = 3 w/w %, the sample made from $m_{K2Cr2O7}$ / $m_{Gelatin}$ = 6 w/w % possesses shorter effective diffusion length and smaller EDL area to droplet area ratio, which implies that the consumption of silver nitrate by the sample with a higher $m_{K2Cr2O7}$ / $m_{Gelatin}$ ratio forces the concentration of silver nitrate in the diffusion front to decrease more 'quickly' than that with a lower $m_{K2Cr2O7}$ / $m_{Gelatin}$ ratio (that outer electrolyte concentration decreases with length was verified in the experiments by the existence of disconnected stain bands between the consecutive rings and/or interconnected patterns).

TABLE 2.3 Summary of the effective diffusion lengths (EDL) of several samples with d = 150 nm prepared with different $m_{K2Cr2O7}$ / $m_{Gelatin}$ ratios.

| $m_{K2Cr2O7}$ / $m_{Gelatin}$ | droplet size R (mm) | EDL(mm) | $(EDL^2+2R*EDL)/R^2$ |
|---|---|---|---|
| 6 w/w % | 1.450 | 0.786 | 1.4 |
| 3 w/w % | 2.295 | 1.776 | 2.1 |
| 3 w/w % | 2.284 | 1.816 | 2.2 |
| 3 w/w % | 1.878 | 1.443 | 2.1 |
| 3 w/w % | 2.408 | 1.879 | 2.2 |

### 2.3.4 Fine structures of LPs

Fine structures of the pattern in ultrathin gelatin films were observed by the tapping mode atomic force microscope, as shown in FIG. 2.8. FIG. 2.8 (a) and (b) show the typical morphology of the rings, which are composed of 300 – 600 nm (in lateral diameter) precipitate particles. FIG. 2.8 (c) displays the junction of the ring and inter-ring space. The well-defined LPs in the ultrathin films are composed of small particles, which has been also pointed out by Walliser[39]. Approaching the edge of the rings, the particles become sparser and the sizes become smaller [see the edge near the left margin in FIG. 2.8 (c)]. The inter-ring position is quite clean, and only a few very small particles exist. More precipitate particles and bigger particles exist in the center, so the sol particles should have diffused into the center position of the ring from the inter-ring position (verify the diffusion of intermediate particles). We have shown the thickness of the dry gelatin film is 150 nm in the previous section. As a result, the precipitate particles may retain a disk like shape (long in a lateral direction, while short in depth), although the true thicknesses of the particles may be larger than the film thickness to some extent.

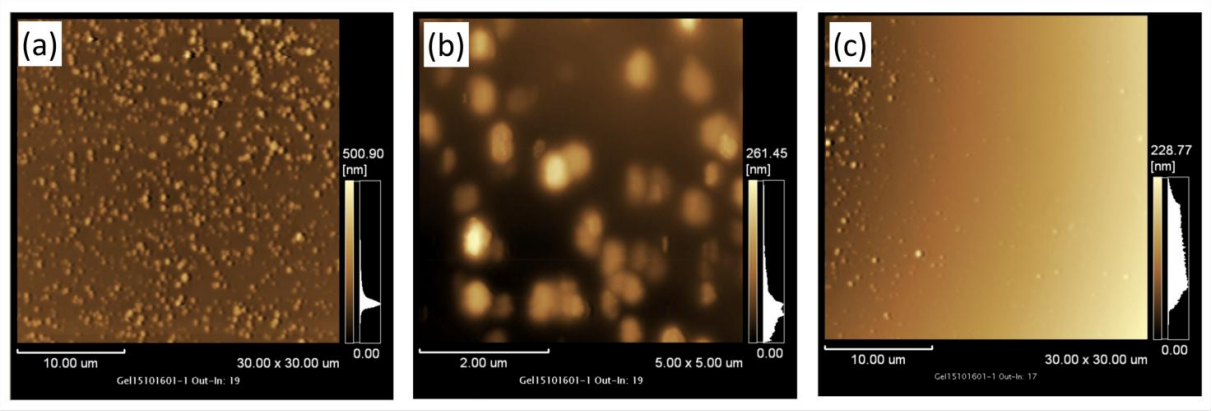


FIG. 2.8 Typical tapping mode atomic force microscopy (AFM) images of (a) a LP ring, (b) the same LP ring at higher magnification, and (c) the junction of the ring and inter-rings space formed in d=150 nm film at 5.0 ℃ ±1.0 ℃. The concentration of the outer (silver nitrate) electrolyte is 0.5 mol/L, while the mass ratio of the inner electrolyte (potassium dichromate) to gelatin is $m_{K2Cr2O7}$:$m_{gel}$= 3%. The silver nitrate solution droplet was softly removed 2 h after dispensing to terminate the reaction for AFM observation.

### 2.3.5 Thinness Limit

The remaining question is whether there is a limit for film thickness below which no LPs will be formed. FIG. 2.9 shows the Optical microscopy image of the structure formed in ultrathin gelatin films with a thickness of 29 nm (Gelatin concentration: 10 g/L) after 2 h of reaction and diffusion. The bright sector is the source of outer silver nitrate solution in the form of a droplet, while the uniform dark area is the gelatin matrix doped with potassium dichromate. There is a uniform grey area of precipitates in quite a long region (~1mm long from the junction between the droplet and gelatin matrix to the outer edge of this area). There are two rings formed in the outermost area, but such structures cannot continue to grow, as there is a limit to effective diffusion length (typically 1.5 – 2.0 mm for $m_{K2Cr2O7}$ : $m_{gel}$= 3%) for a well defined structure (see Section 2.3.3.2). The reason for such a uniform grey area near the droplet is hypothesized as: (a) the thickness of the film is comparable to the gel's diameter of gyration 2Rg, thus giving a different media property, such as a smaller pore size; (b) the thinner film, which is more influenced by the substrate, has a different conformation compared with the thicker films, showing different absoptivity property of water (see FIG. 2.2(b)). By changing the gel materials or substrate materials, these problems may be avoided. Such research could be studied in the future.

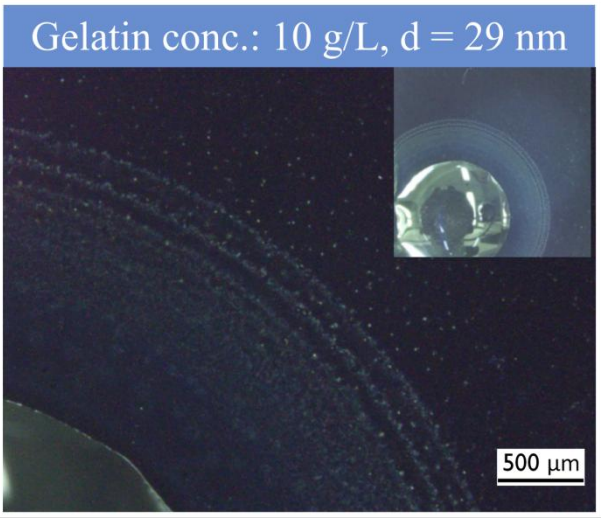

FIG. 2.9 Optical microscopy image of the structures formed by diffusion of outer electrolyte (silver nitrate) and reaction with inner electrolyte (potassium dichromate) in ultrathin gelatin films prepared from hot gelatin solution with the concentration of 10 g/L (Thickness: 29 nm). Inset is the overview of the patterns. The silver nitrate solution droplet was dispensed onto the corner of the thin film to observe the outermost ring. Scale bar is 500 μm. The images were recorded 2 h after dispensing of the silver nitrate solution droplet.

## 2.4 Conclusion

In summary, by controlling rather a low temperature (5.0 ± 1.0 ℃) and introducing equilibrium water vapor in the sample environment, we successfully obtained LPs in ultrathin films with a thickness down to 65 nm. The thicknesses of the films were measured by X-ray reflectivity technique in a non-destructive manner. Besides the thicknesses of thin films, we also obtained the surface densities of thin films with different thicknesses and found that when thinner than ~65 nm, the surface density increases greatly (up to 20 % in the film of ~29 nm), and this point may be crucial to explore LP formation in further ultrathin films. At 5.0 ± 1.0 ℃, gelatin hydro-gel surface shows a hydrophobic nature, which helps prevent the gelatin from being wetted by rapid capillary wetting. This is the clear reason why we succeeded in obtaining LPs. We found that disconnected stain bands between the consecutive rings and/or interconnected patterns exist in ultrathin films in the outermost part of the pattern when enough time is given to let the pattern grow. Fine structures of the pattern in ultrathin gelatin films were also observed by the tapping mode atomic force microscope, and it was found that the Liesegang rings are composed of 300 – 600 nm laterally coagulated particles.

# Chapter 3 Adhesive interfaces studied by X-ray reflectivity

Polymer adhesion to inorganic substrates is a long-standing problem that has been a focus of intensive researches for many decades. Although interfacial adhesion properties are largely determined by molecular structures at buried interfaces, structure-property relationships at buried inorganic/organic interfaces are not well understood due to a lack of nondestructive interface sensitive analytical techniques. Better understanding interfacial structures will aid in the rational design of adhesive package interfaces that can withstand harsh stress testing conditions. X-ray reflectivity (XR) is a promising nondestructive technique to characterize buried interfaces in ultrathin films with sub-nano resolution. XR could thereby become a complementary technique in the adhesives researches. In this research, we studied the hardening process of a commercial adhesive deposited on silicon substrate by XR. We found that the thicknesses of adhesive thin films decrease after hardening. In addition, there exists low density interfacial region in thicker samples, which could be caused by pores or impurities. In order to confirm such interfacial structures, an imaging technique such as our recent invented X-ray reflectivity imaging that will be introduced in Part II is powerful, although it still need to be developed to fulfill practical applications such as the adhesive interfaces due to the limited spatial resolution at the present stage.

## 3.1 Intoduction

Polymer adhesives are ubiquitous in modern society, forming connections between differnt matrix components, applied in industries such as aerospace engineering[64,65], marine coatings[66], microelectronics[67,68], and packaging. Critical properties such as the chemical resistance, corrosion resistance, thermal stability and mechanical strength of these materials strongly influence the applications. As adhesives serve as the junction between different materials, ‘good’ interfacial structures are always of great importance and control such properties. X-ray reflectivity is a promising technique for characterizing buried layers and interfaces in ultrathin films because it is possible to non-destructively measure the electron density profile along the depth in an atomic spacing level resolution. However, there are few reports about adhesive interfaces research by X-ray reflectivity. In this chapter, we discuss the method to prepare thin adhesive films and the feasibility of studying adhesive interfaces by X-ray reflectivity.

# 3.2Experimental

## 3.2.1 Preparation of adhesive thin films

We have studied a substrate coated comercial ultraviolet (UV) curing adhesive, which is mainly composed of UV oligomers, photoinitiators and acrylic polymers. The UV oligomers act as the backbone of the cured material to determine the desired physical properties. The photoinitiator's role is to absorb the UV light and initiate the curing process. The acrylic polymers is the basic bone of adhesive before curing process, while the adhesion level before UV depends on this. The UV curing adhesive is widely used in various industrial processes such as the medical industry and the microelectronic industry due to its high transparency and exceptional stability, even in difficult environmental conditions such as humidity and sunlight. If offers excellent adhesion to glass, metals, ceramics, rubber and most plastics, requiring no mixing and eliminating waste.

In order to prepare adhesive samples suitable for X-ray reflectivity measurement, the adhesives were spin coated on a pre-cleaned polished silicon substrate. FIG. 3.1 shows the sketch of the approach to prepare thin films of UV curing adhesives on silicon substrates. The Si substrates were cleaned by several ultrasonic clean procedures: ultrasonic washing with acetone for 10 minutes followed by heated ultrasonication (55 ℃) in 1% $HNO_3$ for 30 minutes and cleaning by distilled water. The procedures were repeated until the substrates surfaces were hydrophilic (because of the natural $SiO_2$ layer on the substrate surface). The adhesives were dissolved in toluene with proper volume to adjust the viscosity to nearly 1 cP,

$$\nu_{sol} = \frac{V_{ad}\nu_{ad} + V_{solvent}\nu_{solvent}}{V_{sol}}$$

where $\nu_{sol}$ stands for the viscosity of solution, $\nu_{ad}$ and $\nu_{sovent}$ correspond to the viscosity of adhesives and added solvent, repectively, $V_{ad}$ and $V_{sovent}$ correspond to the volume of adhesives and added solvent, repectively. By adjusting the volume of the added solvent, it is possible to prepare different thicknesses adhesive thin films. Thereafter, 15 μL of the solution was dispensed onto the silicon substrate (size: 10 mm × 10 mm) and spin coated at 2000 rpm for 20s. The X-ray reflectivity curves of the as coated samples [stabilized] were measured by a θ/2θ scan X-ray reflectometer. The thin film samples were cured by exposure to a UV source (366 nm) for 2 min. The X-ray reflectivity curves of the cured samples were measured in situ by the same X-ray reflectometer.

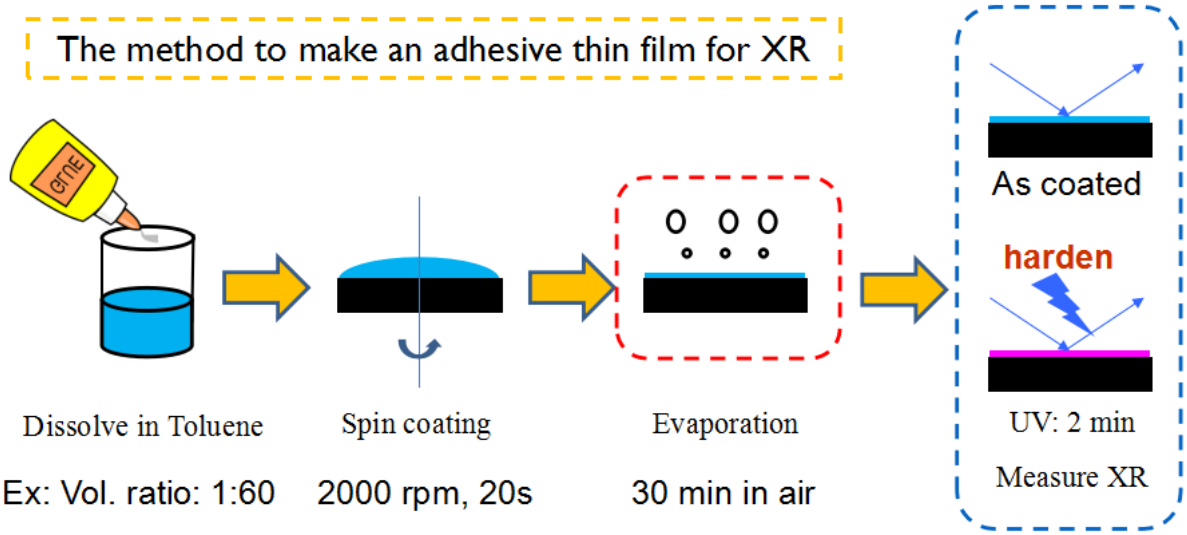


FIG. 3.1 Shetch to show the approach to prepare thin films of UV curing adhesives on silicon substrates. The adhesives were dissolved in a good solvent; 15 μL of the solution was dispensed and spin coated on a pre-cleaned silicon substrate. The X-ray reflectivity curves of the samples were measured by a θ/2θ scan X-ray reflectometer.

## 3.3 Results and Discussions

### 3.3.1 Stability of the soft thin films

Most of adhesives are polymer-based or naturally extracted soft matters. Although nice reference books are found employing X-ray scattering techniques to study soft materials[4,42], it is necessary to check the stability of the adhesive thin film sample exposed to X-rays. FIG. 3.2 shows the X-ray reflectivity profiles of the UV curing adhesive thin film sample in different storing time: as coated (black open rectangle), 2 hrs in ambient enviroment (red solid circle) and 18 hrs in ambient enviroment (blue open triangle). The X-ray reflectivity profiles show a high degree of repeatability, indicating that the sample was stable during the measurement time

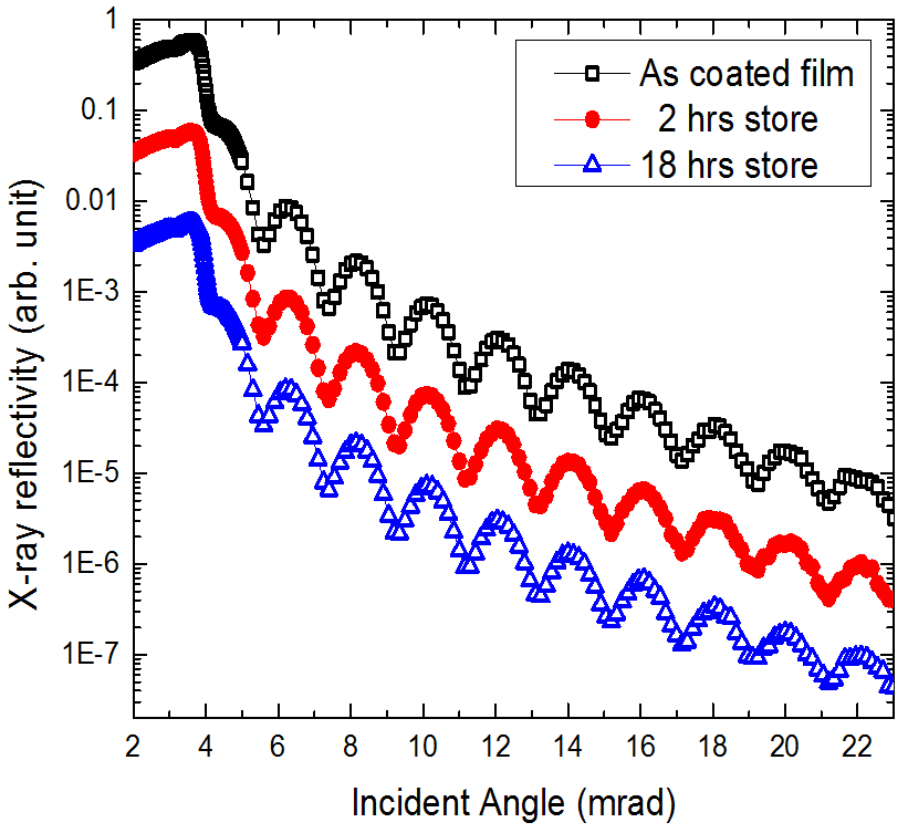


FIG. 3.2 X-ray reflectivity profiles of the UV curing adhesive thin film sample in different storing time: as coated (black open rectangle), 2 hrs in ambient enviroment (red solid circle) and 18 hrs in ambient enviroment (blue open triangle). Profiles are shifted vertically for clarity.

## 3.3.2 Interfacial change induced by UV radiation

### 3.3.2.1 Ultrathin adhesive films

FIG. 3.3 presents the X-ray reflectivity profiles of the UV curing adhesive ultrathin film sample measured as coated (black open rectangle) and right after the UV radiation (366nm, magenta solid downtriangle). Compared with the as coated profile, there is a systematical shift of the X-ray reflectivity after UV radiation, as shown especially in the range of high angles (15 mrad ~ 22 mrad). By using Parratt's formulism[6], the two profiles have been fitted by using the GenX software[69]. In order to extract reliable information, we started the analysis by assuming simple model to fit the measured data. The software calculated the X-ray reflectivity curves of the model with varing parameters [density, thickness and roughness]. By evaluating the figure of merits of the calculations, it is possible to pick up the best fit and extract the information of the thin film sample. We were able to obtain a good fitting of the data by assuming a two-layer model, while the one layer of adhesives model does not give proper fitting results. In GenX, the extracted parameters of the thin film are usually summarized and displayed as a scattering length density (SLD) profiles, as shown in the inset of FIG. 3.3。 The substrate / adhesive interface is defined as Z = 0, while the Z points from the substrate / adhesive interface into the adhesive layer. The SLD is a product of electron density ($\rho_e$ /Å$^3$) and classical radius of electrons (or Thomson scattering length), modulated by the stoichiometric mixture of the atomic form factors and the dispersion corrections.

$$SLD = r_e \rho(z) \sum_{j=1}^{N} \frac{f_j^0 + f_j'(E)}{Z}$$

where $r_e$ = 2.814 $\times 10^{-5}$ Å, ρ(z) is the electron density profile along the depth, $f_j^0$ is the atomic form factor and $f_j'(E)$ is the dispersion correction of the element that the jth electron belongs to, $Z$ is the atomic number. In case of a homogeneous medium and far away from absorption edges, which is the case for the samples of this chapter, we may simplify the expression of the SLD.

$$SLD = r_e \rho(z)$$

For the light elements, the atomic weight is approximately 2 times of the atomic number, for example, Z(Si) = 14 and M(Si) = 28 g/mol, while Z(C) = 6 and M(C) = 12 g/mol. Thereby 2 g of light matters contain 1 mol of electrons. As a result, the mass density is proportional to the electron density and the scattering length density, as displayed in the inset of FIG. 3.3. The thickness of the ultrathin adhesive film is around 400 Å with a low surface density layer of 50 Å. We observe a 'good' interface between the silicon substrate and the UV curing adhesive, which indicates that the adhesive is well attached to the silicon substrate. The X-ray reflectivity profile tells the 'goodness' of interface by showing well defined interference fringes. The main difference or change of the scattering length density profile after curing compared with the as coated case is the shrink of the surface layer thickness. Further investigations are introduced further in the next subsection.

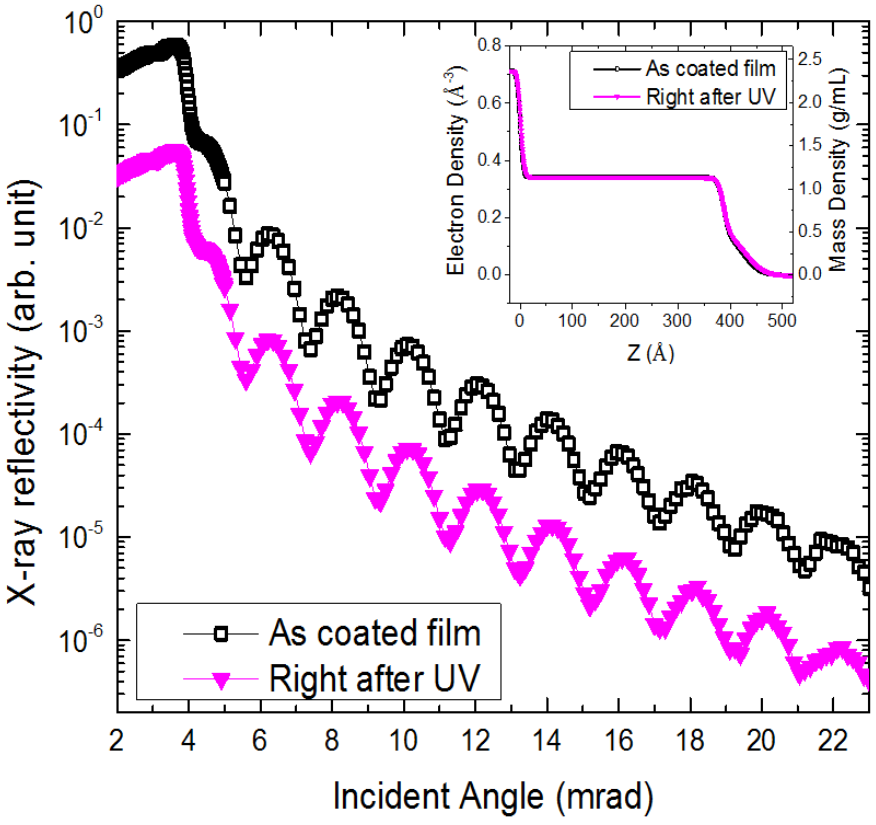


FIG. 3.3 X-ray reflectivity profiles of the UV curing adhesive ultrathin film sample measured as coated (black open rectangle) and right after the UV radiation (magenta solid downtriangle). Profiles are shifted vertically for clarity. Inset shows shows the

electron density profiles ($Å^{-3}$, the right vertical axis shows the mass density in g/mL) of as coated (black open rectangle) and after UV radiation (magenta solid downtriangle) extracted from the fitting of the profiles.

#### 3.3.2.2 Thin adhesive films

It is necessary to investigate the interfaces what if we increase the thickness of an ultrathin adhesive film, as the interface may become worse for thick samples. FIG. 3.4 presents the X-ray reflectivity profiles of the UV curing adhesive thin film sample measured as coated (red open circle), right after UV exposure (green solid triangle) and 16 hrs after UV radiation (blue open rectangle). In the same way, the three profiles have been fitted by using the GenX software. We were able to obtain a good fitting of the data by assuming a three-layer model, while the one-layer or the two-layer of adhesives model does not give proper fitting results.

Compared with ultrathin film case, we obsreve larger shift of X-ray reflectivity profiles at high incident angle range. Following the UV irradiation, the thin film sample experienced a slow dynamic change (compare green solid triangle and blue open rectangle data). The inset of FIG. 3.4 shows electron density profiles (or the mass density profile) along the depth extracted from the fitting. The thickness of the film is around 1850 Å with gradient low density at the surface. The thickness of the thin adhesive film is 4.5 times of the ultrathn adhesive film. Because of the thickness difference, the thin adhesive film possesses a different profile compared with the ultrathin case. There exists a low density region (the range of z = 0 ~ 50 Å) at the interface between the silicon substrate and the UV curing adhesive. Such low interfacial density region may due to the presence of pores or impurities. Compared with the case of a ultrathin film, it is more difficult for the solvent to evaporate during the spin coating process. The solvent may aggregate at the interface, where the energy is different. Thereafter the solvent may keep to arise impurities or escape to form a void. In order to understand the interface thoroughly, in-plane resolution is needed. Following the UV irradiation, the thicknes of the thin film sample decreaseed. This shrinkage is caused by the crosslinking and polymerization of the adhesive. Moreover, the sample's thickness decreases further for the sample 16 hrs after UV radiation, which means time is necessary for the thin adhesive film to be totally cured. Moreover, the interface density increases after UV irradiationn and storing. The fact tells the UV curing adhesive thin film was cured under the exposure of ultraviolet radiation.

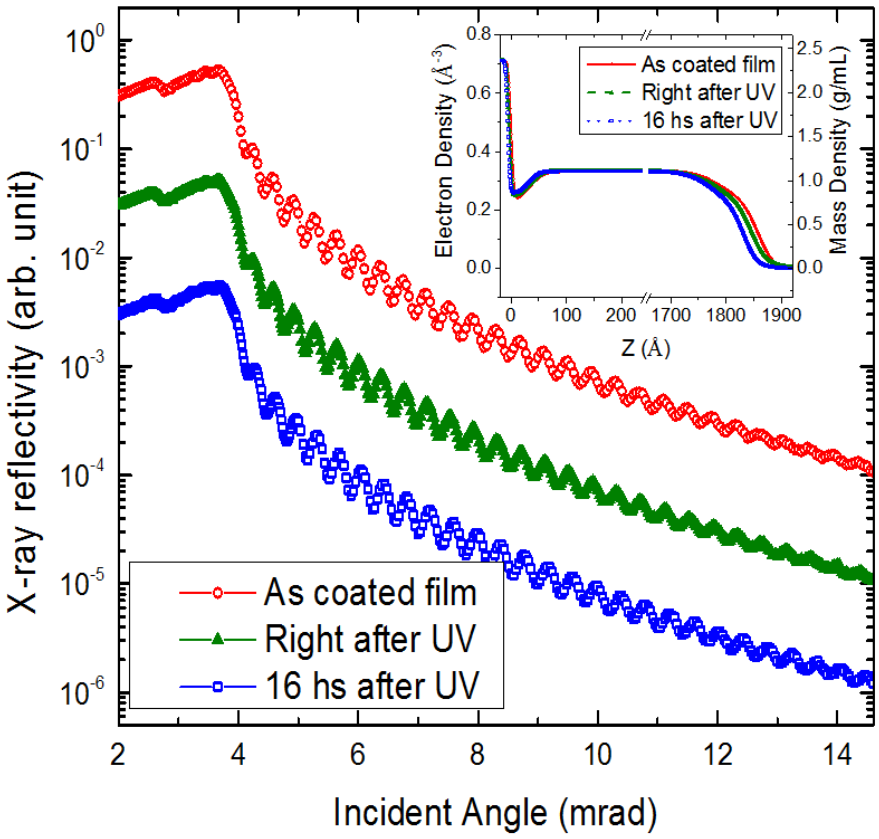


FIG. 3.4 (a) X-ray reflectivity profiles of the UV curing adhesive thin film sample measured as coated (red open circle), right after UV exposure (green solid triangle) and 16 hrs after UV radiation (blue open rectangle). Profiles are shifted vertically for clarity. Inset shows the electron density profiles (the right vertical axis shows the mass density in g/mL) extracted from the fitting of the profiles.

## 3.4 Conclusion

X-ray reflectivity could become a complementary technique in the adhesives researches. In this research, we have demonstrated that X-ray reflectivity is a powerful technique to study the buried interface of adhesive thin films in atomic scale resolution. By spin coating, we have established the method to study adhesive thin films by X-ray reflectivity. In specific, we have studied the UV curing adhesives, and found the hardening process and interfacical defects can be detected by XR, the shrinkage of adhesives after curing may be also retrieved. In the experiment, there still exist some problems and shall be addressed in the future: (1) the realibility of X-ray reflectivity fitting is a long standing problem, where we need some pre-knowledge of the sample. (2) the conformation of the silicon substrate shall be discussed, and the relationship between the model sample and practical adhesives need to be clarified.

# Part II. Original X-ray reflectivity imaging technique

In this information age, scientists are creating and utilizing many functional devices composed of complicated interfaces. In order to understand how the interfaces work and/or to check if the designed interfaces are properly fabricated, a non-destructive imaging technique is in urgent demand. Furthermore, in many practical applications a uniform interface is preferred and it is important to have a characterization technique to tell the ‘goodness’ of the interface or the location of ‘bad (hetero)’ structure that we call ‘defects’. By applying Liesegang pattern formation in multi-layered ultrathin films we are able to fabricate complicated structures, but we cannot see and check the patterned interfaces with present characterization techniques. This limitation hinders the understanding and application of such interesting phenomenon. In case of adhesive researches, composite materials, adhesives and adhesive / materials interfaces form an adhesion system. If the adhesives are peeled off from the materials, there is no evidence the properties are as the same as they are in the adhesion system. Aiming at a powerful solution to many functional interfaces problems, we have successfully developed an X-ray reflectivity imaging (XRI) technique. In the second main part of this thesis, the XRI system employing synchrotron radiation X-rays to visualize buried inhomogeneous / patterned layers and interfaces is introduced firstly. Second, micro X-ray reflectivity profiles obtained from in-plane and grazing incident angle combined scan in XRI fashion is proved. Third, the XRI system implemented in with laboratory ‘mobile’ setup 15W power source is also presented. By applying our technique, it is possible and promising to fabricate and image three dimensional tunable regular structures by ultrathin Liesegang pattern formation. The pattern formation may move to the next stage with the aid of our XRI technique. In the case of adhesive interfaces, application of XRI is also promising to directly in situ visualize the adhesive interface under normal or harsh service.

# Chapter 4 Theoretical background of X-ray reflectivity imaging

This single chapter describes the basic principle of X-ray reflectivity, that of X-ray reflectivity imaging and image reconstructions algorithms.

## 4.1 X-ray reflectivity

### 4.1.1 Refractive index

X-ray reflectivity (XR) is a probe to inverstigate surfaces and interfaces in angstrom scale. An electromagnetic plane wave including X-rays given by its electric field vector $\mathbf{E}(r) = E_0 \exp(i\mathbf{k_i}\cdot\mathbf{r})$, which penetrates into a medium characterized by an index of refraction $n(\mathbf{r})$, propagates according to the Helmholtz equation

$$\Delta\vec{E}(r) + k^2 n^2(\vec{r})\vec{E}(\vec{r}) = 0$$

where $k = 2\pi/\lambda$ is the modulus of the wavevector ki and $\lambda$ denotes the x-ray wavelength. In general, the index of a refraction medium for X-rays is calculated and expressed as

$$n(\vec{r}) = 1 - \delta(\vec{r}) + i\beta(\vec{r})$$

with the dispersion $\delta$ and absorption terms $\beta$

$$\delta(\vec{r}) = \frac{2\pi r_0 \rho(\vec{r})}{k^2} \sum_{j=1}^{N} \frac{f_j(0) + f_j'(E)}{Z}$$

$$\beta(\vec{r}) = \frac{2\pi r_0 \rho(\vec{r})}{k^2} \sum_{j=1}^{N} \frac{f_j''(E)}{Z}$$

where $\delta$ is always positive, $r_0$ is the classic electron radius $r_0 = 2.814 \times 10^{-5}$ Å, k is the wavenumber, $\rho$ is the electron density of the medium, Z indicates the total number of electrons, $f_j(\mathbf{Q})$ is the atomic scattering length

$$f_j(\vec{Q}) = f_j^0(\vec{Q}) + f_j'(E) + i f_j''(E)$$

usually tabulated as Atomic Form Factors.

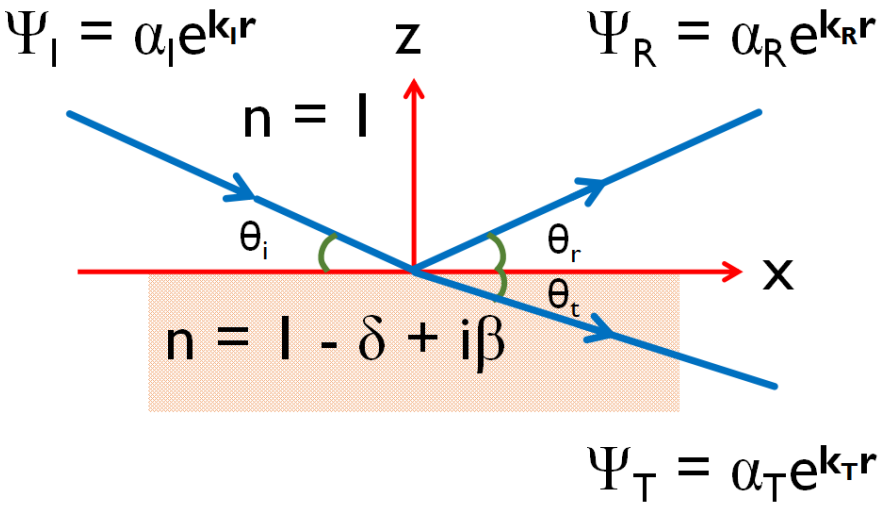


FIG. 4.1 A plane electromagnetic wave with wavevector $\mathbf{k_i}$ hits a surface at a grazing angle $\theta_i$. The wave splits into a reflected ($\theta_i = \theta_r$) and a refracted wave transmitted at the angle at $\theta_t$, Snell's law and the Fresnel equations can be derived by requiring continuity at the interface of the wave and its derivative. [44]

For a single vacuum/medium interface the Snell's law of refraction gives $\cos\theta_i = (1 - \delta)\cos\theta_r$, where $\theta_r$ is the exit angle of the refracted X-rays (as shown in FIG. 4.1). Thus if $\theta_r = 0$, and since $\delta$ is very small, the critical angle is

$$\theta_c = \sqrt{2\delta} = \sqrt{\frac{4\pi r_0 \rho(\vec{r})}{k^2} \sum_{j=1}^{N} \frac{f_j(0) + f_j'(E)}{Z}}$$

For incident angles $\theta_i \leq \theta_c$ , X-rays are under total external reflection phenomenon. The critical angles of some metals are summarized in TABLE 4.1.

TABLE 4.1 A few examples of useful data used in reflectivity analysis. The table contains the density ρ the critical wavevector $Q_c$, the parameter δ, β, and the critical angle $\theta_c$ (δ, β, and $\theta_c$ are given at $\lambda = 0.77$ Å).

| Materials | Z | density(g/cm$^3$) | $Q_c$(Å$^{-1}$) | δ($10^{-6}$) | β($10^{-8}$) | $\theta_c$ (mrad) |
|---|---|---|---|---|---|---|
| Au | 79 | 19.32 | 0.0794 | 11.83 | -15.734 | 4.86 |
| Cu | 29 | 8.96 | 0.0593 | 6.60 | -3.300 | 3.63 |
| Co | 27 | 8.90 | 0.0594 | 6.63 | -2.737 | 3.64 |
| Mo | 42 | 10.22 | 0.0607 | 6.92 | -1.359 | 3.72 |
| Ti | 22 | 4.54 | 0.0425 | 3.38 | -0.790 | 2.60 |
| Ni | 28 | 8.90 | 0.0604 | 6.84 | -3.114 | 3.70 |
| Zr | 40 | 6.51 | 0.0481 | 4.35 | -0.741 | 2.95 |
| Ta | 73 | 16.65 | 0.0749 | 10.53 | -10.978 | 4.59 |
| Si | 14 | 2.33 | 0.0316 | 1.87 | -0.111 | 1.93 |
| Al | 13 | 2.70 | 0.0334 | 2.10 | -0.098 | 2.05 |
| Co | 27 | 8.90 | 0.0564 | 23.90 | -35.096 | 3.46 |

### 4.1.2 Fresnel equations

The Snell's law and Fresnel equations are derived by imposing the boundary conditions that the electric field and the magnetic field at the interface z = 0 must be continuous (see FIG. 4.1).

Transverse Electric Field: $\alpha_i + \alpha_r = \alpha_t$

Magnetic Field: $\alpha_i \overrightarrow{k_i} + \alpha_r \overrightarrow{k_r} = \alpha_t \overrightarrow{k_t}$

The wavenumber in vacuum is denoted by $k=|\mathbf{k}_i|=|\mathbf{k}_r|$ and in the material it is $nk=|\mathbf{k}_t|$. Since $\theta_i$ and $\theta_r$ are small, by organizing equations above, the Fresneal equations are derived as

$$r = \frac{\alpha_r}{\alpha_i} = \frac{\theta_i - \theta_r}{\theta_i + \theta_r};\ t = \frac{\alpha_t}{\alpha_i} = \frac{2\theta_i}{\theta_i + \theta_r}$$

### 4.1.3 Reflectivity from a homogeneous layer

In case of infinite slab, the reflectivity is calculated from Fresnel equations, as shown in FIG. 4.2 (a). In case of the finite slab, there is an infinite series of possible reflections, and the first three of these are drawn in the figure FIG. 4.2 (b).

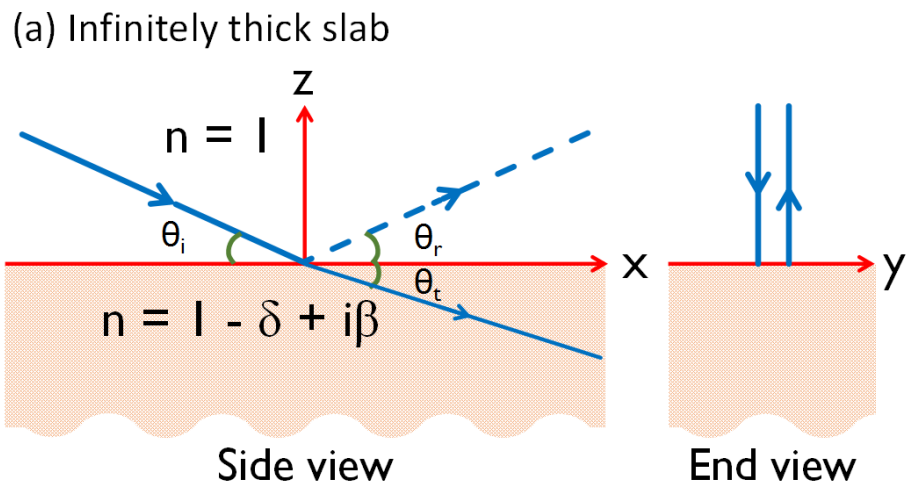

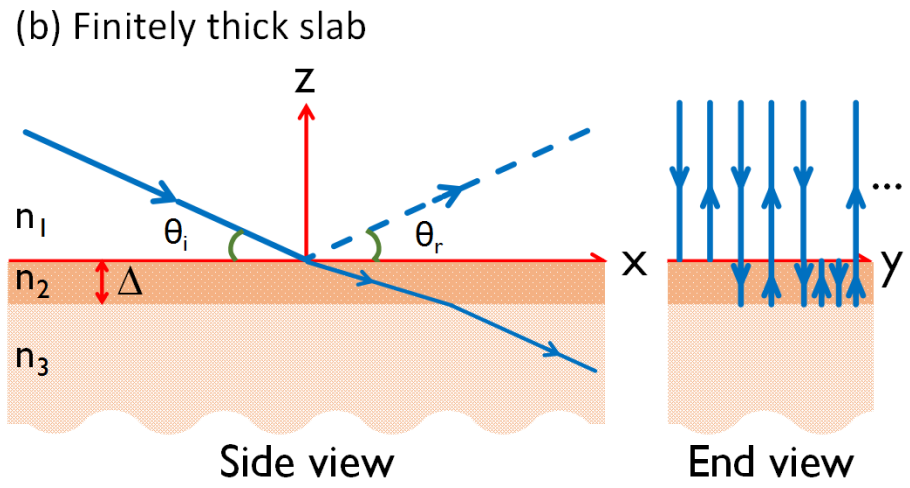


FIG. 4.2 Reflection and transmission from a homogeneous layer of infinite (a) and finite (b) thickness. The finite slab is of thickness Δ and the total reflectivity is the sum of the infinite number of reflections, as indicated in the right panel of (b).[44]

The total amplitude reflectivity from the homogeneous layer is derived:

$$r_{slab} = r_{01} + t_{01}r_{12}t_{10}\sum_{m=0}^{\infty}(r_{10}r_{12}p^2)^m$$

where $p^2$ is the phase factor $p^2 = e^{iQ\Delta}$. $Q = |\mathbf{k_r} - \mathbf{k_i}|$.

The expression can be further simplified by consider $r_{01} = -r_{10}$, $r_{01}^2 + t_{01}t_{10} = 1$,

$$r_{slab} = r_{01} + t_{01}r_{12}t_{10}\frac{1}{1 - r_{10}r_{12}p^2} = \frac{r_{01} + r_{12}p^2}{1 + r_{01}r_{12}p^2}$$

One example of the reflectivity intensity given by the square of the equation is plotted in FIG. 4.3.

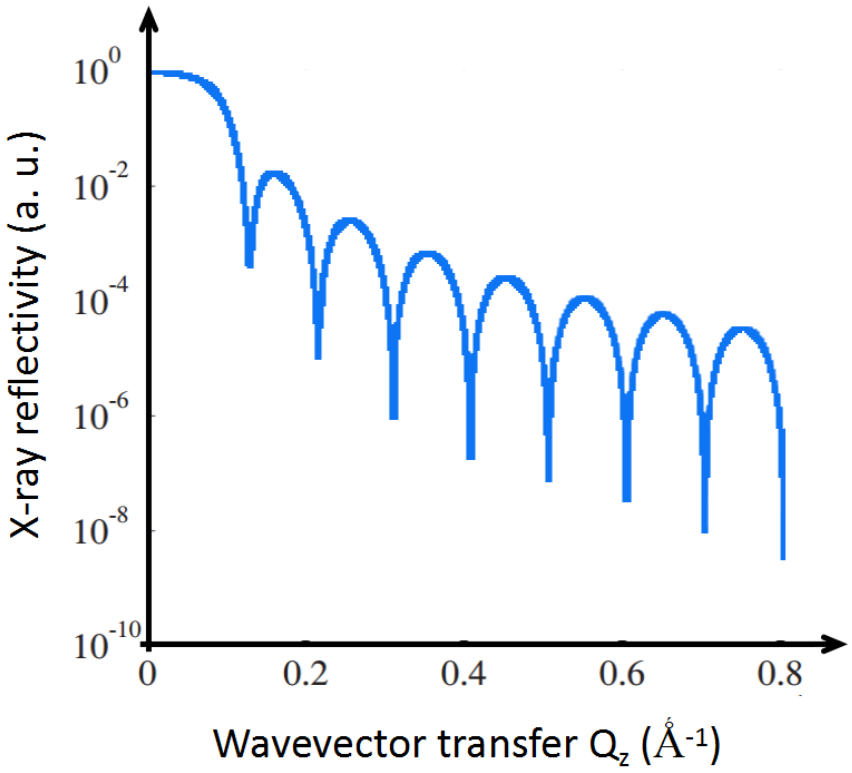


FIG. 4.3 Kiessig fringes from a homogeneous layer of Tungsten. Solid curve: the calculated reflectivity $|r_{slab}|^2$ for a slab of thickness $10 \times 2\pi$ Å. The density of the film is 4.678 electrons per Å$^3$.[44]

### 4.1.4 Reflectivity from a multi-layer

Schematically shows a multilayer stacck consisting of N interfaces. The impinging wave with an amplitude normalized to unity. The X-ray reflectivity from the top surface is calculated by the recursive approach first described by Parratt. If $X_{j+1}$ denotes the ratio of $R_{j+1}$ and $T_{j+1}$ in layer j+1, then $X_j$ for the layer above may be calculated via

$$X_j = \frac{R_j}{T_j} = \exp(-2ik_{z,j}z_j)\frac{r_{j,j+1} + X_{j+1}\exp(2ik_{z,j+1}z_j)}{1 + r_{j,j+1}X_{j+1}\exp(2ik_{z,j+1}z_j)}$$

where $r_{j,j+1}$ is the Fresnel coefficient of the interface j.

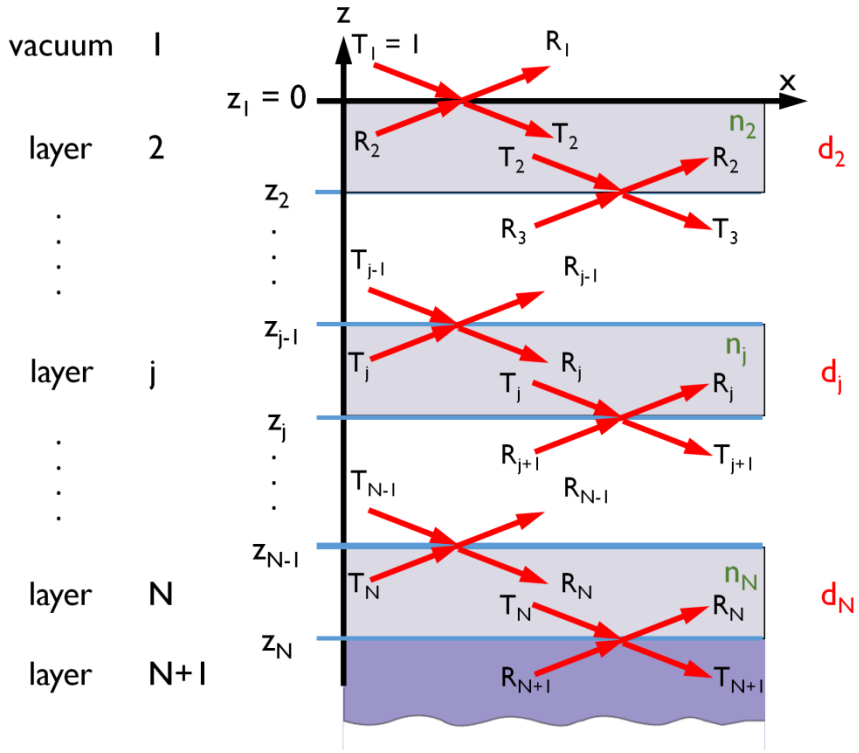


FIG. 4.4 Sketch of a system consisting of N + 1 layers with N interfaces. The incident wave amplitude is normalized to unity, $T_1 = 1$. No wave is reflected from the substrate, i.e. $R_{N+1} = 0$.[42]

### 4.1.5 Mesurement and typical data

FIG. 4.5 shows schematically one of the routine measurement in house or in Synchrotron facility. The X-rays are monochromated and collimated to illuminate the sample at grazing incident angle. According to the reflection law of electromagnetic wave, the reflected X-rays will form an equivalent angle with the sample surface. Such reflected X-rays are detected by a zero dimensional detector such as a scintilation counter (point detector). By scanning the sample and detector (usually called θ/2θ scan), we are able to record the X-ray reflectivity profiles as shown in FIG. 4.5(b). By considerting the physical model, thin films' properties such as thin films' densities, layer thicknesses and roughnesses are obtained from the data.

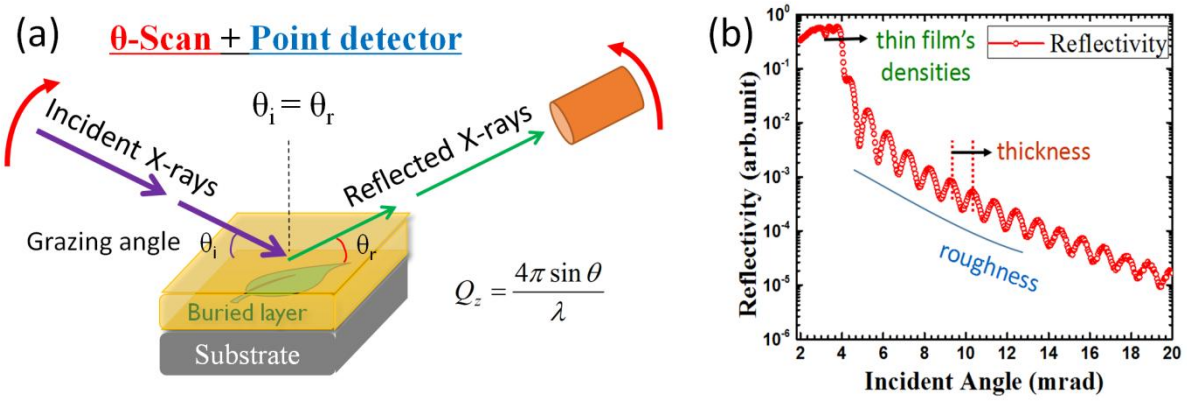

FIG. 4.5 (a) Schematic of a typical X-ray reflectivity measurement. Monochromatic X-rays beam impings on the sample at grazing incident angle, X-rays photons at equivalent reflected angle are collected by a 0D detector. By scanning the grazing incident angle / exit reflected angle and recording the intensity other than the incident angle, the X-ray reflectivity profile is obtained. (b) One example of the X-ray reflectivity data. From the profile, thin films' properties such as thin films' densities, layer thicknesses and roughnesses are retrieved.

### 4.1.6 The missing information in X-ray reflectivity

X-ray reflectivity (XR) is powerful for characterizing buried layers and interfaces in ultrathin films because of its ability to probe the electron density profile along the depth in a non-destructive manner. Since X-rays (especially hard X-rays) possess the wavelength in atomic scale, XR is sensitive to slight structural changes along the depth of layered thin film materials in the order of sub-nanometers or even smaller. Routine X-ray reflectivity assumes the in-plane uniformity of the sample to be measured, the in-plane spatial resolution is missing. When the ultrathin films are not in-plane uniform and there exist several different layered structures depending on the location of the sample, it is difficult for ordinary X-ray reflectivity to give sufficient information to give a whole picture. In this thesis, we describe the addition of spatial resolution and imaging capability to X-ray reflectivity technique.

## 4.2 Novel X-ray reflectivity imaging

The recently developed X-ray reflectivity imaging technique is based on routine X-ray reflectivity and image reconstruction. By applying a monochromatic wide beam to irradiate the whole area of the sample at grazing incident angle, we are able to obtain a one dimensional reflection projection recorded by an area detector. Through collecting such reflection projections at different perspective in-plane angles, we are able to reconstruct the X-ray reflectivity images, which physically means the two dimensional in-plane sptial distribution of X-ray reflectivity.

### 4.2.1 Mesurement and and typical data

FIG. 4.6 gives a sketch of X-ray reflectivity imaging technique. Compared with routine X-ray reflectivity mesurement, we employ a wide monochromatic X-ray beam and area detector for the X-ray reflectivity imaging technique. Other than conducting $\theta/2\theta$ scan, the grazing incident angle is fixed and the sample is rotateed in-plane ($\varphi$-scan) for 180 degrees. During the in-plane angle scan, many reflection projections are recorded by the area detector. The collection of all the reflection projections are stored in a sinogram, where xaxis corresponds to the in-plane angles, yaxis relates to the reflection projection positions. As in the measurement the sample rotates in-plane for half of an circle, the one projection point draw half of an sine period. The X-ray reflectivity imaging technique shares the same image reconstruction scheme from the sinogram as the computerized tomography[70–72].

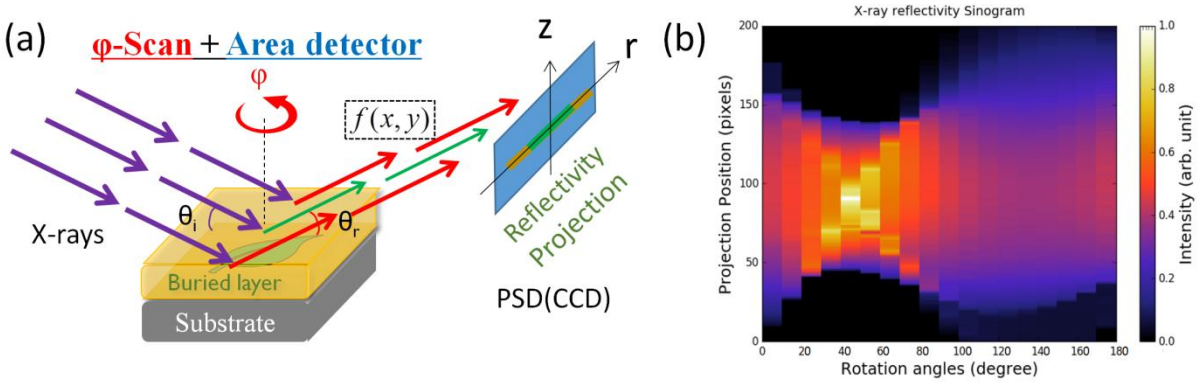


FIG. 4.6 Schematic of the novel X-ray reflectivity imaging. Monochromatic wide X-rays beam impings on the sample at a fixed grazing incident angle, X-rays reflection projections at equivalent reflected angle are recorded by an area detector. By scanning the in-plane angle and recording many reflection projections for 180 degrees, we reconstruct the X-ray reflectivity image by mathematical inversion. (b) One example of the reflection projections data called sinogram obtained from the X-ray reflectivity imaging measurement.

### 4.2.2 Image reconstruction from projections

Generally speaking, the image reconstruction from many projections at different persective angles is a discrete inverse problem. There are many different techniques suitable for different implementations. Among them the two most porpular ones are Fourier based technique Convolution back projection (CBP, or Filter back projection) and Algebraic based techniques. Here only a short introduction of the techniques are given, and more details are easy to be found in many references books[70–73].

#### 4.2.2.1 Convolution Back Projection (CBP)

Mathematically, the reflection projections are the integral reflection intensity along the X-ray forward direction according to the Radon transform[70]:

$$p_{\varphi}(r) = \int_{-\infty}^{\infty} f(r\cos\varphi - z\sin\varphi, r\sin\varphi + z\cos\varphi)dz \tag{2}$$

where φ is the in-plane angle, r is the projection positions (Experimentally pixel number on the CCD), z is the X-rays forward direction, f(x, y) is the 2D reflectivity image, $p_{\varphi}(r)$ is the 1D reflection projection profile at in-plane angle φ.

For the X-ray reflectivity image reconstruction process, we prepared the software based on the convolution back-projection algorithm using Object-Parscal coded GUI. According to Fourier Slice Theorem[71] and Convolution Theorem (see FIG. 4.7), we could back project all convolved reflection projections at different in-plane angles to reconstruct the 2D image:

$$f(x,y) = \int_0^{\pi} g_{\varphi}(x\cos\varphi + y\sin\varphi)d\varphi \tag{3a}$$

where f(x, y) is the 2D reflectivity image, which in other word is the reflectivity distribution at the local position labeled by **(x, y)**. The image is discretized into x-y grid, and the simplest linear interpolation is employed where interpolation is inevitable noticing we need to back project the data at different in-plane angles. $g_\varphi(r)$ is the convolved projection at specific in-plane angle r:

$$g_\varphi(r) = h(r) * p_\varphi(r) \tag{3b}$$

in which $P_\varphi(r)$ is the 1D reflection projection at specific in-plane angle φ, * indicates the sign of convolution and h(r) is the convolution kernel [It is mathematically the same as to multiple the projections with the Ram-Lak filter function H(r) in frequency domain according to the Convolution Theorem]:

$$h(r) = \frac{f_c}{\pi r}\sin(2\pi r f_c) - \frac{1}{(\pi r)^2}\sin^2(\pi r f_c) \tag{3c}$$

where $f_c$ is the cutoff frequency of the Ram-Lak filter in the Fourier space. According to the Nyquist sampling theorem[72], this value was set as 0.5 or smaller when doing the image reconstruction.

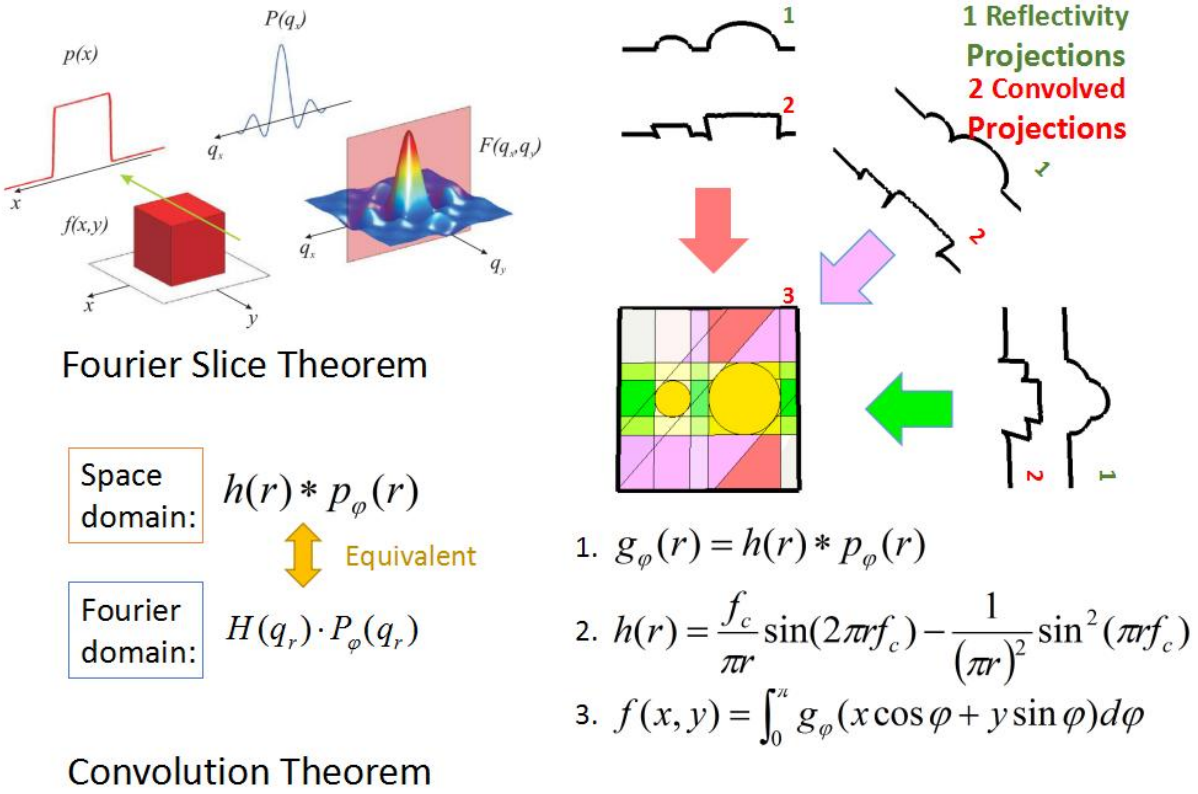


FIG. 4.7 Summary of Convolution back projection method for image reconstruction. Left: The sketch to demonstrate the Fourier slice theore[44] and convolution theorem. Right: The implementation of Convolution backprojection method

#### 4.2.2.2 General Algebraic techniques

The concept of general algebraic tehcniques is to transfer the process to a linear system and then solve the linear equations, as shown in FIG. 4.8. The 2D reflectivity image is at first discrete as a 2D array of pixels and represent by a model vector **m**. According to the Radon transform, the forward projection process is to integrate the pixels values along a specific direction. The operator of integration is reprented by the ray matrix **G**. The data collection procedure is simplified as **Gm = d**, where many inverse algorithms can be used to calculate **m** from **d**. Possible inverse approchs include TSVD (truncated singular value decompostion), ART (algebraic reconstruction technique), SIRT(simultaneous iterative reconstruction tehcnique)

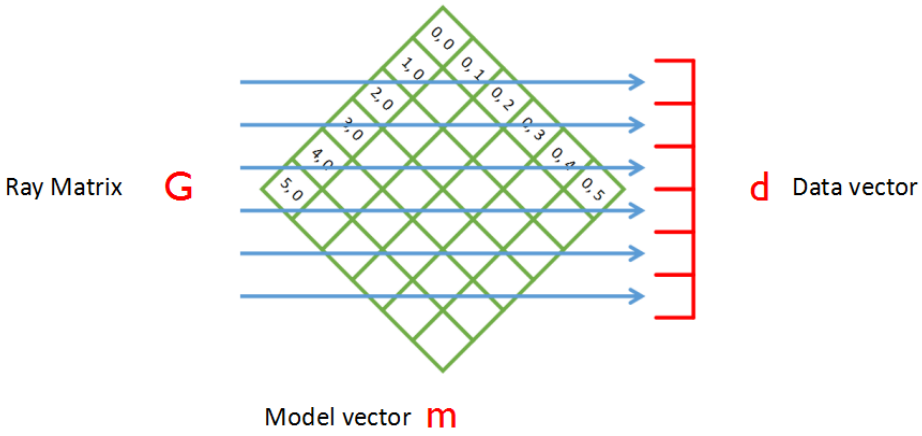


FIG. 4.8 Schematic of the generation of linear system in Algebraic approaches. The 2D image is represented by a 2D array of pixels and stored in a model vector **m**. The forward projection process is to integrate the pixels values along a specific direction. The operator of integration is reprented by the ray matrix **G**. The data collection procedure is simplified as **Gm = d**, where many inverse algorithms can be used to calculate **m** from **d**.

# Chapter 5 Micro-imaging of buried layers and interfaces in ultrathin films by X-ray reflectivity

X-ray reflectivity is a promising technique for characterizing buried layers and interfaces in ultrathin films because of its ability to probe the electron density profile along the depth in a non-destructive manner. While routine X-ray reflectivity assumes the in-plane uniformity of the sample to be measured, it is also quite important to see buried inhomogeneous/patterned layers and interfaces. The present chapter describes the addition of spatial resolution and imaging capability to X-ray reflectivity technique to visualize surfaces and buried interfaces. To visualize quite wide viewing area size quickly, the image reconstruction scheme has been employed instead of the scanning of microbeam. Though the mathematics is quite close to X-ray computer tomography, the technique gives the image contrast caused by the difference in reflectivity at each in-plane point in the thin film sample. By a choosing grazing angle, the image gives inhomogenuity of X-ray reflectivity at the specific wavevector transfer. With a collimated monochromatic synchrotron X-ray beam of 0.05 mm (H) × 8mm (V), the intensity profiles of X-ray reflection projections have been taken at many different in-plane rotation angles, from 0 to 180 deg. We have succeeded in visualizing buried layers and interfaces of the 8 mm dia area with the spatial resolution of better than 20 micron.

Synchrotron radiation takes its name from a specific type of particle accelerator, which generates radiation from charged particles travelling at relativistic speeds in applied magnetic fields which force them to travel along curved or wiggle paths. Synchrotron radiation is produced either in the bending magnets needed to keep the electrons in a closed orbit, or in insertion devices such as wigglers or undulators situated in the straight sections of the storage ring. A synchrotron radiation source provides brilliant X-rays up to 10 decades more brilliant than a laboratory X-ray source. In addition, since the distance between the source (insertion device) and the experimental setup can be quite far (typically 20 m), the angular resolution is much better than that of the laboratory case. The implementation of X-ray reflectivity imaging with Synchrotron radiation is promising. In this chapter I will describe the first results of X-ray reflectivity imaging of buried layers and interfaces in ultrathin films by using synchrotron radiation. Because of the brilliance of synchrotron radiation, the typical measuring time is shorter than 1 min. Three analytical cases have been discussed, (i) imaging of a buried layer and interface covered by a protection layer, (ii) distinguish of different local parts of different thickness in an ultrathin film, and (iii) selective imaging of specific metal in the thin film form.

## 5.1Introduction

X-ray reflectivity (XR) is sensitive to slight structural changes along the depth of layered thin film materials in the order of sub-nanometers or sub-angstroms. Conventional X-ray reflectivity gives 'average' information

over quite a large area, typically $mm^2 \sim cm^2$. When the local structures along the depth are not uniform and there exist several different layered structures depending on the location of the sample, it is necessary to extend X-ray reflectivity's capability in the micro area[74]. Even where the layered structure is almost uniform, usually the local heterogeneity presents the key in solving problems. In modern research, there have been a lot of unsolved but interesting scientific problems in inhomogeneous thin films, and thus it is extremely important to have an imaging technique to search for key points. Invented surfaces and interfaces imaging techniques includes X-ray reflection phase-contrast full field microscopy by Fenter *et al.*[9,75–77], lensless X-ray imaging technique in reflection geometry applying post scattering phase coding by Roy *et al.*[10], three-dimensional coherent X-ray surface scattering imaging technique by Sun *et al.*[11], Ptychographic X-ray imaging technique on crystal truncation rod by Zhu *et al.*[78]. Although these techniques are promising and show possibilities for specific applications, many of these techniques require sophisticated optics, while others rely on coherent X-rays or special samples. We invented a complementary imaging method called X-ray reflectivity imaging (XRI) that is devoted to visualization of buried layers and interfaces in ultrathin films. XRI is realized by introducing an image reconstruction scheme to X-ray reflectivity. Compared with the methods mentioned above, it shows several advantages such as: (1) an optics-free technique, no need of X-ray optics like Fresnel Zone plates or Kirkpatrick–Baez mirrors (KB) to focus X-rays; (2) a user-friendly and easily accessible system. no reliance on coherence of X-rays, while the experiment could be performed even in laboratory; (3) a large scale viewing area of the sample [10 mm × 10 mm, works well both for crystal and non-crystal thin films] without perspective effects due to the image reconstruction scheme: (4) Tunable imaging depth fashion. The image contains the information depending on the X-rays penetration depth, which could be tuned by the incident angle or X-rays energy. The X-ray reflectivity imaging experiments have been performed and the capabilities in the laboratory have been demonstrated in parallel beam geometry[79,80] with a spatial resolution of 1.6 mm and in fan beam geometry[81] with a spatial resolution of 0.18 mm. A synchrotron radiation source provides brilliant X-rays up to 10 decades more brilliant than a laboratory X-ray source. In addition, since the distance between the source (insertion device) and the experimental hutch is quite far (typically 20 m), the angular resolution is much better than that of laboratory cases. Introducing synchrotron radiation to reflectivity imaging is promising. In the chapter, we present the first results of X-ray reflectivity imaging of buried layers and interfaces in ultrathin films by using synchrotron radiation achieving a spatial resolution of 20 μm.

## 5.2 Experimental

We performed the experiment at Beamline 14B[82], Photon Factory, Tsukuba, Japan. The experimental set-up is shown in FIG. 5.1. An insertion superconducting vertical wiggler provided white X-ray beam polarized in the vertical plane. The white and vertically polarized beam was monochromatized by a fixed-exit double-crystal Si(111) monochromator, with an energy resolution of $\sim 10^{-4}$. 16 keV X-rays were chosen because the energy is at around the peak position of the power spectrum.

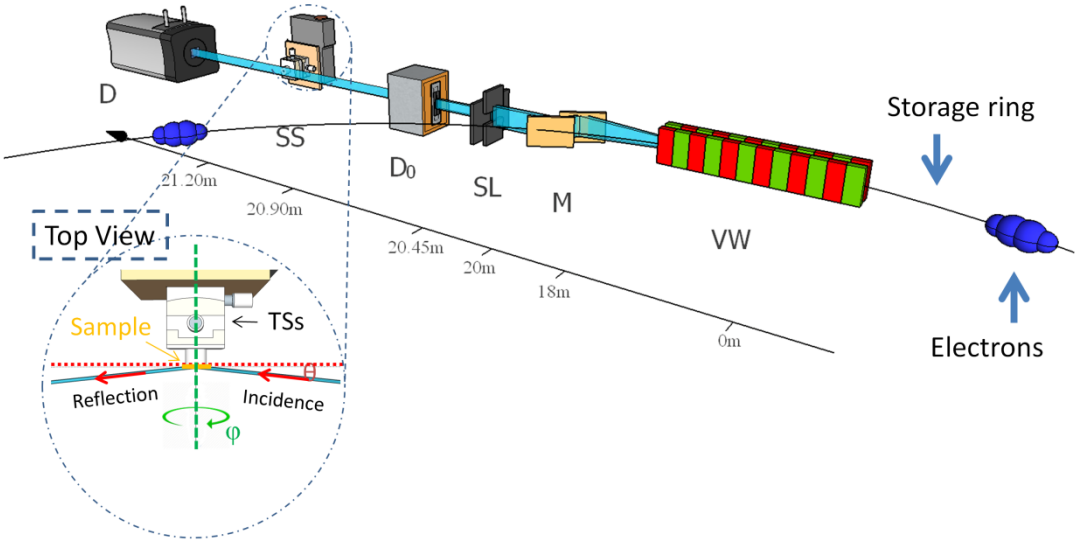


FIG. 5.1 Perspective view of the experimental set-up of X-ray reflectivity imaging technique. Storage ring: orbit of free electron bunches; VW: Vertical Wiggler to generate synchrotron radiation; M: double crystal Monochrometer; SL: 2D slit [1 mm (H) × 8 mm (V)]; $D_0$: Ionization Chamber which records incident X-ray intensity, with a horizontal slit ( 0.05 mm, H ) attached on the top window; SS: Sample stage standing on a high precision goniometer; D: CCD camera with a scintillation film suitable for X-ray detection. Inset is the enlarged image of SS in the top view: TSs: Tilting stages to align the sample to be perpendicular to the in-plane rotational axis. θ is the grazing incident angle and the exit angle between X-rays and sample surface. The thick dashed line in the top view shows the in-plane rotational axis.

The primary beam size was 7 mm (H) × 15 mm (V). A primary collimating 4D slit was set at the furthest upstream side of the experiment hutch, which was 20 m away from the wiggler source, to collimate the beam to 1 mm (H) × 8 mm (V). The X-ray intensity was being monitored all the time during the experiment by an ionization chamber (IC) set 0.45 m behind the 4D slit. In front of the entrance window of the IC a fixed width (50 μm, H) slit was attached to further cut the horizontal width of the beam, thus the final incident beam size was 0.05 mm (H) × 8 mm (V). The sample stage, set 0.45 m downward from the IC, was composed of an in-plane rotational motor, two mutually orthogonal manually micro-tilting stages, a vacuum chuck and a high precision θ/2θ goniometer (not shown in FIG. 5.1). The in-plane rotational motor can scan the in-plane angle from 0 to 180 degree with a positioning accuracy of 0.1 degree. Micro-tilting stages were used to adjust the sample to tilt to the proper angle, thereby ensuring that the sample surface plane was perpendicular to the rotational axis of the in-plane motor. This procedure secured that the incidence was always the same during the in-plane rotational scanning. The vacuum chuck was a specific sample holder designed to hold the flat samples vertically. The components were set on the goniometer, with which the grazing incident angle could be precisely adjusted. At the downstream side, a CCD camera equipped with a scintillation film and capillary optics was set 0.30 m behind the sample as the position sensitive detector, which was used to record reflection projections and was set on the 2θ arm of the goniometer. Further instrumental details are described elsewhere[81].

This technique was inspired by the merits of X-ray reflectivity's high sensitivity for analyzing thin films in depth and the urgent demand for an imaging technique to visualize heterogeneities in thin films. X-ray

reflectivity is measured by θ/2θ scan, where θ is the grazing incident angle[4] and related to the wavevector transfer $Q_z$ (normalized by X-rays wavelength λ) by:

$$Q_z = \frac{4\pi \sin\theta}{\lambda} \tag{1}$$

Howbeit in case of XRI, by performing an in-plane rotational scan at a specific incident angle (or related specific $Q_z$), we reconstructed a reflectivity image at corresponding wavevector transfer $Q_z$, and such a contrast is strongly correlated to the in-depth structure of thin films. Unlike the ordinary X-ray computer tomography in transmission geometry, by employing grazing incidence reflection geometry XRI achieves extremely high sensitivity in depth such as sub nm scale as the same as XR. The signal retrieved from the sample is not the absorption coefficient, but the surfaces and interfaces scattering (reflectivity) from the sample. The reconstructed image is the in-plane spatial mapping (in real space) of X-ray reflectivity at a specific wavevector transfer $Q_z$ (in momentum space). Although this technique gives a 2D image, it also includes in depth information (as will be discussed in Section 6.3). By proper sampling at each in-plane rotational scan (2D image) at each wavevector transfer $Q_z$ (different reflectivity contrast), we could extract the differences inside the ultrathin film and help solve the critical problems in such materials systems.

In order to obtain enough information to reconstruct the reflectivity images, we recorded many 1D reflection projections sampled at in-plane rotational angles evenly from 0 °~ 180 °at fixed grazing incidence. The reflection projections were recorded by the CCD camera as many TIF image files (Note that the reflected X-rays' footprints on the CCD camera are not perfectly 1D projections but narrow rectangles as the incident X-rays horizontally has the width of 50 μm). In order to efficiently handle many TIF images, we use many Python open-source Python libraries designed for scientific computing such as numpy, matplotlib, and Tkinter. For the data reduction and processing, we prepared Python codes to read each TIF file, specify the area of interests and integrate the reflection rectangles into 1D projection with the batch mode compatibility. Mathematically, the reflection projection is the integral reflection intensity profile along the X-ray forward direction according to the Radon transform[70]:

$$p_\varphi(r) = \int_{-\infty}^{\infty} f(r\cos\varphi - z\sin\varphi, r\sin\varphi + z\cos\varphi)dz \tag{2}$$

where φ is the in-plane angle, r is the projection positions (Experimentally pixel number on the CCD), z is the X-rays forward direction, f(x, y) is the 2D reflectivity image, $p_\varphi(r)$ is the 1D reflection projection profile at in-plane angle φ .

For the X-ray reflectivity image reconstruction process, we prepared the software based on the convolution back-projection algorithm using Object-Parscal coded GUI. According to Fourier Slice Theorem[71] and Convolution Theorem, we could reconstruct an XRI image from 1D projections by back projecting all convolved reflection projections at different in-plane angles:

$$f(x,y) = \int_0^{\pi} g_\varphi(x\cos\varphi + y\sin\varphi)d\varphi \tag{3a}$$

where f(x, y) is the 2D reflectivity image, which in other word is the reflectivity distribution at the local position labeled by **(x, y)**. The image is discretized into x-y grid, and interpolation is inevitable noticing we need to back project the data at different in-plane angles. Here the simplest linear interpolation is employed. $g_\varphi(r)$ is the convolved projection at a specific in-plane angle:

$$g_\varphi(r) = h(r) * p_\varphi(r) \tag{3b}$$

in which $P_\varphi(r)$ is the 1D reflection projection at a specific in-plane angle φ, * indicates the sign of convolution and h(r) is the convolution kernel [It is mathematically the same as to multiply the projections with the Ram-Lak filter function H(r) in frequency domain according to the Convolution Theorem]:

$$h(r) = \frac{f_c}{\pi r}\sin(2\pi r f_c) - \frac{1}{(\pi r)^2}\sin^2(\pi r f_c) \tag{3c}$$

where $f_c$ is the cutoff frequency of the Ram-Lak filter in Fourier space. According to the Nyquist sampling theorem[72], this value was set as 0.5 or smaller when conducting the image reconstruction.

## 5.3 Results and Discussion

As discussed in the previous section, an XRI image is a spatial mapping of X-ray reflectivity at a specific $Q_z$. In order to decide $Q_z$ of interest, we firstly measured X-ray reflectivity by scanning grazing incident angle/exit angle (θ/2θ) at a fixed in-plane rotational angle φ before performing the X-ray reflectivity imaging measurement. In X-ray reflectivity, X-ray reflection projections at each incident angle were recorded by the CCD camera and the reflection projections were plotted other than $Q_z$, as shown in FIG. 5.2(a), FIG. 5.4(a), and FIG. 5.6(a). In the X-ray reflectivity imaging experiment, grazing incident angle was fixed, and reflection projections at different in-plane angles were recorded by the CCD camera. This section describes XRI's imaging sensitivity of thin films in three different analytical cases by using three different samples.

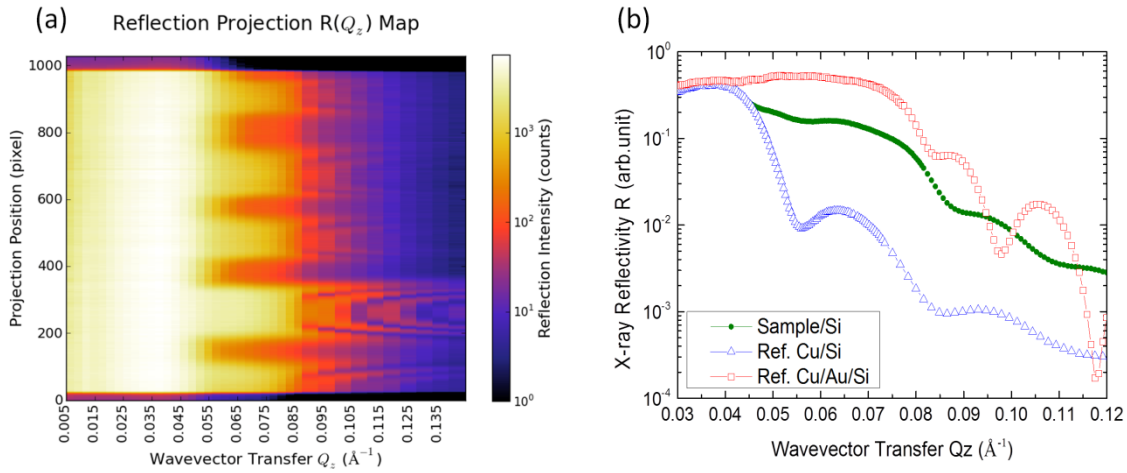


FIG. 5.2 X-ray reflection profiles of the Copper/Gold(Pattern)/Si sample and its reference samples. (a) Local reflectivity profiles of the patterned sample measured at the SR facility as the reflection projection map of the wavevector transfer $Q_z$.

The scanning step for the measurement is $\Delta Q_z = 0.003$ Å$^{-1}$, and the data are plotted in logarithmic colorscale. (b) Ordinary X-ray reflectivity of the patterned sample (circle), the reference uniform Copper/Gold/Si sample (rectangle) and the reference uniform Copper/Si sample (triangle) measured by a laboratory X-ray reflectometer.

### 5.3.1 Imaging buried layers

X-rays, as is commonly known, can easily penetrate the sample and reach the buried layers and interfaces. By controlling the grazing incidence, one can manipulate the penetration depth of X-rays into a thin film, and change electric field in-depth distribution in the sample[83]. X-ray reflectivity is a measurement scanning grazing incidence and probing the structure of thin films in depth. By choosing specific grazing incidence (thus wavevector transfer $Q_z$), one can obtain a proper electric field and then emphasize specific layers or interfaces in the sample. Here we demonstrate how we visualized a buried layer and an interface of a layered thin film.

The sample was an ultrathin film consisting of a homogeneous copper layer and a gold pattern layer on a silicon substrate (size of the substrate: $10 \times 10 \times 0.5$ mm$^3$). The sample was made by an Emitech sputter coater. The layered thin film was prepared according to the following procedure: (1) the silicon substrate was put into the sputter chamber and covered by a mask made of kapton film. The mask was pre-cut with the designed pattern: a circle containing five bars (width: ~1mm) of different lengths, as shown in FIG. 5.3(f). Thereafter the chamber of the sputter machine was pre-vacuumed to < 3 Pa and filled with Argon gas. High voltage was applied between the gold target (original material) and the substrate to ionize Ar atoms and gold particles were then sputtered off from the target by ionized argon atom and deposited onto the substrate. The sputtering condition for the gold layer was as follows, Ar pressure: 8 Pa, ion current: 6 mA, sputtering time: 60s. (2) The gold foil target was replaced by a copper foil target. The mask was then removed. The chamber of the sputtering machine was again pre-vacuumed to < 3 Pa and filled with Argon gas. High voltage was applied between the copper target and the sample and copper was sputtered onto the patterned sample. The sputtering condition for the copper layer was as follows, Ar pressure: 8 Pa, ion current: 10 mA, sputter time: 60s. The copper layer covered the gold pattern uniformly and made the gold pattern a buried layer. Reference samples were also prepared as follows: Ref. Cu/Au/Si sample was made by the same procedure (1) and (2) under the same conditions, except that no mask was applied in the procedure (1), thus sample Ref. Cu/Au/Si consists of a uniform gold layer covered by a homogeneous copper layer. Ref. Cu/Si sample was prepared by only procedure (2), thus the Ref. Cu/Si sample is composed only of a homogeneous copper layer on the substrate.

In order to help understand the merits and physical meaning of XRI images, the X-ray reflectivity profiles of the patterned sample and uniform reference samples were measured by an ordinary X-ray reflectometer in the laboratory, as shown in FIG. 5.2(b): rectangle (copper / gold / Si sample, which references the patterned part), triangle (copper / Si sample, which references the pattern-free part) and solid circle (copper / pattern gold / Si sample). To obtain the density, thickness and roughness of the copper cover layer and that of the gold pattern layer, we fitted the $Q_z$-dependent data of the reference samples (rectangle and triangle profiles) in FIG. 5.2(b) using reflectivity analysis program GenX based on the Parratt formalism[69]. First, the simple one layer model was used to fit the data of the copper / Si sample. Second, we applied two layer model to fit the data of copper / gold / Si sample, while kept the same parameters for the top layer as that extracted from the copper / Si sample. Third, we assume the copper / pattern gold / Si sample has similar in-depth structures from the reference samples. The

extracted in-depth structure information is given in TABLE 1. The thickness of the copper layer is around 172 Å with roughness of 22 Å, while the thickness of the gold layer is 212 Å with roughness of 11 Å. The density of the gold layer extracted from the X-ray reflectivity is 19.17 g/cm$^3$, which is very close to the standard value (19.32 g/cm$^3$). However, the copper layer is a relatively low density layer with the density of around 5.17 g/cm$^3$, while the standard value of copper is 8.96 g/cm$^3$. The density of the Si substrate is 2.33 g/cm$^3$, with roughness of 6 Å.

TABLE 5.1 Summary of the in-depth structure information extracted from ordinary X-ray reflectivity profiles of uniform reference samples. Superscripts a and b indicate the two different reference samples.

| Layer | [a] Pattern Part - Ref. Au/Cu/Si, [b] Other part - Ref. Cu/Si | | | |
|---|---|---|---|---|
| | Density(g/cm$^3$) | $Q_c$(Å$^{-1}$) | Thickness(Å) | Roughness(Å) |
| Cu$^{a,b}$ | 5.17$^{a,b}$ | 0.043$^{a,b}$ | 172$^{a,b}$ | 22$^{a,b}$ |
| Au$^{a}$ | 19.17$^{a}$ | 0.078$^{a}$ | 212$^{a}$ | 11$^{a}$ |
| Si$^{a,b}$ | 2.33$^{a,b}$ | 0.032$^{a,b}$ | --- | 6$^{a,b}$ |

As X-ray reflectivity always assumes in-plane uniformity of samples, the measurement of X-ray reflectivity profiles from the heterogeneous sample was quite difficult. The reason could be (1) heterogeneity may complicate optical alignments; (2) the viewing area (footprint of X-rays) on the sample surface changes when we scan the grazing incident angle during the measurement, which makes the measured reflectivity a varying weighted mixture of reflectivities at different locations. In this research, the sample was positioned in the center of the viewing area, and the measured reflectivity profile: (a) is a mixture of the different lateral parts of the sample; (b) has a different weighting factor for the lateral parts at different incidences. FIG 3.2 (a) is a combination of routine reflectivity scans with a position sensitive detector. The sample was fixed on the sample holder in the direction as shown in FIG 3.3(f), where X-rays impinged on the sample from right and the CCD recorded the reflection projections (the layout of the setup is displayed in FIG. 5.1). The pattern structure was captured by the reflection projections of FIG 3.2 (a). One can see a sharp intensity drop at around $Q_z$ = 0.045 Å$^{-1}$, which corresponds to the critical wavevector transfer $Q_c$ of copper. The value is the same as that extracted from the conventional X-ray reflectivity profile of the Ref. Cu/Si sample (nearly 0.043 Å$^{-1}$) considering the low $Q_z$ resolution ($\Delta Q_z$ = 0.003 Å$^{-1}$). Another sharp drop for some parts of the profiles is around $Q_z$ = 0.080 Å$^{-1}$, which corresponds to the critical wavevector transfer $Q_c$ of gold. The value equals that extracted from the conventional X-ray reflectivity profile of the Ref. Au/Cu/Si sample (nearly 0.078 Å$^{-1}$). The critical wavevector transfers $Q_c$s for each layer, as shown in TABLE I, are given by:

$$Q_c = 2k\sqrt{2\delta} = 4\sqrt{\pi\rho r_0\left(1+\frac{f'}{Z}\right)}, \tag{4}$$

where k is the wavenumber [k = 2π/λ], δ is the deviation of refractive index n from unit [related to the scattering properties of the medium], ρ is the electron density, $r_0$ is classical radius of electron, f' is the dispersion correction for the element, Z is the atomic number. In the high $Q_z$ range ($Q_z$ = 0.08 to 0.14 Å$^{-1}$), the profiles show ripple structures at the pattern positions. These ripples originate from thickness differences of the pattern, as will be discussed later in the X-ray reflectivity images.

In the X-ray reflectivity imaging experiment, by looking at the X-ray reflectivity profiles in FIG. 5.2, five different $Q_z$s (grazing incidence was changed in the experiment, with X-rays' wavelength fixed) were chosen to emphasize different in-depth structures in the sample. 36 reflection projections (views) were measured to reconstruct the X-ray reflectivity image, which is enough to resolve the pattern (1 mm). Exposure time for each projection is 1s. Thereby the total measuring time for 1 image is 36 sec. FIG. 5.3 (a) ~ (e) are the reconstructed images from the experiment at different wavevector transfers $Q_z$s. The images were reconstructed by the homemade software utilizing the convolution back-projection algorithm. The cutoff frequency was set as 0.2 to compensate for the sparse views.

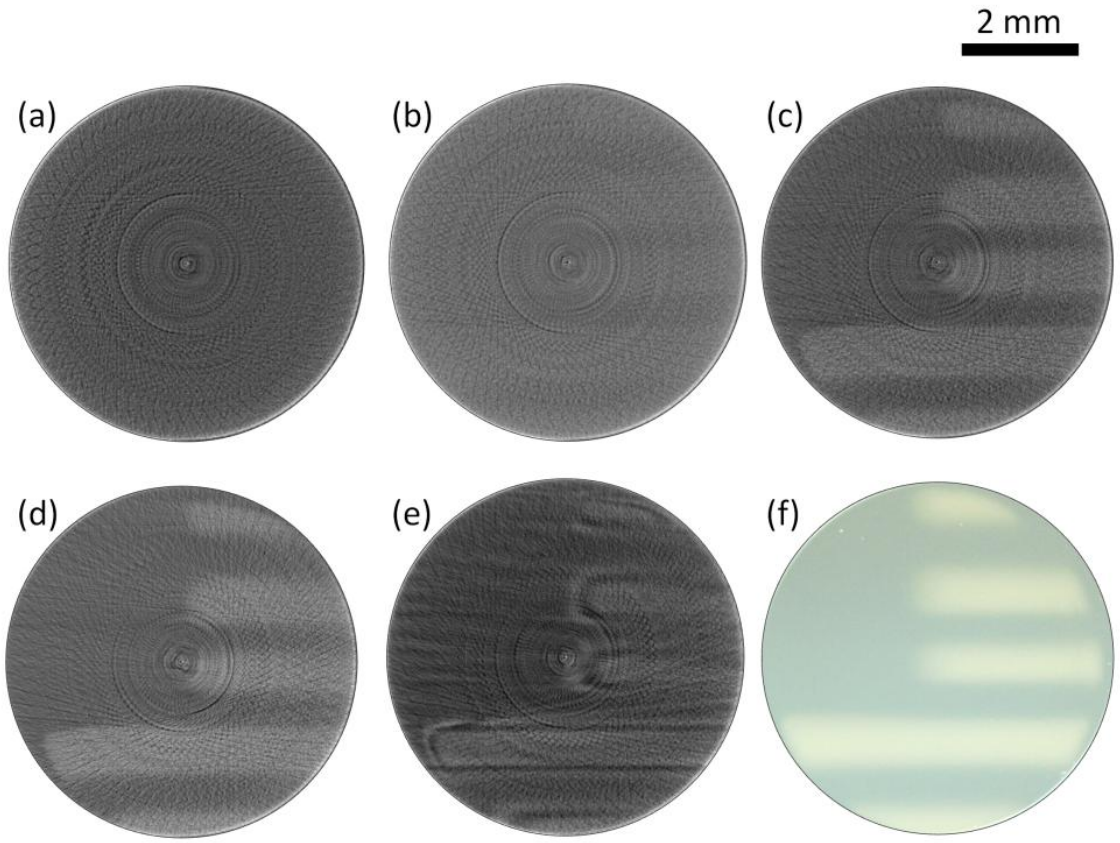


FIG. 5.3 Reconstructed X-ray reflectivity images of the Copper/Gold(Pattern)/Si sample at different of wavevector transfers. Parameters for image reconstruction: 36 views, Cutoff frequency for Ram-Lak filter: 0.2. (a) $Q_z$ = 0.024 $Å^{-1}$; (b) $Q_z$ = 0.049 $Å^{-1}$; (c) $Q_z$ = 0.057 $Å^{-1}$; (d) $Q_z$ = 0.073 $Å^{-1}$; (e) $Q_z$ = 0.098 $Å^{-1}$. (f) Optical image of the pattern sample before coating with copper uniform layer. The image was trimmed to have the same scale as the reconstructed images. Scale bar on the top right shows 2 mm.

FIG. 5.3 (a) shows the reconstructed XRI image at $Q_z$ = 0.024 $Å^{-1}$, which is in the region of total external reflection for the copper layer, as the $Q_c$ of the top copper layer is 0.043 $Å^{-1}$. At this $Q_z$, there is only an evanescent wave propagating just several angstroms below the surface, which means the imaging is very surface sensitive at this $Q_z$. At this $Q_z$, X-rays are totally reflected, and as we deposited a uniform copper layer, the image shows homogeneous contrast. Imaging at this wavevector transfer could be used to detect the surface structure such as roughness and top layer in-plane density differences.

FIG. 5.3 (b) shows the reconstructed XRI image at $Q_z = 0.049$ Å$^{-1}$, which is just beyond the $Q_c$ of the copper layer and far below the $Q_c$ of the gold layer (0.078 Å$^{-1}$). We can see a weak contrast of the pattern (or the buried gold layer) with other parts. At this $Q_z$, there are differences between the pattern part and other parts: (a) in the pattern region, a specific fraction (depends on the $Q_z$ and surface properties of the top layer) of X-rays penetrate the top copper layer and reach the gold pattern surface. Such X-rays reaching the copper/gold interface are totally reflected by the gold. Other fractions of X-rays are reflected by the top surface, thus the reflectivity is still unity if we ignore the small fraction of absorption. (b) In the other pattern-free region, a small fraction of X-rays penetrate the top copper layer and reach the silicon surface and are weakly reflected. ($Q_c$ of Si is 0.032 Å$^{-1}$). Only that part reflected by the top copper surface contributes to the intensity of reflectivity, thus the reflectivity is smaller than unity, as shown by triangles profile in FIG. 5.2 (b). Imaging at this wavevector transfer can be applied to detect the structure of the first layer such as its local thickness differences.

FIG. 5.3 (c) and (d) display the reconstructed XRI images at $Q_z = 0.057$ Å$^{-1}$ and $Q_z = 0.073$ Å$^{-1}$, which are two wavevector transfers in the region between $Q_c$ of the copper layer and $Q_c$ of the buried gold layer. In this region, the reflectivity from copper dropped to $10^{-2}$ while that from the copper/gold layer is still close to unity. This region corresponds to the 1$^{st}$ fringes region of the copper layer, and the reflectivity changes sinusoidally. Thereby the two images at $Q_z = 0.057$ Å$^{-1}$ and $Q_z = 0.073$ Å$^{-1}$ show different contrasts. At these wavevector transfers the copper/gold interface is strongly enhanced, and imaging at such wavevector transfers can effectively probe the interface properties.

FIG. 5.3 (e) shows the reconstructed XRI image at $Q_z = 0.098$ Å$^{-1}$, which is beyond the $Q_c$ of the gold layer. At this wavevector transfer: (a) in the pattern region, X-rays reaching the gold pattern surface can also penetrate the gold layer. Such X-rays are multi-reflected weakly by the gold/silicon interface and gold/copper interface, interfering with each other[6]. The interference pattern is related to the gold layer thickness. (b) In the other pattern-free region, part of the X-rays penetrate the top copper layer and reach the silicon surface and are weakly reflected ($Q_c$ of Si is 0.032 Å$^{-1}$). Although we assume the gold film has the same thickness (212 Å) at different in-plane positions, the actual thickness of the pattern differs from position to position. In the reconstructed image, the patterns have a bright halo structure, which corresponds to the difference in thickness inside the gold film. At this $Q_z$, that ring structure is enhanced because reflectivity is the peak at the ring positions, while the adjacent black valley is related to roughly the dip position in the reflectivity curve at this area. Imaging at such wavevector transfers can be applied to detect differences in the buried layer's structure such as the roughness and the thickness. Further clarifications of the thickness contrast (shift of interference fringes influencing the image contrast) are discussed in Section 3.3.1.

### 5.3.2 Distinguishing different thickness

Ordinary surface characterization techniques only have the ability to image the morphology of the surface, and they cannot probe far into the sample. If the sample has in-plane thickness variation, the surface characterization technique usually needs to go to the edge of the object to ascertain an absolute value. Sometimes the thickness of the film changes gradually without a sharp edge, and in such case it is difficult to know the thickness difference. X-ray reflectivity imaging could give a solution to this problem as X-rays could penetrate

the sample and reach the buried interface. This section describes the XRI's imaging sensitivity of different layer thicknesses inside thin films.

The sample was an ultrathin film which consists of two gold isolated islands (Diameter: 0.5mm) of different thicknesses on a silicon substrate. The sample was made by the Emitech sputter coater. The layer consisting of two gold isolated islands was prepared using the following procedure: (1) the silicon substrate was set into the sputter chamber and covered by a mask made of kapton film. The mask was pre-cut with the designed pattern: one pinhole (Diameter: 0.5mm). The chamber of the sputter machine was pre-vacuumed to < 3 Pa and filled with Argon gas. High voltage was applied between the gold target (original material) and the substrate to ionize Ar atoms and gold was then deposited onto the sample substrate. The sputtering condition was as follows, Ar pressure: 10 Pa, ion current: 6 mA, sputtering time: 60s. (2) The mask was then shifted 1~2mm to one direction (The mask was still covering the whole area of the substrate). The chamber of the sputter machine was pre-vacuumed again to < 3 Pa and filled with Argon gas. High voltage was applied and the sputtering condition for the second island was as follows, Ar pressure: 10 Pa, ion current: 6 mA, sputtering time: 120s. Thus two laterally identical islands with different thicknesses were deposited on the silicon substrate.

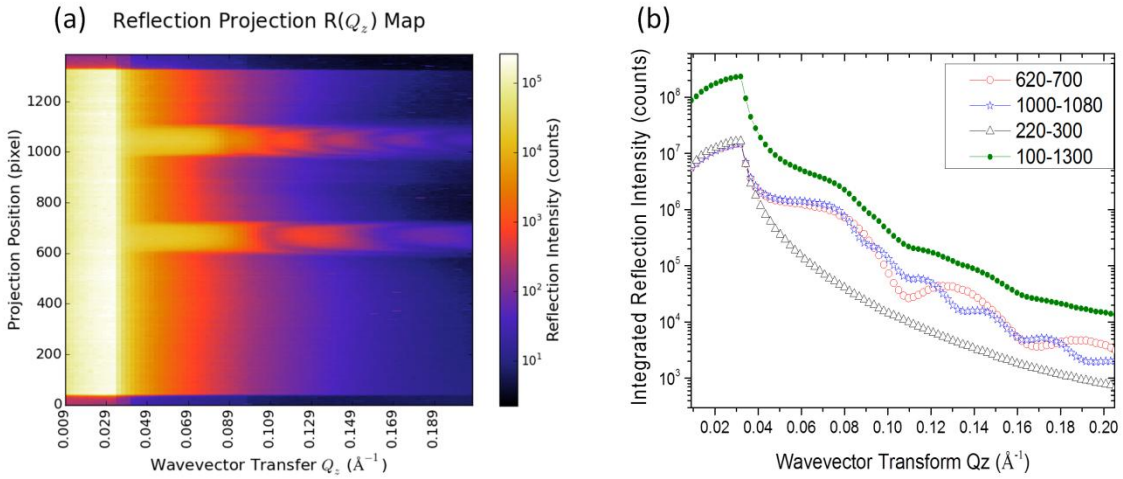


FIG. 5.4 X-ray reflection profiles of the Gold pattern (two islands) /Si sample: two islands' thicknesses are 168 Å and 84 Å. (a) local reflectivity profiles of pattern sample measured at the SR facility as the reflection projection map of the wavevector transfer $Q_z$, The scanning step for the measurement is $\Delta Q_z$ = 0.002 Å$^{-1}$, the data are plotted in logarithmic colorscale. The sample was placed at the center of the sample chuck to ensure the two islands were always in the radiation area during the θ/2θ scan. (b) Extracted X-ray reflectivity profiles integrated in the specific pixel range (see Left figure y-axis): middle island [620 - 700] (circle), top island [1000 - 1080] (star), bare Si [220-300] (triangle), all over the sample surface [100 - 1300] (solid circle).

It is obvious that reference samples are not necessarily needed for such a simple pattern. We measured the reflectivity of these two gold isolated islands separately by θ/2θ scan and the position sensitive detector (CCD camera), as shown in FIG. 5.4 (a). It is necessary to note that the footprint length (L) along the X-rays forward direction on the sample is directly related to the incident angle and the beam width (w):

$$L = w / \sin\theta \tag{5}$$

where L is the length of the footprint on the sample, w is the horizontal width of X-ray beam (50 μm in this experiment), and θ is the incident angle of X-rays. Although at the low $Q_z$ region (viz. low incident angle θ, $Q_z$ <

0.032 $Å^{-1}$, the $Q_c$ of Si), the footprint of incident X-rays are relatively large and the reflection projections include information of the reflectivities from the Si, the reflection intensities are almost 100% from the gold film at the high $Q_z$ region. We can see a sharp intensity drop at around $Q_z$ = 0.032 $Å^{-1}$ in FIG. 5.4 (a), which corresponds to the critical wavevector transfer $Q_c$ of silicon, showing the contribution of the reflectivities from the silicon substrate at the low $Q_z$ region [$Q_z$ < 0.032 $Å^{-1}$]. Another obvious intensity drop is at the two isolated islands positions for $Q_z$ = 0.080 $Å^{-1}$, which corresponds to the critical wavevector transfer $Q_c$ of gold. FIG. 5.4 (b) shows the reflectivity profiles integrating specific pixels range from the FIG. 5.4 (a): middle island [620 - 700] (circle), top island [1000 - 1080] (star), bare Si [220 - 300] (triangle), all over the sample surface [100 - 1300] (solid circle). It is necessary to point out that only the reflectivity profile of bare Si is a pure profile from Si, while other profiles are all mixtures of the reflectivities from gold and silicon. The reflectivity profiles including the middle and top islands have two plateaus: 0.009 $Å^{-1}$ ~ 0.032 $Å^{-1}$ and 0.04 $Å^{-1}$ ~ 0.08 $Å^{-1}$, which correspond to the total reflection region of silicon substrate and gold film.

We conducted a simple calculation to see the mixture ratio of gold to silicon in the area irradiated by the incident X-ray beam:

$$\frac{S_{gold}}{S_{total}} = \frac{R_{total}(Q_{z1}) - R_{silicon}(Q_{z1})}{R_{total}(Q_{z2})} \div \frac{w_{accept}(Q_{z1})}{w_{accept}(Q_{z2})} \tag{6}$$

where $S_{gold}$ is the surface area of the gold island, $S_{total}$ is the surface area of X-rays footprint in the pixel range (e.x. 1000 ~ 1080), $R_{total}(Q_z)$ and $R_{silicon}(Q_z)$ are the reflection intensity from the gold included area and bare silicon area at a specific $Q_z$, respectively, $w_{accept}(Q_z)$ is the accepted horizontal width of X-rays [As the $Q_z$s chosen in this calculation are small enough that the X-rays footprint is always larger than the sample size (10 mm), the accepted X-rays (width) is linearly related to sin θ according to Eq. (5)]. The ratio can be calculated with Eq. (6) by looking up the reflection intensities at $Q_z$ = 0.0319$Å^{-1}$ and at 0.0638$Å^{-1}$ in FIG. 5.4 (b):

$$S_{gold} / S_{total} = (1.36\times10^{6} - 1.10\times10^{5}) \div (1.51\times10^{7}) \div 2 = 4.14\% \tag{7}$$

where $1.36\times10^{6}$ is the reflection intensity from the mixture area {[(1080 – 1000) × 6.45 μm ] × 10 mm} at $Q_z$ = 0.0638$Å^{-1}$, $1.10\times10^{5}$ is the reflection intensity from pure silicon {[(300 – 220) × 6.45 μm ] × 10 mm} at $Q_z$ = 0.0638$Å^{-1}$, $1.51\times10^{7}$ is the reflection intensity from the mixture area {[(1080 – 1000) × 6.45 μm ] × 10 mm} at $Q_z$ = 0.0319$Å^{-1}$. In order to compare the reflection intensities, we need to consider the accepted X-rays intensity and include the weighting factor $w_{accept}$ ($Q_z$ = 0.0638$Å^{-1}$) / $w_{accept}$ ($Q_z$ = 0.0319$Å^{-1}$) = 2. Assuming the perfect round area of the gold island, this calculation implies that the diameter of the gold island is $2\times\sqrt{[10\times(80\times0.00645)\times4.14\%]/\pi} = 0.52$ mm, which is quite close to the designed value.

The thickness of the middle island extracted from the reflectivity profile in FIG. 5.4 (b) is around 83 Å, and the thickness of the top island is 180 Å, which is around twice that of the middle island (related to the doubled deposition time in the sample preparation procedure). Since the X-rays viewing area and the weighting factors for the mixture of gold and silicon are different at different incident angle, we only fitted the interference fringes position [only influenced by the gold film] of the $Q_z$-dependent data in FIG. 5.4 (b) and extracted the thicknesses of the gold patterns. In the high $Q_z$ range ($Q_z$ = 0.08 to 0.20 $Å^{-1}$), the reflection projection also shows ripple structures at the pattern positions. As no additional cover layer was presented, these ripple structures are

obviously due to the thickness differences in each gold island. We sliced at each pixel in FIG. 5.4 (a) and plotted many X-ray reflectivities profiles. Although the footprint of incident X-rays always cover the whole pattern, we fitted the interference fringes position of those reflectivity profiles and extracted the semi-local thicknesses [averaged along X-rays forward direction] in the gold island. The thicknesses of each slice labeled by each pixel value (p) of the middle island in FIG. 5.4 (a) are summarized in TABLE II. At the edge of the island (p = 620), the film is thinnest (76 Å). When approaching the center of the island, the thickness increases. The uniform plateau has the thickest value (88 Å). According to the analysis, the island is made of a uniform thickness plateau (650 - 690) near the center and a slope (620 - 640) at the edge. As it is mentioned above, the values in TABLE II are still averaged values - averaging along the X-rays forward direction. That's one reason why we urgently need the present technique to obtain a 2D image of reflectivity. The top island has a similar structure, and here we omit the discussion.

TABLE 5.2 Summary of thicknesses of each slice labeled by each pixel value of the middle gold island in FIG. 5.4 (a).

| Pixel Position | 620 | 630 | 640 | 650 |
|---|---|---|---|---|
| Thickness (Å) | 76 | 80 | 82 | 86 |
| Pixel Position | 660 ~ 680 | | 690 | 700 |
| Thickness (Å) | 88 | | 87 | 85 |

For the gold islands sample, we also chose five different $Q_z$s (grazing incidence was changed in the experiment, with X-rays wavelength fixed) to emphasize different in-depth structure in the sample. 72 reflection projections (views) were measured to reconstruct the X-ray reflectivity image, which is enough to resolve the pattern (0.5 mm). The total measuring time for 1 image was 72 sec. FIG. 5.5 (a) - (e) are the reconstructed images from the experiment at different wavevector transfers $Q_z$s. The reconstruction algorithm used here was also the convolution back-projection algorithm with the cutoff frequency 0.5.

FIG. 5.5 (a) shows the reconstructed XRI image at $Q_z = 0.030$ Å$^{-1}$, which is in the region of total external reflection for both silicon and gold, as the $Q_c$ of the silicon and gold are 0.032 Å$^{-1}$ and 0.078 Å$^{-1}$ respectively. At this $Q_z$ , the reflectivity from the silicon substrate and gold islands are both unity, so there is no contrast between the pattern and the other pattern-free part in the image. At this $Q_z$, X-rays are totally reflected, and the image shows homogeneous contrast.

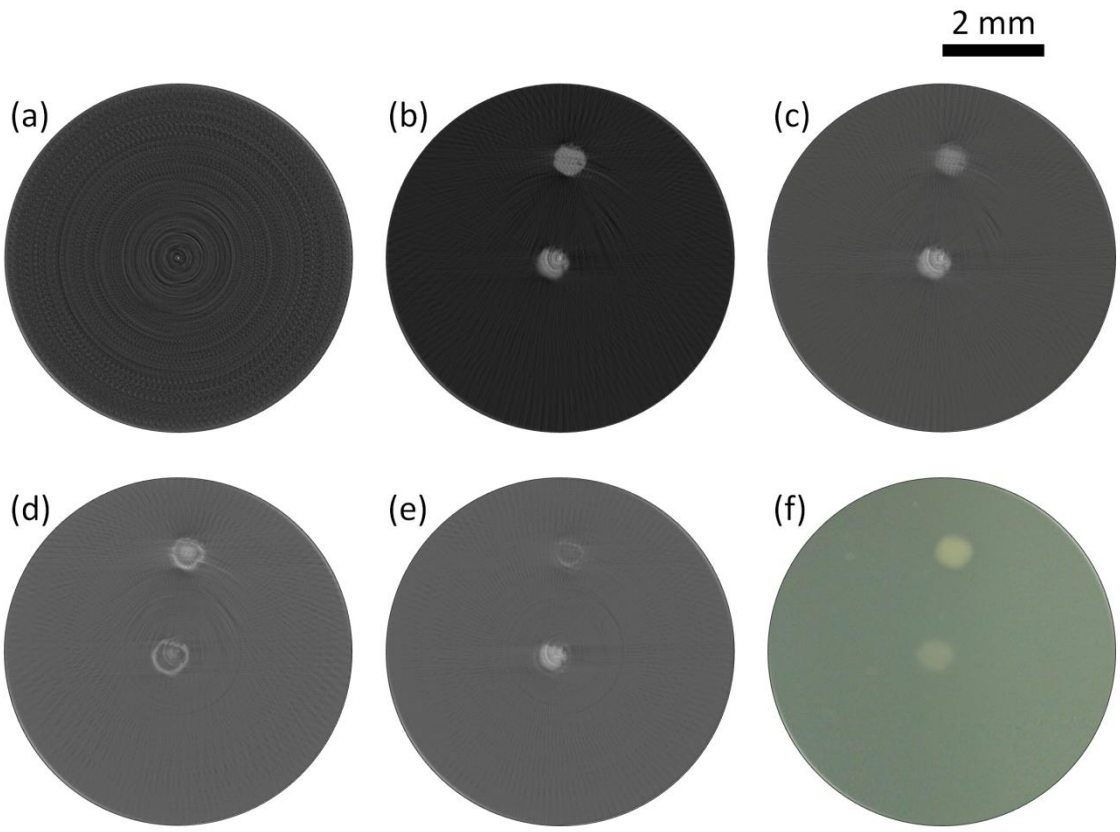


FIG. 5.5 Reconstructed X-ray reflectivity images of the Gold (two islands with different thicknesses)/Si sample at different wavevector transfers. Parameters for image reconstruction: 72 views, Cutoff frequency for Ram-Lak filter: 0.5. (a) $Q_z$ = 0.030 $Å^{-1}$; (b) $Q_z$ = 0.068 $Å^{-1}$; (c) $Q_z$ = 0.089 $Å^{-1}$; (d) $Q_z$ = 0.110 $Å^{-1}$; (e) $Q_z$ = 0.132 $Å^{-1}$. (f) Optical image of the two island pattern. The image was trimmed to have the same scale as the reconstructed images. Scale bar on the top right shows 2 mm.

FIG. 5.5 (b) shows the reconstructed XRI image at $Q_z$ = 0.068 $Å^{-1}$, which is between the $Q_c$ of gold (0.078 $Å^{-1}$) and $Q_c$ of silicon (0.032 $Å^{-1}$). We can see a strong contrast between the gold islands and silicon substrate. At this $Q_z$, in the pattern region, X-rays are totally reflected by the gold and the reflectivity is unity. In the silicon part, X-rays are weakly reflected ($Q_c$ of Si is 0.032 $Å^{-1}$). The two gold islands show the same contrast, as X-rays do not penetrate the gold island film at this $Q_z$. Imaging at this wavevector transfer can be used to detect thin film's surface properties such as the shape and the roughness of the islands' surface.

FIG. 5.5 (c) shows the reconstructed XRI image at $Q_z$ = 0.088 $Å^{-1}$, which is beyond the $Q_c$ of gold (0.078 $Å^{-1}$). We can see a contrast between the middle and the top gold island, in addition to the contrast between the gold islands and silicon substrate. At this wavevector transfer, the image of the middle island is brighter than that of the top island, which means higher reflectivity from the middle island, as shown in FIG. 5.4 (b). In both islands, X-rays penetrate the gold films. The difference is that the reflectivity from the thick top island deviates more from unity than that of the thin middle island. Imaging at this wavevector transfer can be used to detect layer properties such as the shape and the thickness of the thin film. FIG. 5.5 (d) shows the reconstructed XRI image at $Q_z$ = 0.010 $Å^{-1}$, which is in the range of interference fringes region. At this wavevector transfer, the image of the top island is brighter than that of the middle island, which means higher reflectivity from the top island, which

feature also coincides with that shown in FIG. 5.4. The image contrast was reversed compared with the image at $Q_z$ = 0.088 Å$^{-1}$. In addition, the image is not uniform inside each island, because the local thicknesses of the island are also different, as shown in TABLE II. The islands have complex structures: the middle island is mainly composed of a ring structure, while there are shadows inside the ring. The top island consists of an outer shell and an inner uniform structure. FIG. 5.5 (e) shows the reconstructed XRI image at $Q_z$ = 0.013 Å$^{-1}$. The image contrast is reversed again compared with the image at $Q_z$ = 0.010 Å$^{-1}$. At this wavevector transfer, the image at the middle island position is brighter than that of the top island, which means higher reflectivity from the middle island. These features also accord with that shown in FIG. 5.4. At this $Q_z$, the substructures inside each island are different from the previous XRI image: the image of the middle island is now mainly composed of a uniform plateau and a dark ring. However, in case of the top island, only the ring structure is still being resolved. By combining imaging at different wavevector transfers in the interference fringes region, one can visualize not only obvious differences (ex. differences between the middle and the top island), but also very tiny structure differences in sub nm scale (ex. substructure of the film near the edge of each island). By analyzing the image, one can recognize how the two points differ. This technique has high sensitivity along the depth, typically ~Å, while higher $Q_z$ could further emphasize higher sensitivity.

### 5.3.3 Distinguishing different materials

As is commonly known, X-ray reflectivity is not an element selective technique. However, by introducing the in-plane spatial resolution, X-ray reflectivity imaging can provide selective ability when we carefully choose the wavevector transfer of interest. The sample used here is a commercial available patterned target: the repetition of the unit composed of gold, copper and chromium line patterns on a glass substrate, as shown in FIG. 5.7 (d). The sample size is 10 × 10 mm$^2$. The single line width for each material is 0.2 mm with a thickness of 1000 Å.

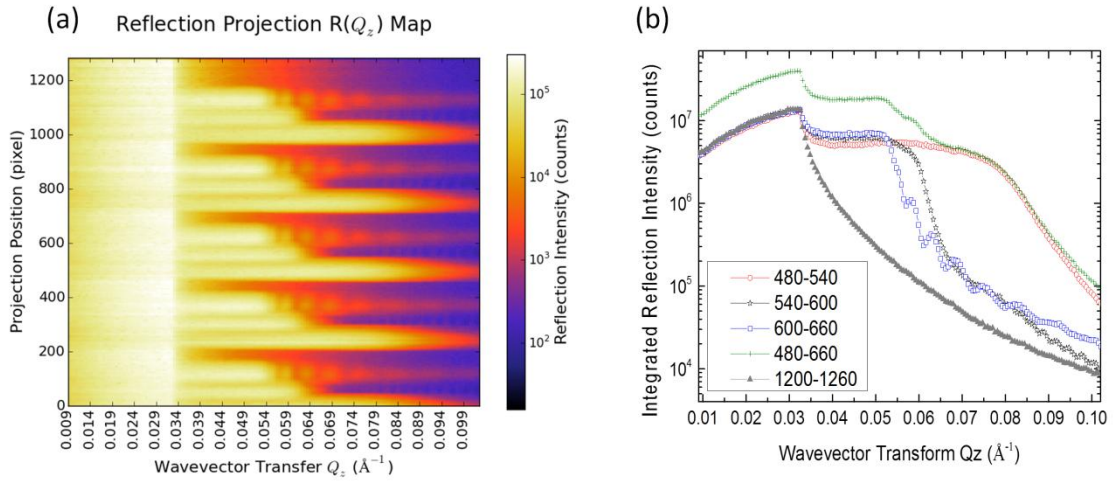


FIG. 5.6 X-ray reflection profiles of the pattern target of Gold, Copper, Chromium line patterns/glass. line width: 0.2 mm; film thickness: 1000 Å. (a) Local reflectivity profiles of the pattern sample measured at the SR facility as the reflection projection map of the wavevector transfer $Q_z$, The scanning step for the measurement is $\Delta Q_z$ = 0.0005 Å$^{-1}$, the data are plotted in logarithmic colorscale. The sample was positioned to ensure the line patterns parallel to the X-ray forward direction. (b)

Extracted X-ray reflectivity profiles integrated in the specific pixel range (see Left figure Y Axis): gold area [480 - 540] (circle), Copper part [540 - 600] (star), Chromium [600 - 660] (rectangle). Area includes all [480 - 660] (cross), and bare Si [1200 - 1260] (solid triangle).

We can also measure X-ray reflectivity projections of the target depending on wavevector transfers $Q_z$s. In order to obtain the reflectivity from different materials independently, the sample was aligned to make the line pattern parallel to the X-rays forward direction. The $Q_c$s of chromium, copper and gold are 0.053 $Å^{-1}$, 0.057 $Å^{-1}$ and 0.079 $Å^{-1}$ respectively, as shown in FIG. 5.6 (a). Such values are quite close to the standard values. FIG. 5.6 (b) shows extracted reflection intensity profiles integrated in the specific pixels range: gold area [480 - 540] (circle), copper part [540 - 600] (star), chromium [600 - 660] (rectangle), area that includes all [480 - 660] (cross), and bare $SiO_2$ [1200 - 1260] (solid triangle). Although the sample was aligned, it was still difficult to make the line pattern perfectly parallel to the beam. The reflectivity profiles are influenced by such a tilt [3 ° CCW direction, shown in the caption of FIG. 5.7 (d)]. This makes the reflectivity profile a mixture of neighboring areas. All materials: gold, copper and chromium reflectivity profiles possess a drop at $Q_z$ = 0.032 $Å^{-1}$, which is the $Q_c$ of the glass substrate. In the displayed $Q_z$ range, gold does not have the interference fringes part. Chromium shows interference fringes in the high $Q_z$ part, while copper's fringes are smeared because of the overlap with neighboring gold and chromium.

We chose three different $Q_z$s to selectively image different materials. 72 reflection projections (views) were measured to reconstruct the X-ray reflectivity image, which is enough to resolve the pattern (0.2 mm). The total measuring time for 1 image is 72 sec. FIG. 5.7 (a) - (c) are the reconstructed images from the experiment at different wavevector transfers $Q_z$s. The images were reconstructed utilizing the same convolution back-projection algorithm with the cutoff frequency 0.5.

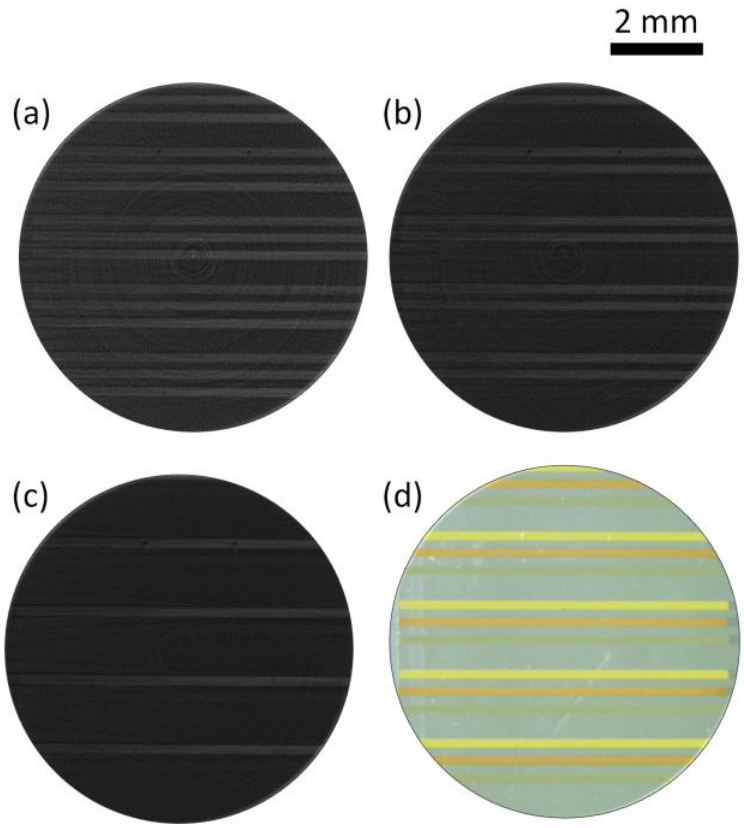


FIG. 5.7 Reconstructed X-ray reflectivity images of the commercial available sample of Gold, Copper, Chromium line patterns/glass at different wavevector transfers. Parameters for image reconstruction: 72 views, Cutoff frequency for Ram-Lak filter: 0.5. (a) $Q_z$ = 0.053 $Å^{-1}$; (b) $Q_z$ = 0.056 $Å^{-1}$; (c) $Q_z$ = 0.063 $Å^{-1}$. Three reconstructed images have been rotated 3 °CW for comparison. (d) Optical image of the sample. The image was trimmed to have the same scale as the reconstructed images. Scale bar on the top right shows 2 mm.

FIG. 5.7 (a) shows the reconstructed reflection image at $Q_z$ = 0.050 $Å^{-1}$, which is below the $Q_c$ of all materials but above the Qc of glass (0.032$Å^{-1}$). We can see a contrast of three line patterns on the black substrate. X-rays that reach the surface of each material are totally reflected by the surfaces, while those that reach the glass substrate strongly penetrate the bulk and are weakly reflected. Imaging at this wavevector transfer shows the pattern of all three materials.

FIG. 5.7 (b) shows the reconstructed XRI image at $Q_z$ = 0.056 $Å^{-1}$, which is below the $Q_c$ of gold and copper but above the $Q_c$ of chromium (0.053$Å^{-1}$). We can resolve the contrast of two line patterns on the black substrate, and the bottom line is not resolved. At this $Q_z$, X-rays that reach the surfaces of gold and copper are totally reflected, while those that reach the surface of chromium are weakly reflected and the reflectivity from the chromium surface is much less than unity. Imaging at this wavevector transfer shows the pattern of the two materials with higher electron densities.

FIG. 5.7 (c) shows the reconstructed XRI image at $Q_z$ = 0.060 $Å^{-1}$, which is below the $Q_c$ of gold but above the $Q_c$ of chromium (0.053$Å^{-1}$) and copper (0.057$Å^{-1}$). We can see a contrast of one line patterns on the black substrate, and the two bottom lines are not resolved. At this $Q_z$, only X-rays that reach the surface of gold are

strongly reflected. Imaging at this wavevector transfer shows only one material pattern, viz., only gold is selected in the image.

Three different materials were selected one by one using this imaging technique, as discussed in the paragraphs above. However, it is necessary to emphasize that this technique does not give spectroscopic element information like characteristic energies in X-ray fluorescence technique, but probes the electron densities of the sample. The critical wavevector transfer $Q_c$ is decided by Eq. (4): the $Q_c$ is proportional to the square root of density $\rho$, hence the sensitivity to density is mediocre. The three different materials have different electron densities, so the critical wavevector transfers $Q_c$s get different values. This imaging technique can selectively visualize different materials by taking advantage of the different total reflection plateau regions.

### 5.3.4 In-plane spatial resolution

In this experiment, the vertical angular divergence of the X-ray beam is nearly 0.02 mrad, and the distance between the sample and the detector is around 300 mm, so the in-plane spatial resolution of this technique is limited only by the pixel size of the CCD camera: 6.45 μm (6.45 μm > 0.02 × 300 μm). In practice, the optical lens for the scintillation layer may smear the image and the spatial resolution may also be affected by the imperfection of optics. The theoretical predicted value is around 15 μm. A 1951 US Air Force(USAF) resolution test target was used for directly checking the in-plane spatial resolution, and it includes a pattern of different sized horizontal and vertical Cr bars on a glass substrate. The resolution target was cut to an appropriate size to obtain the X-ray reflectivity images. FIG. 5.8 (c) shows the optical microscopy image of the resolution target.

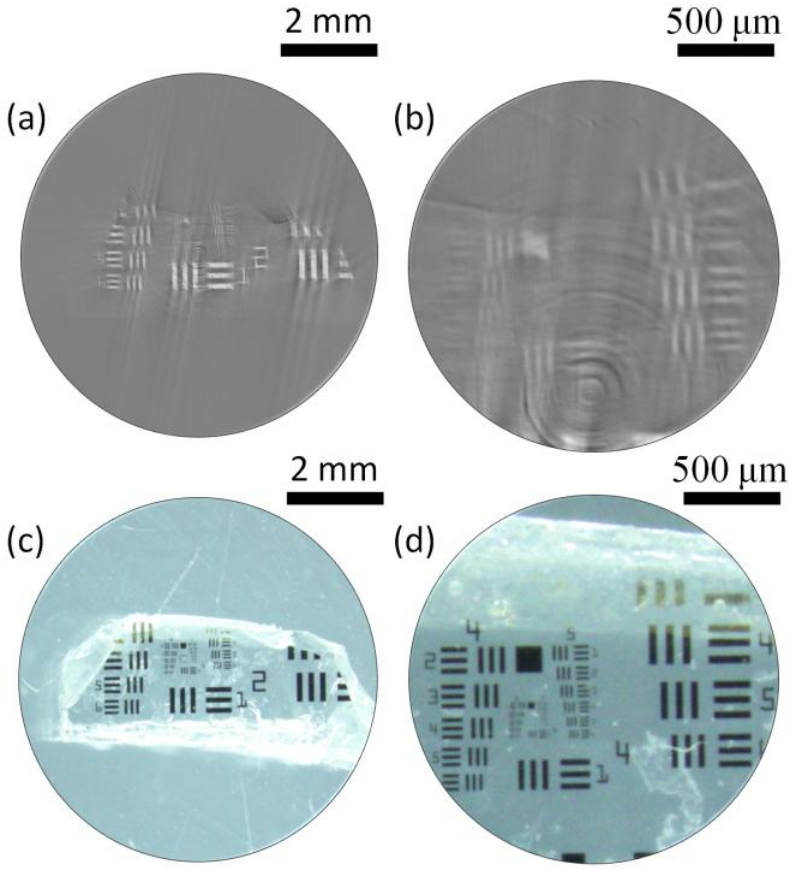


FIG. 5.8 Reconstructed X-ray reflectivity images and optical images of the USAF resolution target in two different magnifications. The resolution target was cut to an appropriate size suitable for the viewing area. (a) low magnification and (b) high magnification of the reconstructed image; (c) optical image and (d) enlarged image of the interested area corresponding to the same scale as (a) and (b). Scale bars are shown at the top right.

We chose $Q_z$ = 0.046 $Å^{-1}$ to enhance the contrast between chromium ($Q_c$ = 0.053 $Å^{-1}$) and the glass substrate ($Q_c$ = 0.032 $Å^{-1}$). 360 reflection projections (views) were measured to obtain the X-ray reflectivity image, in order to resolve the finer structure. The total measuring time was 360 sec. FIG. 5.8 (a) shows the reconstructed image from the experiment. We reconstructed the image utilizing the convolution back-projection algorithm with the cutoff frequency set at 0.5. FIG. 5.8 (b) shows the enlarged image to indicate the resolution, while FIG. 5.8 (d) is the optical microscopy image in the same magnification scale. The smallest width resolved is nearly 20 μm, which is not far from the prediction. In the previous section, it is demonstrated that the sensitivity of XRI in the depth direction is ~1 Å. In summary, the spatial resolutions along three orthogonal directions at the present stage are established: 20 μm × 20 μm × 0.1 nm.

In the experiment, the specification of $Q_z$ is decided by the incident grazing angle, as shown in Eq. (1). According to the geometry of this experiment, the beam width is 0.05 mm (H) × 8 mm (V). In order to get a square viewing area (footprint in the reflectivity measurement) of 8 mm(H) × 8 mm(V), the incident angle can be calculated from Eq. (5) and should be 6.25 mrad, which corresponds to the $Q_z$ of 0.100 $Å^{-1}$. At different $Q_z$s, the width of incident beam (the width of entrance slit) should have been adjusted to the proper value as suggested by the Eq. (5). In our experiment, we applied a slit with a fixed width of 0.05 mm, and it may have caused some distortions in the image. However, these distortions still do not influence the previous data analysis

(large pattern), although it may smear the images and influence the spatial resolution. When applied to more difficult cases such as the observation of structures approaching the spatial resolution limit or the detection of extremely tiny differences, such distortions or smearing effects should be taken into account. In such cases, introducing a width adjustable slit is helpful.

## 5.4 Conclusion

In this work, we have successfully visualized the buried layers and interfaces in ultrathin films by a novel X-ray reflectivity imaging technique using synchrotron radiation. By collecting a series of reflection projection intensity profiles during an in-plane rotational scan of the sample, under grazing-incidence reflection geometry, we can obtain the X-ray reflectivity image by employing mathematical image reconstruction. By tuning the grazing angle, we successfully obtained different image contrasts, which indicate that different in-depth structures were enhanced. The different X-ray reflectivities at local in-plane areas of thin films at a specific wavevector transfer show the different in-plane structures of the sample. By comparing different images at different incident angles, we not only visualized buried interfaces, but also obtained nice contrasts in tiny thickness differences (in the order of ~ Å) and selectively visualized different materials with different densities. We also confirmed that the in-plane spatial resolution is better than 20 μm. This technique provides high in-depth sensitivity (~ Å) with quite good spatial resolution (20 μm).

# Chapter 6 Interface sensitive imaging by image-reconstruction aided X-ray reflectivity technique

The previous chapter demonstrates how we have succeeded in realizing X-ray reflectivity imaging (XRI) of heterogeneous ultrathin films at specific wavevector transfers by applying a wide parallel beam and an area detector. In this chapter, we describe that by combining in-plane angle scan and grazing incident angle scan, it is possible to reconstruct a series of interface sensitive X-ray reflectivity images at different grazing incident angles (proportional to wavevector transfers). The physical meaning of a reconstructed X-ray reflectivity image at a specific wavevector transfer is the 2D reflectivity distribution of the sample, in that manner it is possible to retrieve the micro X-ray reflectivity (where the pixel size is in micro-scale) profiles at different local positions of the sample.

## 6.1 Introduction

we have successfully developed a complementary novel X-ray reflectivity imaging (XRI) technique employing a wide monochromatic synchrotron beam [84] and an area detectors. This technique developed by us[79,80,85] is based on X-ray reflectivity and an image reconstruction scheme that is mathematically similar to computerized tomography [70–72]. The physical meaning of a reconstructed X-ray reflectivity image at a specific wavevector transfer is the 2D reflectivity distribution of the sample. Here, we extend the technique to obtain more information of the samples by collecting a series of X-ray reflectivity images at different wavevector transfers. In this work, we are able to retrieve many X-ray reflectivity profiles at micro-scale areas covering full sample (size: 8 mm × 8 mm).

## 6.2 Experimental

### 6.2.1 Model Sample preparation

We prepared a heterogeneous patterned ultrathin film sample (schematically shown in the center of FIG. 6.1, where yellow corresponds to gold patterns, black refers to nickel patterns, transparent flat cylinder stands for the uniform titanium cover layer). The thin film composed of heterogeneous layers was fabricated by the Eiko sputtering coater on a pre-cleaned silicon substrate (20 mm × 15 mm × 2 mm). The thickness of the silicon substrate was chosen to maintain the mirror surface flat enough. Under the top uniform Ti layer the heterogeneous layer is composed of two groups of patterns: (1) left top gold polygon and right bottom rectangle with different thicknesses; (2) left bottom nickel thick rectangle, right top triangle and right center thin bar (see

the schematic of the sample in FIG. 6.1). The model sample was constructed as follows: (1) the silicon substrate was set into the sputter chamber and covered by a specific mask made of kapton film. The mask was pre-cut with the designed different patterns. The chamber of the sputtering machine was pre-vacuumed to < 0.1 Pa and filled with Argon gas. High voltage was applied to ionize Ar atom between the gold target (original material) and substrate and a gold film was then deposited onto the sample substrate. The sputtering condition was as follows, Ar pressure: 2 Pa, ion current: 50 (a.u.), sputtering time: 30s. The mask was then replaced by that of a different pattern. The chamber of the sputter was again pre-vacuumed to < 0.1 Pa and filled with Argon gas. High voltage was then applied and the sputtering condition for the second gold pattern was as follows, Ar pressure: 2 Pa, ion current: 50 (a.u.), sputtering time: 60s. (2) The gold foil target was replaced by a nickel foil target. The nickel patterns (triangle, rectangle and bar) were then deposited one by one. The sputtering condition for nickel patterns were as follows, Ar pressure: 2 Pa, ion current: 260 (a.u.), sputtering time was chosen as 10s, 20s and 30s to prepare different nickel patterns with different thicknesses. (3) The nickel foil target was then displaced by a titanium foil target. Then mask with a circle hole (8 mm dia.) is set to limit the depositing area. The chamber of the sputter was again pre-vacuumed to < 0.1 Pa and filled with Argon gas. The sputtering condition for the titanium layer was as follows, Ar pressure: 2.0 Pa, ion current: 200 (a. u.), sputtering time: 80s. The titanium layer covers the gold and nickel patterns uniformly and makes them buried separated layers.

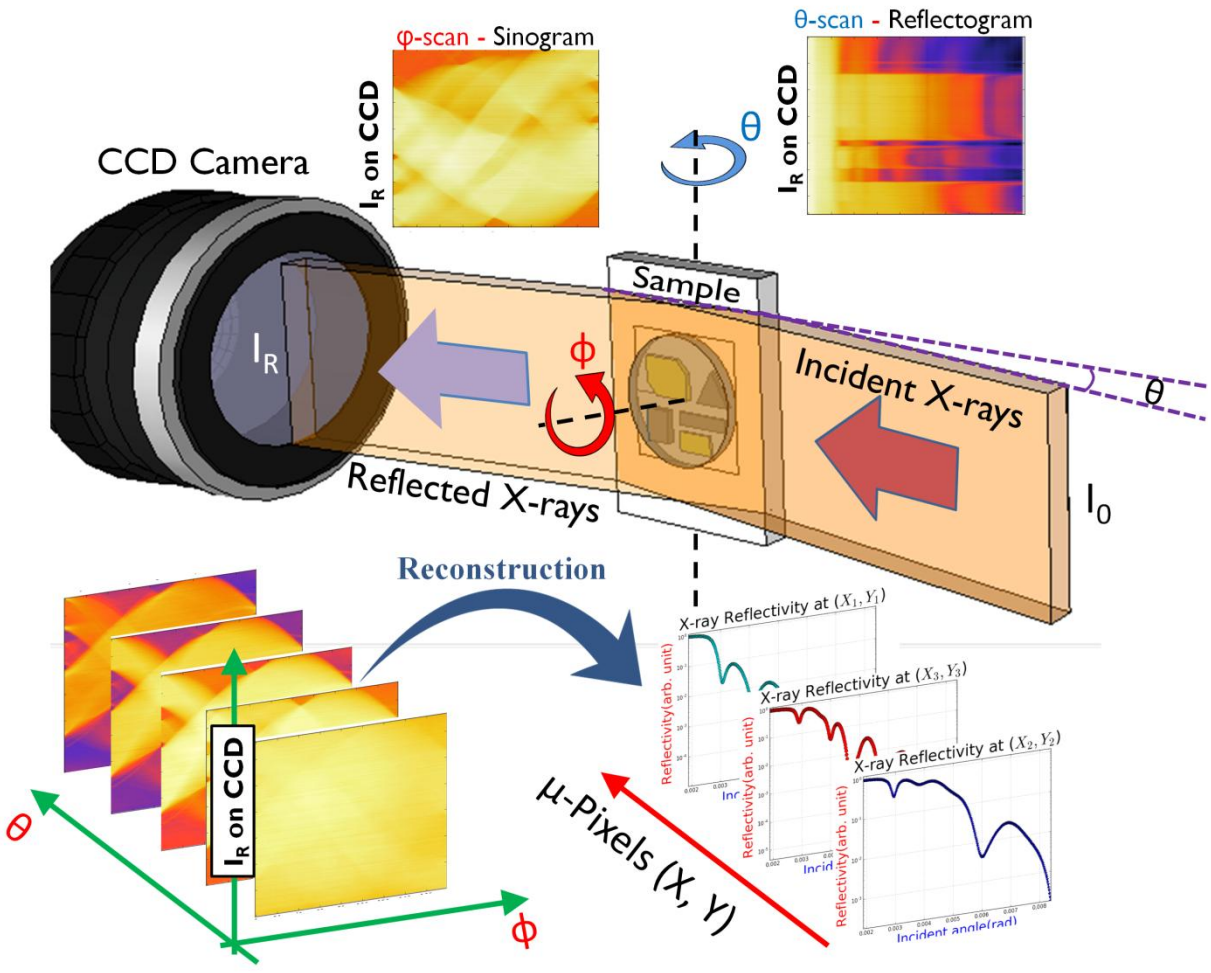


FIG. 6.1 Conceptual schematic of the interface sensitive imaging technique by image-reconstruction aided X-ray reflectivity. A monochromatic wide X-ray beam irradiates the full sample at a grazing incident angle θ, and the reflected X-ray beam at

the equivalent exit angle θ is recorded as an approximate 1D profile by an X-ray CCD camera. The sample is rotated in-plane and many such 1D profiles are recorded at different in-plane angles φ (usually plotted as a sinogram). By combining grazing incident angle θ scan, many sinograms at different θ are collected as the raw data. The full μ-X-ray reflectivity profiles at different sample positions are derived from the collection of the whole data set by reconstruction process.

### 6.2.2 X-ray reflectivity imaging technique

The experiments of interface sensitive imaging by X-ray reflectivity were carried out on the beamline 14-B, Photon Factory, Tsukuba, Japan. The new imaging approach is an extension of the recently developed X-ray reflectivity imaging (XRI) technique [84]. By combining the XRI and ordinary X-ray reflectivity (XR) θ/2θ scan, we are able to realize interface sensitive imaging by X-ray reflectivity, as schematically shown in FIG. 6.1 (In-plane angle φ = 0 °, grazing incident angle θ = 2 mrad are drawn in the figure). The experimental set-up is as the same as that of X-ray reflectivity imaging. The synchrotron radiation from the vertical wiggler was monochromatized to 16keV [around the peak position of the spectrum[82]] by a fixed-exit double crystal Si(111) monochromator. Monochromatic X-rays were collimated by several slits to form a parallel beam (vertical angular divergence: 0.02mrad), while the beam size was 0.10 (H) × 8 mm (V) at sample position. The parallel beam illuminated around 10 mm [H, footprint length of X-rays is always long enough to cover the silicon substrate size (10mm)] × 8 mm [V] sample surface at grazing incidence geometry. The sample stage is based on a high precision θ/2θ goniometer with the accuracy of 0.001 °. A rotational motor is vertically attached to an L-shape stand fixed on the goniometer to realize in-plane φ rotation. The Sample was vertically mounted by a sample holder that employs a small pump to attach the substrate from the backside. The sample holder was equipped with two manually tilting stages to adjust the sample surface to be perpendicular to the in-plane rotational axis. The reflected X-rays were recorded by a CCD camera (pixel size: 6.45μm) as a 1D projection image. By the in-plane angle φ-scan, the sample was rotated in-plane at specific interval angle (Δφ = 2 °, N = 90 projections) until 180 degree and reflectivity projections were collected at each interval angle, plotted as a sinogram. By the grazing incident angle θ-scan, sample was tilted at specific interval grazing angle (Δθ = 0.004 °) and reflectivity is collected as a function of θ and plotted as a reflectogram. By combining φ-scan (XRI) and θ-scan (XR), we are able to reconstruct the micro X-ray reflectivity (μXR) profiles at different local positions of the sample, where the spatial resolution of the μXR is decided by the pixel size of the reconstructed XRI image.

## 6.3 Results and discussions

### 6.3.1 Origin data reduction

The origin data were reflection projections recorded by the CCD camera and stored in many TIF (Tagged Image Format) images with 16 bits dynamic range. Note that the X-rays' footprints on the CCD camera are not perfectly 1D projections but narrow rectangles as the incident X-rays horizontally have the width of 100 μm. In order to efficiently handle many TIF images, we use many Python open-source libraries designed for scientific computing such as numpy, matplotlib, and Tkinter. For the data reduction and processing, we prepared Python codes to read each TIF file, specify the area of interests, and integrate the reflection rectangles into 1D projection with the batch mode compatibility. CCD dark counts background is subtracted and then the data are normalized to counting rate by considering different measuring time in low and high grazing incident angles range.

### 6.3.2 The data collection

In the measurement, we collected 1D X-ray reflection projections systematically in different grazing angles (θ-scan) and in-plane angles (φ-scan). The reduced informative data collection is composed of many 1D X-ray reflection projections as a function of grazing angle θ and in-plane angle φ. They are either be grouped as (a) different sinograms at different grazing angles, or (b) different reflectograms at different in-plane angles. The former group method is equivalent to many XRI measurements at different grazing angles, while the later group fashion corresponds to many XR measurements at different in-plane angles. In order to retrieve μXR at all the in-plane locations of the sample, both of φ-scan and θ-scan are required, and we can choose the order depending on the experimental convenience.

#### 6.3.2.1 Sinograms at different wavevector transfers $Q_z$s

Following the fashion of XRI, the experimental data were stored as a collection of sinograms at different grazing incident angles θ, namely at corresponding wavevector transfers $Q_z$s. θ is the grazing incident angle and relates to the wavevector transfer $Q_z$ (normalized by X-rays wavelength λ) by [44]

$$Q_z = \frac{4\pi \sin\theta}{\lambda} \tag{1}$$

FIG. 6.2 gives some selected X-ray reflectivity sinograms of the sample plotted as a function of in-plane angles φ at specific incident angles with wavevector transfers of (a) $Q_z$ = 0.0377 Å$^{-1}$, (b) $Q_z$ = 0.0422 Å$^{-1}$, (c) $Q_z$ = 0.0502 Å$^{-1}$, (d) $Q_z$ = 0.0651 Å$^{-1}$, (e) $Q_z$ = 0.0845 Å$^{-1}$, (f) $Q_z$ = 0.1369 Å$^{-1}$. Mathematically, the reflection projection is the integral reflection intensity profile along the X-ray forward direction according to the Radon transform[70]

$$p_\varphi(r) = \int_{-\infty}^{\infty} f(r\cos\varphi - z\sin\varphi, r\sin\varphi + z\cos\varphi)dz \tag{2}$$

where φ is the in-plane angle, r is the projection positions (experimental pixel number on the CCD), **z** is the X-rays forward direction, f(x, y) is the 2D reflectivity image, and $p_\varphi(r)$ is the 1D reflection projection profile at in-plane angle φ. In each panels of FIG. 6.2, the features (if any) experience half of rotation, thus the integrated reflectivity projection forms a half period of sine wave. The X-ray's penetration depth in the sample is tuned by the wavevector transfer $Q_z$. At small wavevector transfer $Q_z$ = 0.0377 Å$^{-1}$, the X-rays are totally reflected by the Ti surface, thus displaying a uniform sinogram. In panel (b) where $Q_z$ = 0.0422 Å$^{-1}$, a washy feature is immersed in the uniform background. Howbeit when $Q_z$ = 0. 0502 Å$^{-1}$, a strong contrast is achieved and the pattern below the Ti is shown as the $Q_z$ is beyond the critical wavevector transfer $Q_c$(Ti) of Ti. In panel (d) where $Q_z$ = 0. 0651 Å$^{-1}$, there begins to exist variation between different features as nickel's critical wavevector transfer $Q_c$(Ni) is smaller than this $Q_z$. In panel (e) $Q_z$ = 0.0845 Å$^{-1}$ and (f) $Q_z$ = 0.1369 Å$^{-1}$, both of the wavevector transfers are larger than $Q_c$(Au), the change of contrast is demonstrated and detailed characteristics inside the gold film is responsible of such sinograms.

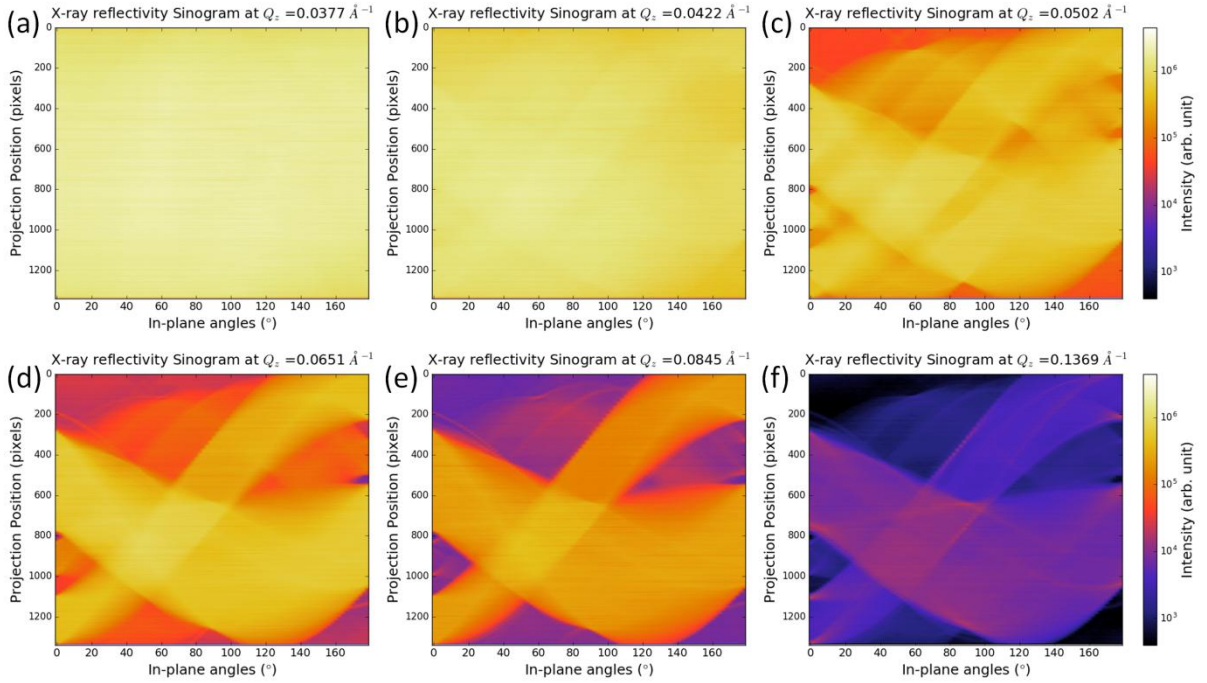


FIG. 6.2 Selected X-ray reflectivity sinograms of the sample plotted as a function of in-plane angles φ at specific incident angle with wavevector transfer of (a) $Q_z$ = 0.0377 $Å^{-1}$, (b) $Q_z$ = 0.0422 $Å^{-1}$, (c) $Q_z$ = 0.0502 $Å^{-1}$, (d) $Q_z$ = 0.0651 $Å^{-1}$, (e) $Q_z$ = 0.0845 $Å^{-1}$, (f) $Q_z$ = 0.1369 $Å^{-1}$, where the data are plotted on a same range logarithmic colorscale. The scanning step for the measurement is Δφ = 2 °.

### 6.3.2.2 Reflectograms at different in-plane angles φs

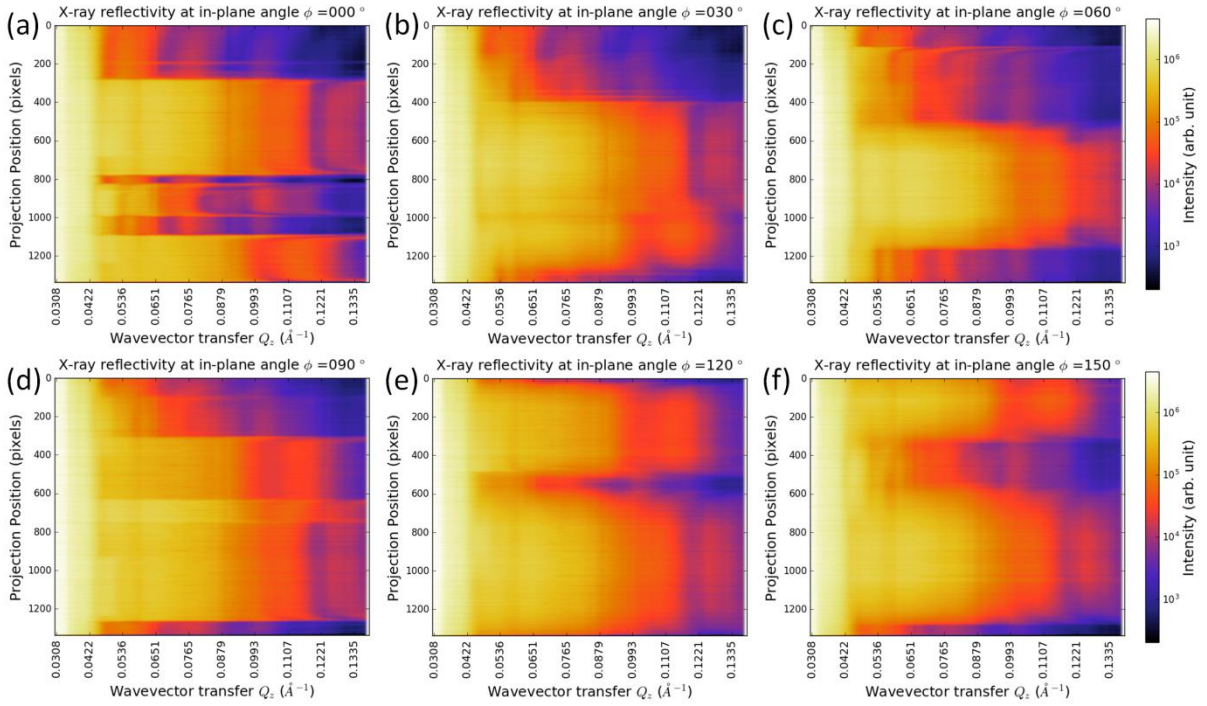


FIG. 6.3 Selected X-ray reflectograms of the sample plotted as a function of wavevector transfers $Q_z$ at specific in-plane angle (a) φ = 0 °, (b) φ = 30 °, (c) φ = 60 °, (d) φ = 90 °, (e) φ = 120 °, (f) φ = 150 °, where the data are plotted on a same range logarithmic colorscale. The scanning step for the measurement is $\Delta Q_z$ = 0.00114 $Å^{-1}$.

The collection of the data can be categorized in another scheme: many reflectograms at different in-plan angles, where the reflectogram is composed of reflectivity projections at a series of wavevector transfers collected by grazing incident angle θ-scan. The selected 6 reflectograms at characteristic in-plane angles are shown in FIG. 6.3. In all panels, a sharp intensity drop at $Q_z$ = 0.42 $Å^{-1}$ is observed, which corresponds to the critical wavevector transfer $Q_c$ of titanium. Another two intensity drops are around $Q_z$ = 0.50 $Å^{-1}$ and $Q_z$ = 0.80 $Å^{-1}$, corresponding to the $Q_c$ of nickel and gold, respectively. More careful inspection of critical wavevector transfer $Q_c$s from the experimental data and comparison with theoretical values will be discussed in Section 3.4. A reflectogram is physically a collection of 1D reflectivity projections integrating along a specific perspective observation direction at a series of wavevector transfers. The model sample is designed in that way we can confirm the reliability of the data. In panel (a) at φ = 0 °: (1) in the position range of [0 - 280], where the sample is composed of a uniform Ti layer, four equal period interference fringes are observed (the same feature is throughout the whole reflectogram, and also shown in the range of [1000 - 1080]), also corresponding to a uniform Ti film; (2) in the position range of [280 - 780] and [1080 - 1338], there are higher reflectivity intensities in the whole $Q_z$ range than those of other regions. Such areas are mixture of gold and nickel patterns, and the contribution of reflectivity from nickel is weak beyond the nickel $Q_z$ = 0.50 $Å^{-1}$. The contribution of nickel patterns are still visible in the position range of [500 - 780] and [1240 - 1338] where there exist low intensities range corresponding to lack of nickel pattern in the range of $Q_z$ = 0.42 - 0.50 $Å^{-1}$ (see the schematic of sample in FIG. 6.1 for comparison). In that range X-rays are not only totally reflected by gold, but also completely reflected by nickel. The reflectivity profiles of the gold films in the position range of [280 - 780] and [1080 - 1338] are also different, implying that the different structures of the gold or nickel patterns. (3) in the position range of [820 - 1000], the reflectivity profile is not the same for the local position of the pattern, which implies the different thicknesses at local positions of the same pattern; (4) At the position around [200], there exists a brighter reflectivity profile, which corresponds to the leakage of gold from the mask in the sputtering process (as will be shown in Section 3.3).

In panel (b) φ = 30 °and panel (c) φ = 60 °, the characteristics of reflectograms show differences with that of panel (a): (1) the reflectivity profiles of the gold patterns are closer and the patterns overlap with each other and form a higher intensity region in the position range of [520 - 1180] at φ = 60 °. In the position range of [120 - 260], there appears a new pattern that corresponds to the nickel triangle on the sample. When the sample rotates to the in-plane angle φ = 90 °in panel (d), we start to see the separation and the other different length side of the gold polygon and rectangle. In panel (e) and (f), the reflectograms give a further different descriptions of the sample at specific perspective in-plane angles.

### 6.3.3 Reconstructed X-ray reflectivity images

As it is possible to achieve single reflectivity points in a XRI image[84,85] from a sinogram at specific wavevector transfer $Q_z$, and we have collected many sinograms at different $Q_z$s, the micro X-ray reflectivity profiles at every pixel are easy to be plotted by extracting reflectivity values at a series of XRI images. In order to achieve a quantitative X-ray reflectivity profiles, stable image reconstruction scheme shall be adopted. In this chapter, we firstly transfer the Radon transfers to an algebraic linear system [70–72], and then apply the Pseudo Inverse algorithm [86–88] [In specific, Truncated Singular Value Decomposition method] to reconstruct many XRI

images. Considering it is a direct discrete method and a convenient accession to employ different regularization methods to different sample cases, we selected the algebraic fashion to quantitatively reconstruct the XRI images.

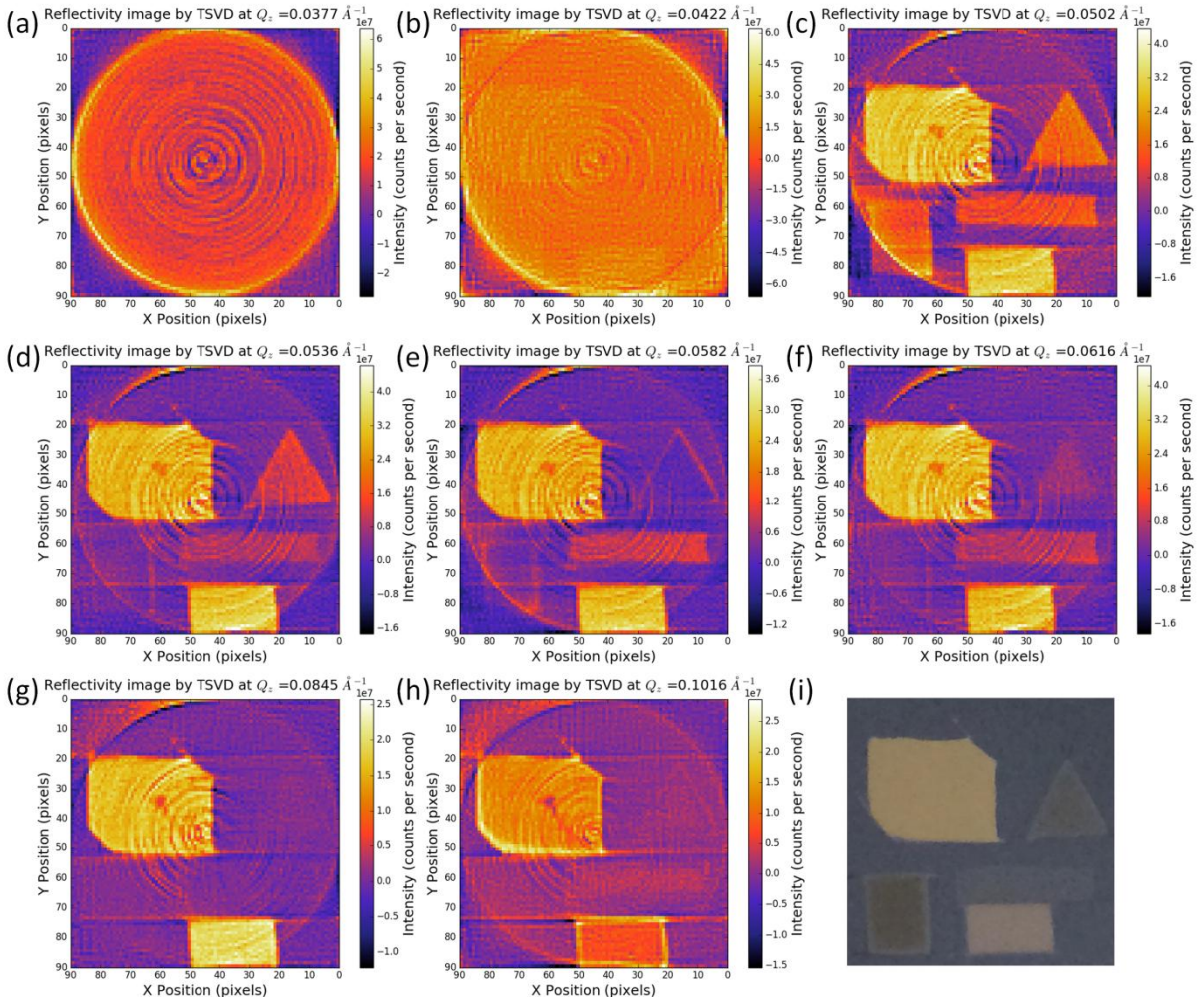


FIG. 6.4 Selected reconstructed X-ray reflectivity images of the sample at specific incident angle with wavevector transfer of (a) $Q_z$ = 0.0377 $Å^{-1}$, (b) $Q_z$ = 0.0422 $Å^{-1}$, (c) $Q_z$ = 0.0502 $Å^{-1}$, (d) $Q_z$ = 0.0536 $Å^{-1}$, (e) $Q_z$ = 0.0582 $Å^{-1}$, (f) $Q_z$ = 0.0616 $Å^{-1}$, (g) $Q_z$ = 0.0845 $Å^{-1}$, (h) $Q_z$ = 0.0616 $Å^{-1}$, where the data are plotted on logarithmic colorscales. Number of projections for image reconstruction: 90 views. (i) An Optical image of the patterned sample before coating with the titanium uniform layer. The image was trimmed to have the same scale as the reconstructed images.

In the experiment, we measured reflection projections at 90 in-plane angles per wavevector transfer. In order to avoid the rank deficient problem of the algebraic system [73], the 1338 pixels (measured 1D reflection projection length: 6.45μm × 1338 = 8.6mm) are equally binned into 90 pixels (pixel length: 96μm, 96μm × 90 = 8.6 mm), yet the spatial resolution suffers from the binning processing. In order to achieve higher resolution μXR, a smaller in-plane angle step scan is necessary. FIG. 6.4 presents several selected reconstructed X-ray reflectivity images of the sample at wavevector transfers of (a) $Q_z$ = 0.0377 $Å^{-1}$, (b) $Q_z$ = 0.0422 $Å^{-1}$, (c) $Q_z$ = 0.0502 $Å^{-1}$, (d) $Q_z$ = 0.0536 $Å^{-1}$, (e) $Q_z$ = 0.0582 $Å^{-1}$, (f) $Q_z$ = 0.0616 $Å^{-1}$, (g) $Q_z$ = 0.0845 $Å^{-1}$, (h) $Q_z$ = 0.0616 $Å^{-1}$, respectively. Panel (i) is the optical image of the sample taken before covering the uniform Ti layer. Panel (a) exhibits a uniform image, irrespective of the existence of ring artifacts. The bland image just matches the uniform surface of the Ti layer, whose $Q_c$ = 0.42 $Å^{-1}$ > 0.0377 $Å^{-1}$. In panel (a), X-rays only penetrates into the surface layer as an evanescent wave with a typical penetration depth of ~10 Å, where the image can be made to

be surface sensitive. The image at panel (b) is picked up at around the $Q_c$ of Ti, where a weak contrast of the pattern is observed. As the $Q_z$ = 0.0422 $Å^{-1}$ is below the $Q_c$ of the nickel layer and far below that of the gold layer. At the $Q_z$ the specific fraction of X-rays (depends on the $Q_z$ and surface properties of the surface layer) penetrating through the Ti layer are totally reflected by the patterns but lost in the pattern-free region. The difference of the penetrating fraction of X-rays leads to the light contrast. In panel (c) the fraction of X-rays passing through the surface layer increases and we obtain a higher contrast of the patterns. In addition, as the $Q_z$ is close to the $Q_c$ of nickel, the gold patterns produce higher reflectivity than nickel patterns (of which reflectivity intensities start to decrease around the critical wavevector transfer), thus giving a contrast between two different materials patterns. At pixel [55, 15] in panel (c), the tail structure from the main pattern is detected, and this features can be also found in the optical image of panel (i) and is coherent with the feature of FIG. 6.3(a). Around pixel [60, 35] in the center of gold polygon, we can see a dark spot, and such feature is not found in panel (a), which means the feature (whether it is a hole or inclusion) is below the surface of the uniform titanium layer and above the gold polygon. It is necessary to mention that the effective image is within the inscribed circle, and some parts of the patterns in the bottom are out of the effective viewing area. In panel (d) the reflectivity intensities from the nickel patterns decrease as the $Q_z$ is larger than the $Q_c$ of nickel, while the gold patterns keep the same visibility. The visibility of the left bottom nickel rectangle is poorest, which obviously suggests that its X-ray reflectivity profile is different from that of other nickel patterns, demonstrating the layer properties (thickness or roughness) of the left bottom nickel rectangle is different with other nickel patterns. In panel (e) at $Q_z$ = 0.0582 $Å^{-1}$, we see a right top hollow nickel triangle and a left bottom hollow rectangle contrast, originating from the difference of layer thicknesses between the edge and the center of the patterns. The thickness difference is verified by panel (f) at $Q_z$ = 0.0616 $Å^{-1}$, where the right top nickel triangle pattern gives a contrast of solid triangle. In addition, the left bottom nickel rectangle shows a washy shadow and middle long nickel bar still keeps a high visibility, apparently indicating the three nickel layers are distinctive in properties. In addition, there still exists the dark spot around pixel [60, 35] with similar morphology. In panel (g) at $Q_z$ = 0.0845 $Å^{-1}$, which is larger than the $Q_c$ of gold, the reflectivity intensities from gold patterns also begin to decline. Withal, the shape of the dark spot around pixel [60, 35] changes a little bit, revealing the hetero-structure owns a depth profile inside the gold layer. At $Q_z$ = 0.0616 $Å^{-1}$ in panel (h), we mainly see a hollow left top gold polygon and a hollow right bottom gold rectangle contrast, suggesting thin similar edge structure as that of nickel patterns. Interestingly, there appears a long tail extended from the dark spot around pixel [60, 35], which confirms that the defect stretches into the gold layer and has a depth dependence.

### 6.3.4 Micro X-ray reflectivity profiles

Since we collected a series of X-ray reflectivity images sampled equally in a range of wavevector transfers, we were able to reconstruct the X-ray reflectivity profile at every micro sized pixel. Such X-ray reflectivity profile of one micro sized pixel is called micro X-ray reflectivity (μXR). In this proof-of-principle experiment, imaging of the 90 × 90 pixels (size ~96μm) produces 8100 μXR profiles. Compared with nano / micro beam [74,89,90] scan methods, although the μXR approach requires some numerical analysis, it owns several merits. (1) It possesses no perspective effect based on an image reconstruction scheme; In the scan method, the size of nano / micro beam shall be asymmetric in turns of grazing incidence geometry, as in the X-ray forward direction s = 1

μm beam will have a footprint length of L = s/sinθ = 100 μm at θ = 10 mrad. (2) The spatial resolution of the μXR is limited by the pixel size of the area detector, while the limitation is possible to go beyond by for instance employing a post-magnifier. (3) Other than employing sophisticated optics to focus X-rays, the μXR applies the parallel Synchrotron beam, and this is especially important to X-ray reflectivity that demands high angular resolution. Howbeit we need to take good care as the μXR picks up the X-ray reflectivity profiles by many in-plane φ-scan and image reconstruction scheme. In order to check the measurement's merits of figure, we sum up the pixels counts along the 1D projection of the reflectogram (as selectively shown in FIG. 6.3) at each in-plane angle. The integrated profile corresponds to X-ray reflectivity of the heterogeneous film measured by ordinary X-ray reflectometor. FIG. 6.5(a) shows the integrated X-ray reflectivity profiles plotted as in-plane angles. It indicates that the integrated X-ray reflectivity profile does not change when the sample is rotated in-plane. This simple fact implies at least two important conclusions: (1) the footprint of X-rays on the sample remained on the same area during the in-plane angle scan; (2) the incident angle did not change during the in-plane angle scan, which kept the reproducibility of the wavevector transfer range. Furthermore, FIG. 6.5(b) presents a comparison of the integrated X-ray reflectivity profile from the raw reflectogram data (blue open circle) and that from the pixel sum of μXR profiles. As shown, the two X-ray reflectivity profiles are almost the same, indicating the image reconstruction does not possess any preference to low or high reflectivity intensities.

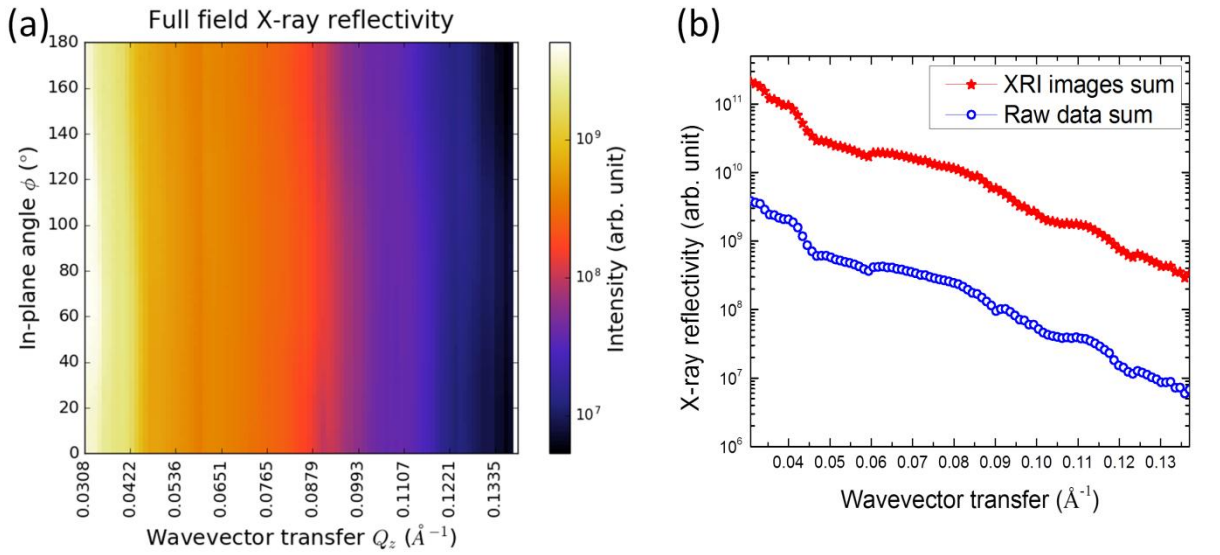


FIG. 6.5 The X-ray reflectivity profile of the whole sample. (a) Integrated X-ray reflectivity of the heterogeneous thin film sample at different in-plane angles, showing the figure of merit of the measurement. (b) The integrated X-ray reflectivity profiles of the sample derived from the raw data (blue open circle) and reconstructed X-ray reflectivity images (red solid star).

### 6.3.4.1 Micro X-ray reflectivity profiles of arrays of pixels

Selected micro X-ray reflectivity mapping of an array of pixels are shown in FIG. 6.6 at (a) Y = 30, (b) Y = 35, (c) Y = 62, (d) X = 10, (e) X = 35, (f) X = 72 (where here the upper case indicates the title at each panel) at the range wavevector transfers of from $Q_z$ = 0.0308 ~ 0.1369 $Å^{-1}$, where the coordinates correspond to that of FIG. 6.4. The reconstructed micro X-ray reflectivity mappings are pure X-ray reflectivity profiles from an array of micro pixels (μ-pixlels), which are different from the reflectograms of FIG. 6.3 (a collection of data, integrated X-ray reflectograms along a perspective direction according to Radon transform). The top panels show μXR profiles from the array of pixels along the X direction. In panel (a) at Y =30, we see two sets of μXR

profiles as the Y=30 line slices through the top gold polygon [x = 42 – 86, where here the lower case indicates the y-axis at each panel] and nickel triangle [x = 10 - 20]. By looking at the μXR profiles with a reasonable spatial resolution, it is possible to conduct micro area analysis of the ultrathin film sample. The center of the gold polygon [x = 44 - 84] is quite uniform and at different locations along the Y = 30 line similar μXR profiles are observed, regardless of intensity fluctuations from the ring artifacts. There exists a length (~2 pixels, 192 μm) with smaller thickness at both edges. The nickel triangle with the intercept length of 1.05 mm (x = 10 – 21, 11 pixels) is not as uniform as the gold polygon and shows asymmetric thickness gradient at the edges (see the μXR profiles near x = 10 and x = 20). In panel (b) at Y =35, the slice passes through the same patterns. The differences compared with panel (a) are: (1) a longer intercept (1.63 mm) across the nickel triangle [x = 7 – 24, 17 pixels], which is not surprising for a triangle shape; (2) a low intensities profile shown at x = 60 in the μXR set of the gold polygon, which is the same as the discussion in Section 3.3. Moreover, we see the defect become wider at high $Q_z$, which means that the defect possesses a volume into the deeper location. Since the technique is an interface sensitive imaging approach by collecting many XRI images at a series of wavevector transfers, it is a powerful method to find tiny hetero-structures (usually such tiny differences control the useful function) in the quite large sample. At Y = 62 in panel (c), the line goes through the left bottom nickel rectangle and right bottom nickel bar, whereby we see two sets of μXR profiles. The two μXR profiles possess different appearance from the right top triangle [shown in panel (b)]. Detailed comparison will be discussed in Section 3.4.2.

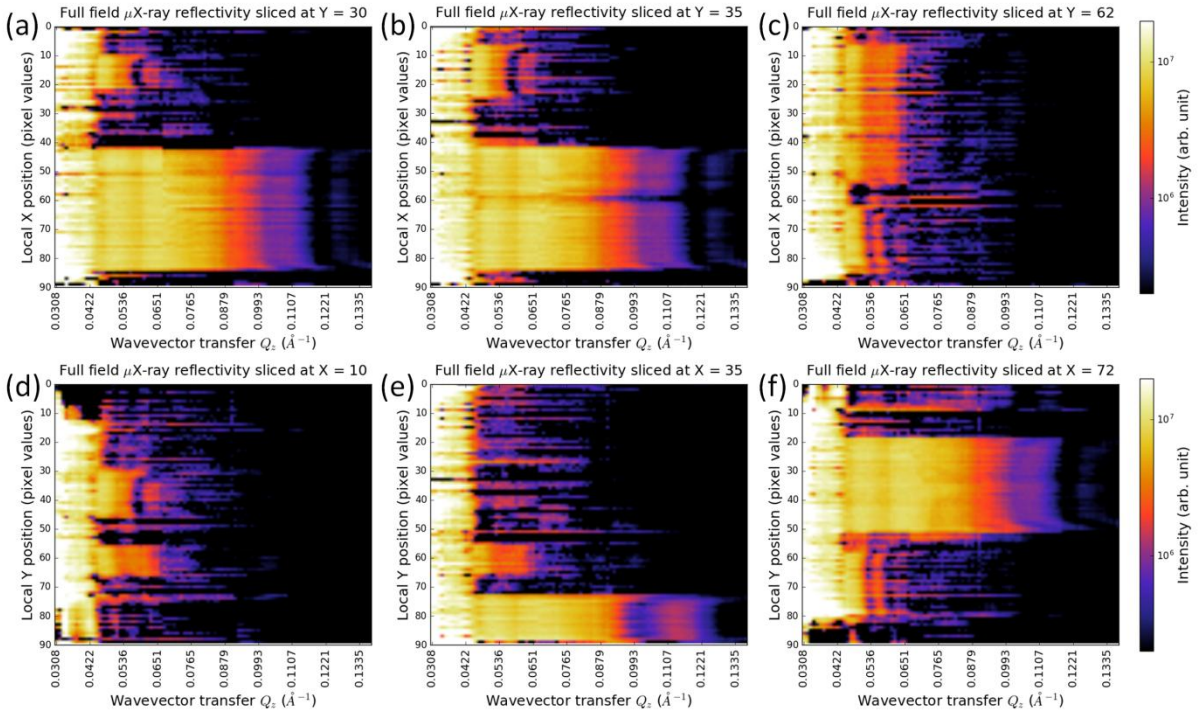


FIG. 6.6 Selected micro X-ray reflectivity mapping of an array of pixels at (a) Y = 30, (b) Y = 35, (c) Y = 62, (d) X = 10, (e) X = 35, (f) X = 72 corresponding to the coordinates in FIG. 6.4 extracted from reconstructed X-ray reflectivity images at the whole range of wavevector transfers from $Q_z$ = 0.0308 ~ 0.1369 $Å^{-1}$. The micro X-ray reflectivity intensity profiles are from the local (X, Y) positions indicated by the title and y-axis of each panel, which are different from the integrated reflectograms shown in FIG. 6.3. The y-axis indicates the other μ pixel coordinate (the main μ pixel coordinate is shown in the title of each panel), while x-axis corresponds to the wavevector transfer. The reflectivity intensities are plotted on a logarithmic scale.

The bottom panels give μXR profiles from the array of pixels along the Y direction. The panel (d) X = 10 shows the local μXR profiles of the nickel right top triangle and center bar. The μXR profiles from the same pattern are similar at different perspectives, which is coherent with the design of the sample. At $Q_z$ = 0.050 ~ 0.065 $Å^{-1}$, the two nickel patterns obviously possess two different μXR profiles, which confirms that they are different in structures. In panel (e) at X = 35, the μXR profiles of the right bottom gold rectangle are shown at y = 74 – 88. Compared with that of the left top gold polygon, they hold different appearance for $Q_z > 0.080$ $Å^{-1}$. Furthermore, inside the gold rectangle pattern, there exists heterogeneous structure at the edges (y = 74 – 77, 3 pixels). In panel (f) at X = 72, we again checks the μXR profiles of the left top gold polygon. Along the Y direction (X = 72), the polygon shows obviously asymmetric thickness gradient at the edges (compare the μXR profiles at near y = 20 and y = 50). Thanks to many local μXR profiles obtained from the measurement, more detailed analysis of the heterogeneous thin film sample can be discussed.

### 6.3.4.2 Micro X-ray reflectivity from single pixels

FIG. 6.7 shows several selected micro X-ray reflectivity profiles from single pixels: (a) pixel [40,10] (red open uptriangle), (b) pixel [70,30] (orange open circle), (c) pixel [42,82] (olive open rectangle), (d) pixel [70,65] (blue open diamond), pixel [15,40] (violet open downtriangle), pixel [35,62] (dark yellow open star), where the coordinates are coherent with that of FIG. 6.4. In (a) – (c) panel, simulations calculated by Parratt's formulism[6] are displayed (black line) as guides. The parameters used to calculate the profiles are summarized in Table 1. The pixel [40, 10] in panel (a) of FIG. 6.7 corresponds to a gold or nickel pattern-free area, in such a manner that there is only a uniform layer of titanium at this pixel. The μXR profile confirms this point by displaying a sharply drop at $Q_z$ = 0.042 $Å^{-1}$ and the equal period interference fringes (interference of X-rays reflected by surface and Ti/Si interface). The one-layer-model simulation matches the profile well, irrespective a few outliers. In panel (b) at the pixel [70, 30], the μXR possesses a intensity drop around $Q_z$ = 0.042 $Å^{-1}$ (the $Q_c$ of surface titanium) and shallow oscillations (due to the interference of X-rays reflected by surface and Ti/Au interface) below $Q_z$ = 0.08 $Å^{-1}$ (the $Q_c$ of surface gold). Beyond $Q_z$ = 0.08 $Å^{-1}$, the μXR profile drops sharply (X-rays penetrate into the gold layer) and experiences different oscillations (due to the interference of X-rays reflected by surface, Ti/Au interface and Au/Si interface) corresponds to the thickness of the gold layer. In the simulation, the same properties cover titanium layer is assumed, and it is found that the thickness of the gold layer is around 240 Å, as shown in Table 1. The μXR other gold pattern, at the pixel [42, 82] in panel (c), however, shows different oscillation period beyond $Q_z$ = 0.08 $Å^{-1}$. Only one tact fringe is observed, which means this gold layer is thinner than that of the panel (b). The simulation shows the thickness of the gold layer of the pixel [42, 82] is around 112 Å, which value is reasonable considering the difference of deposition time. Panel (d) gives the μXR profiles of nickel patterns. Here no simulation has been conducted as the nickel layer is not a single layer (even it is the case for uniform one time deposition). In order to discuss the in-depth structure of multilayer structure, a longer $Q_z$ range and better $\Delta Q_z$ resolution may be necessary. Howbeit it is possible to conduct such experiments for more complicated samples. In panel (d), μXR profiles of three pixels stand for three different nickel patterns. All the three μXR profiles possess a small intensity drop at near $Q_z$ = 0.042 $Å^{-1}$, which corresponds to the $Q_c$ of Titanium. The second large drop in μXR profiles correspond to the $Q_c$ of nickel is 0.049 $Å^{-1}$, and it turns out that the nickel patterns have a low density 5.86 $g/cm^3$. Moreover, the number of interference fringes of the three μXR

profiles in the limited $Q_z$ range are different: $N_{[70,65]} > N_{[15,40]} > N_{[35,62]}$, indicating the thicknesses difference: $d_{[70,65]} > d_{[15,40]} > d_{[35,62]}$, which is consistent with different deposition time. As above, we have successfully retrieved micro X-ray reflectivity profiles from the in-plane angle scan and grazing incident angle scan measurements.

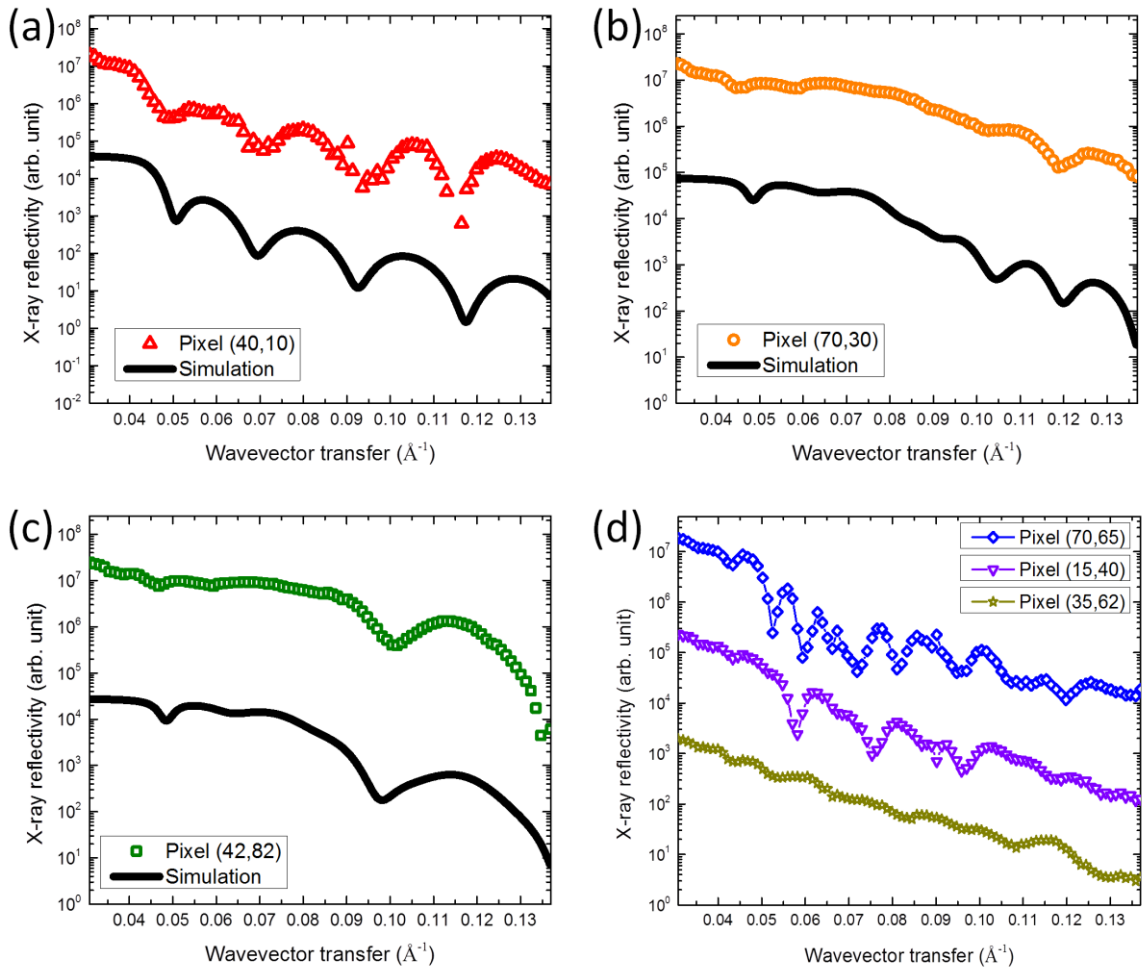


FIG. 6.7 Selected micro X-ray reflectivity profiles extracted from reconstructed X-ray reflectivity images at the whole range of wavevector transfers from $Q_z = 0.0308 \sim 0.1369$ Å$^{-1}$ at local positions of (a) pixel [40,10] (red open uptriangle), (b) pixel [70,30] (orange open circle), (c) pixel [42,82] (olive open rectangle), (d) pixel [70,65] (blue open diamond), pixel [15,40] (violet open downtriangle), pixel [35,62] (dark yellow open star), where pixel numbers correspond to that in FIG. 6.4. In (a) – (c) panel, simulations calculated by Parratt's formulism are displayed (black line) as guides.

TABLE 6.1The parameters used for the Parratt's formulism to conduct the X-ray reflectivity profiles simulations in FIG. 6.7. The inter-diffusion parameter is set as 16 Å for the Ti surface, 10 Å for the Ti / gold interface and 6 Å for the gold / Si interface.

| Local Points[#] | Layers Model[†] | Measured $Q_c$ ($Å^{-1}$) [1] | Layer density ($g/cm^3$) [‡] | Thickness (Å) |
|---|---|---|---|---|
| [40,10] | **Ti**/Si | 0.04108 | 4.25 | 230 |
| [70,30] | Ti/**Au**/Si | 0.07936 | 19.32 | 230/280 |
| [42,82] | Ti/**Au**/Si | 0.07936 | 19.32 | 230/112 |

[#]Local points correspond the positions specified by the pixel values in FIG. 6.4.

[†] The Silicon substrate has an infinite thickness.

[‡]The Layer density ρ is calculated from the $Q_c$ and they are that of the layer indicated in bold.

### 6.3.5 Quantitative analysis and outlook

In this study, we have firstly demonstrated that interface sensitive imaging by image-reconstruction aided X-ray reflectivity technique. By combining the in-plane angle scan and grazing incident angle scan, we are able to extract micro X-ray reflectivity profiles from full areas of a large sample. In this proof-of-principle experiment, the analysis is still semi-quantitative. Possible future improvements include: (1) More careful calibrations of X-ray intensities and detector. In order to extract X-ray reflectivity profiles to analyze film's properties like roughness, it is necessary to employ normalization to the X-ray reflectivity projections. Moreover, we need to consider sensitivities of the area detector; as usual X-ray reflectivity covers quite a long dynamic range. (2) Robust image reconstruction scheme. We need some suitable image reconstruction approaches to obtain reliable numbers in the inverse processes. Sometimes regularizations are necessary. We then need to know the resolution matrix to tell us how the results are smeared out.

## 6.4 Conclusion

In conclusion, interface sensitive imaging of a heterogeneous thin film sample by image-reconstruction aided X-ray reflectivity technique has been successfully demonstrated employing a wide monochromatic synchrotron beam. By applying an area detector, combining in-plane angle scan and grazing incident angle scan, we are able to reconstruct a series of X-ray reflectivity images at different grazing incident angles (proportional to wavevector transfers). The physical meaning of a reconstructed X-ray reflectivity image at specific wavevector transfers is the 2D reflectivity distribution of the sample. Thereby we are able to pick up the micro X-ray reflectivity (where the pixel size is in micro-scale) profiles at different local positions of the sample, where the spatial resolution of the μXR is decided by the pixel size of the reconstructed XRI images.

# Chapter 7 X-ray reflectivity imager with 15 W power X-ray source

X-ray reflectivity imaging is a promising approach that can be implemented not only in synchrotron facilities, but also as a routine technique in the laboratory. In the X-ray laboratory in NIMS, we have invented the original complementary X-ray reflectivity imager suitable for routine imaging of surfaces and buried interfaces, which make it accessible to more researchers. In parallel geometry as the case in the previous chapters, the spatial resolution either suffers from the beam angular divergence and pixel detector element size. The angular divergence of ordinary rotating anode source in laboratory is quite large (~20 mrad) and the typical detector pixel size is 50 μm. Other than the implement of the similar parallel beam geometry, the use of the beam divergence and the application of the magnification in fan beam geometry could avoid such limitations. The present chapter gives the instrumental details of the compact X-ray reflectivity imager employing laboratory micro-focus X-ray source. Though the power of X-ray source is only 15W, it works well. The calibration of the system has been discussed, because it is particularly important for the present grazing incidence geometry. We also give a visualization example of the buried interface, physical meaning of the reconstructed image and discussions about possibilities for improvement.

## 7.1 Introduction

Advanced X-ray imaging techniques are promising and appealing, because X-rays are capable of penetrating through mater non-destructively, have a short wavelength and hence the produce images with high spatial resolution[44]. Many progresses have been achieved in the past decades, but there are few X-ray imaging techniques developed for surfaces and interfaces. Invented surfaces and interfaces imaging techniques by different groups include X-ray reflection phase-contrast full field microscopy[9], Fourier transform holography in reflection geometry[10], a coherent diffraction imaging technique near total external reflection[11], and a ptychographic X-ray imaging technique on crystal truncation rod[78]. Although these techniques are competitive for specific applications, many of them require high brilliance sources like synchrotron facilities and sophisticated optics, while others rely on coherent X-rays or special samples.

We invented a complementary laboratory X-ray reflectivity imager suitable for routine imaging of surfaces and interfaces in layered heterogeneous thin films with a large scale viewing area [10 mm × 10 mm] and tunable imaging depth fashion. The technique is based on X-ray reflectivity (XR). XR is extremely sensitive to slight structural changes along the depth of thin films in the order of sub-nanometers or sub-angstroms, but the limitation is it always averaging over the thin films and doesn't own an in-plane spatial resolution[74]. However, the heterogeneous structures are usually more practical and scientifically important. We give XR imaging capability by introducing the image reconstruction scheme instead of scanning the micro-beam. X-ray reflectivity imaging technique in parallel beam geometry has been performed and demonstrated by employing laboratory rotating anode X-ray source[79,80] and synchrotron radiation[91]. The spatial resolution either suffers from the beam divergence (laboratory case, achieving an in-plane spatial resolution of

1.6 mm) and pixel detector element size (synchrotron radiation case, with the detector pixel size of 6.45 μm). The use of the beam divergence and the employment of the magnification feature could avoid such limitations. In this chapter, we describe how we successfully invented the X-ray reflectivity imager with portable low power micro focus X-ray source.

## 7.2 Instrumentation

Our X-ray reflectivity imager (XRI) is based on recording many 1D X-ray reflectivity projections and 2D image reconstruction. The image reconstruction process shares some similarities with computed tomography techniques[70], because X-ray reflectivity imaging technique employs the same mathematical image reconstruction algorithms. However, XRI gives more information than mere cross-sectional density image, which is usually given by ordinary transmission X-ray computer tomography. In the case of multilayered thin films, X-ray electric field inside a sample is modulated by its layered structure and also by the glancing angle (more exactly, wavevector transfer $Q_z$)[92]. This suggests the new type of imaging technique is able to give contrasts sensitive to a specific layer and/or interface. Compared with computed tomography technique, X-ray reflectivity imager: (1) does not need very high energy X-rays or high transmission; (2) does not experience the beam hardening problem as incident X-rays impinges on every local position of the sample simultaneously; (3) has high sensitivity along the depth direction of sample because the image contrast originates from interferences[4] of X-rays reflected by each interfaces of the sample.

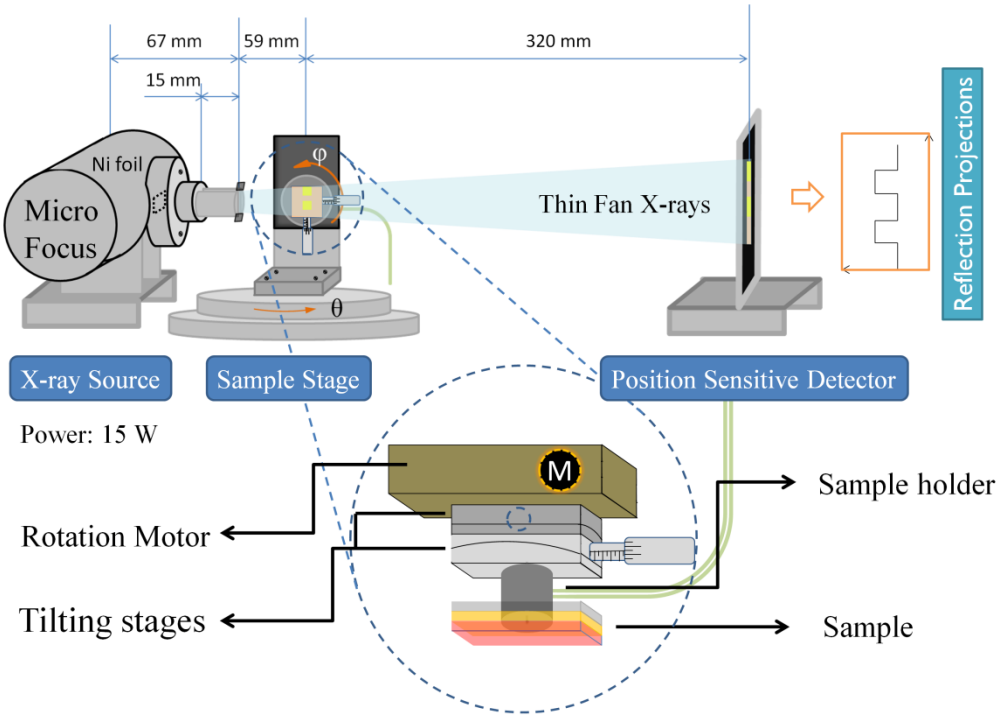


FIG. 7.1 Side view of the prototype X-ray reflectivity imager. The Oxford Instrument micro focus X-ray source with focusing size of 35 μm (nominal) is modified to fulfill the aim: A 20 μm thick Ni foil was pasted on the upstream side of the top plate window of the source; on the downstream side two flat tungsten alloy plates were attached vertically (50 μm gap) to the top plate by Araldite adhesive; on the top of tungsten plates two pieces of lead plate (1 mm thick) were put to cut vertical X-rays. X-rays from the top plate form a monochromatic thin fan beam. Inset is the enlarged image of the sample stage in the top view: Rotation motor realizes the in-plane φ motion of the sample; manually tilting stages help to adjust the sample to be perpendicular to the in-plane rotational axis. Samples are mounted vertically by a sample holder that uses a small pump. The sample stage is based on a precise Rigaku Diffractometer which could precisely change the grazing incident angle. Detector system is the Fuji Film imaging plate assembled on a linear motor.

The side view sketch of the prototype X-ray reflectivity imager is shown in FIG. 7.1. In order to collect enough reflectivity projections to reconstruct images, we design a system with three main components: a point X-ray source, a special sample stage and a position sensitive detector. An air-cooled sealed-type copper anode X-ray tube (Oxford Instruments, XTG5011, Apogee, max. power 50kV-1mA, nominal focus size 35 μm) is fixed on a linear positioning stage (manual) whose position could be adjusted along the direction orthogonal to the beam. To obtain only copper Kα X-rays without the use of crystal monochromator, the X-ray tube operates at quite low tube voltage, typically 15kV. Setting tube voltage at 15kV aims at efficiently suppressing the contribution of high energy bremsstrahlung. The top plate of the X-ray source is equipped with one filter and two collimating optics. The Cu Kβ filter (20 μm thick Ni foil) is pasted on the backside of the top plate. The absorption edge of Ni is 8.33 keV, which is slightly smaller than the energy of the other main peak of copper characteristic X-rays Cu Kβ = 8.90 keV and larger than that of the main peak of copper characteristic X-rays Cu Kα = 8.05 keV, so the Ni foil filter effectively absorbs the Cu Kβ but keeps the Cu Kα. The intensity ratio of Cu Kα / Cu Kβ X-rays after Ni filtering could be estimated by the formula:

$$\frac{I_{K\alpha}}{I_{K\beta}} = \frac{I_{K\alpha 0}\exp(-\mu_{K\alpha}\rho d)}{I_{K\beta 0}\exp(-\mu_{K\beta}\rho d)} \approx \frac{I_{K\alpha 0}}{I_{K\beta 0}}\exp\left[-(45.7-275)\times 8.908\times 0.002\right] = \frac{I_{K\alpha 0}}{I_{K\beta 0}}\times 59.5 \approx 7.5\times 59.5 = 450$$

in case of 20 μm Ni foil, where $I_{K\alpha 0}$ and $I_{K\beta 0}$ are the X-rays intensity of Cu Kα and Kβ before filtering, $I_{K\alpha}$ and $I_{K\beta}$ are those after filtering, $\mu_{K\alpha}$ and $\mu_{K\beta}$ are the mass absorption coefficients, ρ is the mass density, and d is the thickness of the Ni foil. In addition, the tube voltage is set as 15kV and tube current is 1mA. The intensity of the bremsstrahlung are proportional to the tube voltage to the 2nd power: $I_{cont.} \propto iZV^2$, while the intensity of characteristic X-rays are proportional to the tube voltage to the 1.5th power: $I_{K-line} \propto i(V - V_k)^{1.5}$. In the formulas i is the tube current, V is the tube voltage. $V_k$ is the K excitation voltage, Z is the atomic number. The low power efficiently decreases the high energy bremsstrahlung background and keeps higher fraction of characteristic X-rays, although we may sacrifice some flux. By the careful design, we have monochromatic X-rays emitted from the top plate window, as shown in FIG. 7.2. On the front side of the top plate two flat polished tungsten alloy plates (15 mm long) are attached vertically (50 μm gap) to the top plate by Araldite adhesive; on the opposite side of tungsten plates two pieces of lead plates (1 mm thick) are set to cut vertical X-rays. Open gap of the two lead plates, which determines fan beam's divergent angle, is adjusted simultaneously with glancing angle θ in order to achieve a square viewing area on the sample position. Heavy metals were chosen to effectively shape the beam and introduce no another fluorescent X-rays to the power spectrum. The outgoing X-ray beam from the collimating optics pertains to a fan shape from the side view, while keeps a parallel shape from the top view with some angular divergence. Solid angle of X-rays is confined by the narrow pathway and thereby X-rays from the top plate form a monochromatic thin fan beam.

A sample stage was designed to fulfill grazing incidence adjustments and in-plane rotation scans. Inset of FIG. 7.1 is the enlarged image of the sample stage in the top view. The sample stage is based on a Rigaku θ/2θ diffractometer which could precisely change the glancing angle of X-rays on a sample surface, with the accuracy of 0.001 degree. A rotational motor is vertically attached to an L-shape stand fixed on the goniometer to realize in-plane φ rotation. Samples are vertically mounted by a sample holder that employs a small pump to attach the substrate from the backside. In order to ensure the same grazing angle during in-plane motions, the sample holder is equipped with two manually tilting stages to adjust the sample surface to be perpendicular to the in-plane rotational axis.

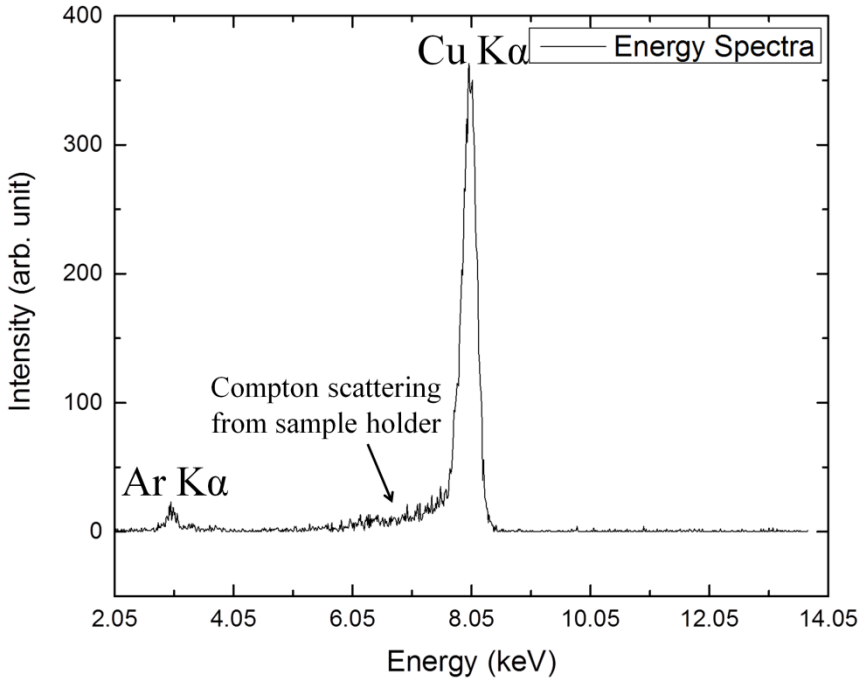


FIG. 7.2 The energy spectrum of primary X-rays beam, indirectly measured by air scattering near the sample holder by the Ourstech SDD detector operating at -10 ℃ and digitized by the multi channel analyzer MCA7600. The main peak corresponds to the Cu Kα line.

We utilize a Fuji Film imaging plate as the position sensitive detector. The imaging plate is put inside a special case with a carbon window assembled on the linear motor to realize automatical data acquisition. The reflectivity projections are very thin and recorded in a row on the imaging plate. Thereafter the imaging plate are scanned by a Fuji Film BAS-1800 system with the pixel size of 50 μm and reflectivity projections are digitized, integrated along the short direction (The projection is not perfectly 1D as I. incident X-rays has the width of 50 μm; II. X-ray beam disperses as propagating forward) and stored in a set for further data processing. The data scanned by the BAS-1800 scanner are stored originally in the logarithmic scale with 16 bits (0 ~ 65535), which is defined as quantum level (QL). The quantity that is proportional to the true X-rays intensity is called photo stimulated luminescence (PSL). PSL is related to QL as follows:

$$PSL = \left(\frac{P_{size}}{100}\right)^2 \times \frac{4000}{S} \times 10^{L\times\left(\frac{QL}{2^B}-\frac{1}{2}\right)}$$

where $P_{size}$ is the pixel size (50 μm), S is the sensitivity of the imaging plate (4000), L is the latitude (5.0, means with a dynamic range of $10^5$, which could include whole range of a routine X-ray reflectivity profile), B is the gradation speed and the number of bits used to store each pixel (B = 16). During the experiment, a sample is rotated at a specific in-plane interval angle Δφ, while the imaging plate on the linear motor moves one step per in-plane rotation interval and a sequence of reflectivity projections are recorded on the imaging plate with incremental distances. In addition, following every measurement of the reflectivity projection, the X-rays source is powered off and waits a period of time as the same as the measuring time to cool down, thus good stability of X-rays intensity is maintained during the whole measurements. The physical meaning of the projection is the integral reflectivity along the X-rays forward direction corresponding to a specific in-plane rotation angle φ = n × Δφ (n is an integer). Since the fan beam geometry is applied, the

1D reflectivity projection is magnified and the in-plane spatial resolution is only limited by the source size, which is ideally 35 μm; the magnification degree is:

$$M = \frac{SD}{SS} = \frac{446}{126} = 3.54$$

where SS is the source to sample distance, and SD is the source to detector distance. Table I shows the summary of the instrumental specifications of fan beam geometry X-ray reflectivity imager compared with parallel beam geometry X-ray reflectivity imaging technique. Because the X-ray reflectivity imager operates well at very low power without circulating water cooling system, and the setup can be highly compact, it is possible to employ this equipment in 'mobile use' such as on-site check.

TABLE 7.1 Summary of the instrumental specifications of fan beam geometry X-ray reflectivity imager compared with parallel beam geometry X-ray reflectivity imaging technique[79,80].

| | Fan beam geometry | Parallel beam geometry |
|---|---|---|
| X-rays Generator | Micro-focus tube | Rotating anode tube |
| Source size | 35 μm (nominal) | 50 μm × 10 mm (at 6 deg) |
| Tube voltage | 15kV | 20kV |
| Tube current | 1mA | 10mA |
| Cooling | Air | Circulating water |
| Monochromator | 20 μm Ni Filter | Multilayer |
| Collimator | 50 μm (H) × 10 mm (V) | 50 μm (H) × 9.5 mm (V) |
| Beam divergence (V) | --- | 20 mrad |
| Magnification | 3.54 | --- |
| Spatial resolution | < 0.18mm | ~1.6 mm |
| Resolution limit | Source size | Beam divergence |

## 7.3 Calibration

X-rays reflectivity imager is a grazing incidence X-ray scattering imaging technique that is very sensitive to X-ray wavelength [λ, in the unit of Å] and incident angle [θ, in the unit of mrad] in the form of the wavevector transfer $Q_z$:

$$Q_Z = \frac{4\pi \sin\theta}{\lambda}$$

X-ray energy is monochromated by the proper instrumentation, we need to achieve a good calibration for incident angle θ. Alignment could be divided into two parts: (1) beam geometry calibration, which is only applied when the instrument is firstly constructed or influenced by strong vibrations; (2) sample alignment, which is needed to be done each time following sample exchange.

### 7.3.1 Beam geometry calibration

There are several calibrations should be considered before mounting a sample, and such calibrations are highly crucial to the reconstructed image quality. The X-ray beam is collimated and calibrated horizontally and vertically. (1) Horizontally, the beam is adjusted to hit the rotational center of the Rigaku θ/2θ diffractometer (goniometer). The goniometer center is found by rotating the goniometer 180 ° and is pointed out by a fixed position sharp pinhead. We then move the X-ray beam (horizontally narrow) to hit the pinhead position. By using the imaging plate, we could easily check the positions of the pinhead and the X-ray beam. Thereby we move the X-ray source along the orthogonal direction of X-rays propagating plane to ensure the beam's impinging upon the pinhead, where the shadow of the pointer appear on the beam footprint shown on the imaging plate. (2) The linear stage of the imaging plate is adjusted to make the X-ray beam impinge on the near edge part of the imaging plate, from which we could move the imaging plate to the other direction and make full use of the imaging plate to record as many reflectivity projections as possible. (3) Vertically, the beam (fan shape) is adjusted to the height where the center line of the fan is coincident with the rotational center of the in-plane motor. In order to find the in-plane rotational center, we use another pin that attaches to the sample holder. X-ray shadow of the pin is recorded by the imaging plate at φ = 0 ° and 180 °; thereafter, the rotational center is calculated and compared with the center line of the fan beam. The difference that the in-plane rotational center from the center line is calculated back at the vertical lead slit position. The height of vertical lead slit is then shifted to compensate the difference. The procedure is repeated several times until the in-plane rotational center corresponds to the center line of the fan beam. (4) The height of the imaging plate is also adjusted to the optics center so the reflectivity projections appear at the vertical center of the imaging plate.

### 7.3.2 Sample alignment

The sample alignment includes the translational alignment to ensure a proper viewing area on the sample (footprint of X-rays shall exactly cover the sample surface) and the grazing angle calibration (related to both the viewing area and the penetration depth). These two alignments are usually done simultaneously.

As the position sensitive detector is used, we could monitor the X-ray direct beam and the reflected beam on our detector. (1) Before mounting the sample, the X-rays direct beam is recorded [line (limited width) shape] and the width of the direct beam is recorded. (2) A sample is introduced to the X-ray path where half of the direct beam is blocked by the sample. There are two cases in this procedure: (a) an X-ray reflection also appears on the imaging plate, which indicates the grazing angle is positive. Then we move the goniometer to decrease grazing angle until we cannot see the reflection that coincides with the direct beam. (b) There is no X-ray reflection on the imaging plate, which indicates the grazing angle is negative. Then we move the goniometer to increase grazing angle until we can see the reflection, then decrease the grazing angle to make the reflection coincides with the direct beam. The grazing angle is approximately 0 at this position, and the sample translational position is adjusted to cut half of the direct beam. We repeat the calibration two or three times until both of the criteria are fulfilled: (1) the sample blocked half of the direct beam; (2) the grazing angle is 0, which can be confirmed by varying the incident angle(we move the goniometer a small angle '+δ' and '-δ', if the beam is widest at the original point and the widths at '+δ' and '-δ' are the same, we can say the original position is **'0'**).

## 7.4 Image reconstruction

The Fuji Film BAS-1800 system is used to read imaging plate and the PSL values for each pixel are digitized and stored in a defined IMG file. We prepared Python codes to read the IMG file and integrate the projected reflectivity rectangles into line profiles with the batch mode compatibility. In order to efficiently handle the imaging plate data, we use many open-source Python libraries designed for scientific computing such as numpy, matplotlib and Tkinter.

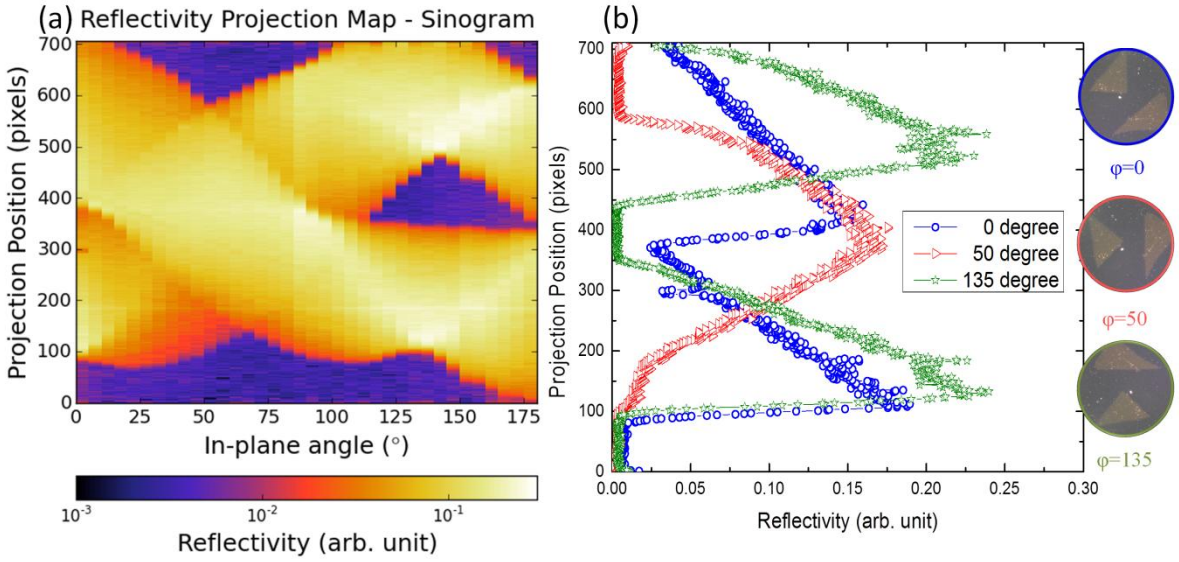


FIG. 7.3 Typical X-ray reflectivity projections data of the Carbon /Gold pattern (two triangles) /Si sample: two triangles' thickness are 1000 Å, while the thickness of uniform carbon layer is around 680 Å. Left: sinogram of the sample plotted as the in-plane angle φ at specific incident angle θ = 6 mrad, with wavevector transfer $Q_z$ = 0.049 $Å^{-1}$, the data are plotted in logarithmic colorscale. Right: extracted reflectivity projection line profiles at different specific in-plane rotational angle: blue open circle, φ = 0 °; red open right-triangle, φ = 50 °; olive open star, φ = 135 °. Insets show the sample in-plane positions to help with understand of the geometry, where X-rays are assumed from the left hand side.

The purpose of the reconstruction process is to reconstruct a map of X-ray reflectivity throughout the sample in-plane at a specific wave vector transfer $Q_z$. To reconstruct the image, the preprocessed projections are stored in a matrix known as a sinogram, as shown in FIG. 7.3(a). We prepared the image reconstruction software based on Convolution Back-projection[70] (CBP) algorithm using Object-Parscal coded Graphical User Interface (GUI): we firstly convolve the projection data with h(r) [the inverse Fourier transform of the ramp filter H(r)] in space domain:

$$g_\varphi(r) = h(r) * P_\varphi(r)$$

where $g_\varphi(r)$ is the convolved projection at a specific in-plane angle φ, $P_\varphi(r)$ is the measured projection at specific in-plane angle φ and h(r) is the filter function in space domain[it is mathematically the same as to multiply the projections with the ramp filter function H(r) in frequency domain]:

$$h(r) = \frac{f_c}{\pi r}\sin(2\pi r f_c) - \frac{f_c}{(\pi r)^2}\sin^2(\pi r f_c)$$

where $f_c$ is the cutoff frequency of the filter function, and in our cases $f_c = 0.5$ following the Nyquist Theorem (although sometimes we may vary $f_c$ by our software to some extent to suppress noise at the expense of the image resolution). We then back project all the convolved projections to achieve the reflectivity mapping image:

$$f(x,y) = \int_0^{\pi} g_{\varphi}(x\cos(\varphi) + y\sin(\varphi))d\varphi$$

where f(x, y) is the reflectivity at a local position labeled by **(x, y)**. The image is discretized into x-y grid, and interpolation is inevitable noticing we need back project the data at different in-plane angles. Here the simplest linear interpolation is employed.

## 7.5 Results and Discussions

We conducted preliminary tests by using a model sample: Carbon / Gold / Silicon layered ultrathin film. The sample was prepared by depositing gold on a pre-cleaned silicon substrate covered with the patterned kapton mask on an Emitech SC7620 sputtering machine, followed by sputtering a uniform carbon layer to bury the gold pattern by an ordinary carbon coater. A slice of square silicon (size: 10 mm × 10 mm) was used as the substrate. The Si substrate was pre-cleaned by several ultrasonic clean procedure: (1) ultrasonic washing with acetone for 10 minutes, (2) heated ultrasonication (55 ℃) in 1% $HNO_3$ for 30 minutes, (3) washing with distilled water. The procedures were repeated until the substrates surfaces were hydrophilic (because of a natural oxidized $SiO_2$ layer on the substrate surface). For the preparation of the gold pattern, sputtering time was chosen at 120 s to obtain the desired film thickness; for the fabrication of the carbon cover layer, we repeated 6 times of 60 s coating to obtain a uniform film with enough thickness. FIG. 7.4(a) shows the optical image of the gold pattern taken before covering the carbon uniform layer.

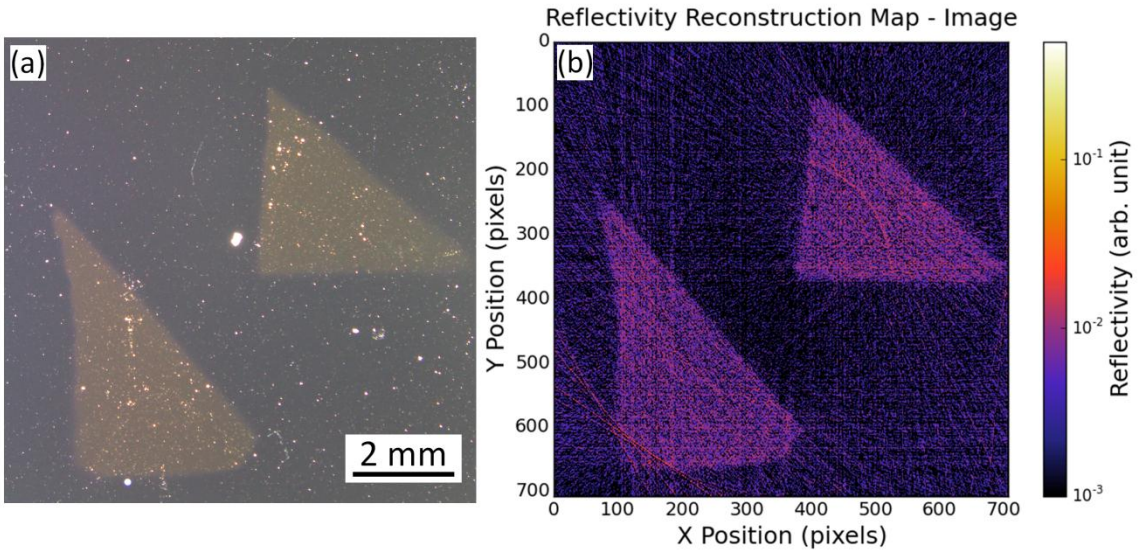


FIG. 7.4 An optical image of the pattern and an X-ray reflectivity image (with an X-ray wavelength of 1.54 Å) of the Carbon /Gold pattern (two triangles) /Si sample. LEFT: the optical image of the Gold pattern (two triangles) /Si sample before coating the uniform Carbon cover layer. The image was trimmed to have the same scale as the reconstructed image. RIGHT: the reconstructed reflectivity

image of the sample at specific incident angle θ = 6 mrad, with wavevector transfer $Q_z$ = 0.049 Å$^{-1}$. The data are plotted on logarithmic colorscale. Parameters for image reconstruction: 36 views, Cutoff frequency for Ram-Lak filter: 0.5.

In order to visualize the buried gold pattern, we set the incident angle of the X-ray beam at θ = 6 mrad, which in terms of wavevector transfer equals to $Q_z$ = 0.049 Å$^{-1}$. This $Q_z$ is larger than the critical wavevector transfer of carbon $Q_c$(C) = 0.031 Å$^{-1}$, that of silicon $Q_c$(Si) = 0.032 Å$^{-1}$, and smaller than that of gold $Q_c$(Au) = 0.078 Å$^{-1}$. Below the critical wavevector transfer $Q_c$, X-rays are totally reflected by the interface, while above the $Q_c$, X-ray reflectivity decreases rapidly. The X-ray reflectivity from the surface of the carbon film is ~ 1.5% at $Q_z$ = 0.049 Å$^{-1}$, and that from the silicon substrate is ~ 1.5%, while X-ray reflectivity from the interface between carbon and gold is ~85%, as shown in Table II calculated by Parratt's equation[6] with Python codes. Thereby at $Q_z$ = 0.049 Å$^{-1}$ X-rays easily penetrate the uniform carbon layer and are strongly reflected by the carbon / gold interface but weakly reflected by the carbon / silicon interface, thus we achieved an obvious contrast between the gold pattern and the silicon substrate, as shown in FIG. 7.4(b).

TABLE 7.2 Summary of critical wavevector transfers $Q_z$s (or critical angle using the Cu Kα X-rays source where λ=1.54 Å.) for different layers of the sample and calculated reflectivity values R (at $Q_z$ = 0.049 Å$^{-1}$) from each interface.

| Layer | $Q_c$ (Å$^{-1}$) | $\theta_c$ (mrad)$^{\lambda=1.54Å}$ | Interface | Reflectivity R (a. u.)$^{Qz = 0.049 Å-1}$ |
|---|---|---|---|---|
| C | 0.031 | 3.8 | Air /C | ~1.5% |
| Si | 0.032 | 3.9 | C / Si | ~1.5% |
| Au | 0.078 | 9.6 | C /Au | ~85% |

During the measurements, data were recorded every Δφ = 5 ° and there are 36 projections in the raw data, which were stored in a sinogram; exposure time was 1 min for each projection, and it is enough to obtain sufficient statistics because of the high reflectivity from the carbon / gold interface. The recorded projection data are reflected intensities (PSL, counts); they shall be normalized by the incident X-rays line profile (direct beam $I_0$, 1 min) which was also measured by the imaging plate in advance without the sample. In addition, the incident X-rays line profile (direct beam) may have some inherent intensity structures due to the non-uniformity of collimators or the X-ray source, which bring circle artifacts to the final reconstructed image. As a result, the normalization is necessary and important. FIG. 7.3(a) is the normalized sinogram of X-ray reflectivity projections data plotted as a function of in-plane angle φ at the wavevector transfer $Q_z$ = 0.049 Å$^{-1}$, where the data are plotted on a logarithmic colorscale. FIG. 7.3(b) is the extracted reflectivity projection line profiles at different specific in-plane rotational angle: blue open circle, φ = 0 °; red open right-triangle, φ = 50 °; and olive open star, φ = 135 °. The line profile at each in-plane angle φ is mathematically the integral of reflectivity intensities along the X-rays forward direction (which strongly depends on the in-plane angle φ) according to the Radon transform[70]:

$$p_\varphi(r) = \int_{-\infty}^{\infty} f(r\cos\phi - z\sin\phi, r\sin\phi + z\cos\phi)dz$$

where z is along the X-ray forward direction, r corresponds to the projection position on the imaging plate, f(x, y) is the reflectivity at a local point (x, y), φ is the in-plane angle, and $p_\varphi$(r) is the projection line profile at specific φ. The measurement of the sinogram is actually to integrate the 2D reflectivity mapping image to many 1D line profiles at different

in-plane angles φ, while the image reconstruction is to employ the set of 1D profiles to obtain a reconstructed 2D image. Specifically, at φ = 0 °, the projection line profile possesses two ridges which correspond to the two right triangle gold patterns, where X-rays come from the left hand side and so does the integrating direction. Because of the shape of right triangles, both ridges show steep slope at one side and slow slope at the other side. In addition, the right angle side of the bottom triangle at φ = 0 °[see the inset of FIG. 7.3(b)] is longer in the right angle side than that of top triangle, so we see higher integrated intensities in the bottom ridges, as shown in the FIG. 7.3 (b). At φ = 50 °, as shown in the inset of FIG. 7.3 (b) [where X-rays still impinge on the sample along the left to right direction], the projection line profile is consist of only one ridge. As the right triangle at φ = 50° [the bottom triangle at φ = 0 °] has a round shape at the short side corner, the top part of the line profile has a curved shape. On the other hand, because the long side corner of the right triangle is distorted and the side lenght is longer than that of the left triangle, we see a small hump at the bottom part of the line profile. At φ = 135 °, we observe two ridges again since the two triangles are separated again in the line profile because of the geometry as shown in the inset. Furthermore, the two ridges are thinner and the intensities are higher than that at φ = 0 °as the peak intensities correspond to the integrals along the hypotenuses of the right triangles. Compare with the two ridges, we see the curved slope at the top triangle at φ = 135° [the bottom triangle at φ = 0 °] but a quite straight slope at the other right triangle, which means the shape of the bottom triangle is better deposited. In the line profiles, we could also see that the integral intensities from the silicon part is quite low compared with that from the gold part, as shown in the pixel range 0~100 at each angle and in the pixel range 350~450 at φ = 135 °in FIG. 7.3. As demonstrated in the sinogram, the X-ray reflectivity imager has high sensitivity and even tiny pattern could be detected.

The image was reconstructed by our software based on Convolution Back-projection (CBP) algorithm. The cutting-off frequency was set as 0.5. The reconstructed image is displayed in FIG. 7.4(b) on a logarithmic colorscale. Although the gold pattern is buried by the uniform carbon layer, we clearly obtained the image of the gold pattern. The reconstructed image selectively visualized the gold pattern from the silicon substrate. In the image, we could easily discuss the pattern of the gold thin film in detail: (1) the left bottom right triangle is larger than the top right one; (2) the top right pattern is better shaped, while the right angle of the bottom triangle is not sharp (round) and the smallest acute angle is distorted. These two facts are the same information from the optical image taken before coating the carbon layer. We prepared the sample so we could have taken a photo before the pattern was covered. However, if the as-received sample has a covered top layer, or the interface experiences some dynamic changes, we obviously could not obtain the same information by the optical microscope, thus in such cases X-ray reflectivity imager stands out. In addition, even though we took the optical image before coating the carbon layer, the X-rays and visible light have different sensitivities as they have totally different energies. As we collect 36 views data [36 × 708] and the reconstructed image contains 708 × 708 pixels, the system is obviously a rank deficient tomography system[73]; We cannot quantitatively extract reflectivity from each pixel as in such systems the pixels values are smeared out to some extent. However, we could still see from the reconstructed image the reflectivity value from the gold area is $10 \sim 10^2$ times of the reflectivity from the silicon area, and it is a reasonable ratio. The views should be increased to obtain more quantitative information. However, for many cases we only need to see the different structures from the uniform part, where 36 projections data are usually sufficient. In addition, half of an hour measuring time is quite standard in laboratory experiments. In FIG. 7.4 (b) there still exist some artifacts: (1) the circle artifact in the top right triangle, which comes from the not perfect normalization (There were some dis-match when the normalization of the reflected intensity projections were applied); (2) some strips at the right angle of the bottom left triangle, which originates from the fact that the corner was out of the viewing area of X-rays in some views[see the sinogram in the range from φ = 110 °

to 150 ° in FIG. 7.3(a)]. These artifacts could be either avoided or neglected during the analysis as we know the origin and they don't obstruct drawing the same conclusion.

As mentioned in the Section 7.2, the in-plane spatial resolution is only limited by the size of the X-ray source, namely the micro-focus size (nominal focus size 35 μm). Although the in-plane spatial resolution may be degraded by the sparse views in the rank deficient case, the better resolution could be obtained by collecting enough views. Due to the fan beam geometry, the incident angles at different local positions of the sample are different: $\theta + \Delta(x, y)$. In the experiment θ = 6 mrad, and Δ(x, y) depends on the local positions:

$$\Delta(x, y) \approx -\frac{\theta \cdot x}{x + L_{SS}}$$

where $L_{SS}$ is the source to sample distance and is approximately 126 mm in the present version. In our geometry, we prefer and use the 'vertical' fan beam angle (equals to 4.55 °). On the other hand, the 'horizontal' angular divergence ( < 0.48 mrad, as shown in FIG. 7.5) is not ideal as we assume parallel beam in 'horizontal' direction in order to obtain the same grazing incident angle at the local positions. In the present samples, the contrast comes from the different reflectivity intensities from the total reflection region and another region. The allowance for the incident angle is quite large (2 ~10 mrad), the 0.48 mrad difference doesn't influence the result. On the other hand, we could achieve more sensitive images by de-convolution method in the interference region that may possess comparable image quality with X-ray reflectivity imaging in parallel beam geometry employing synchrotron radiation[91]. In fact, the result of the present example is the convolution of the reflectivity projection profile with the instrument function (angular divergence). By collecting many data at different $Q_z$ in a sequence, it is possible to de-convolve the reflectivity profile and extract the reflectivity projection at each $Q_z$, whereby obtain the reconstructed image at each $Q_z$.

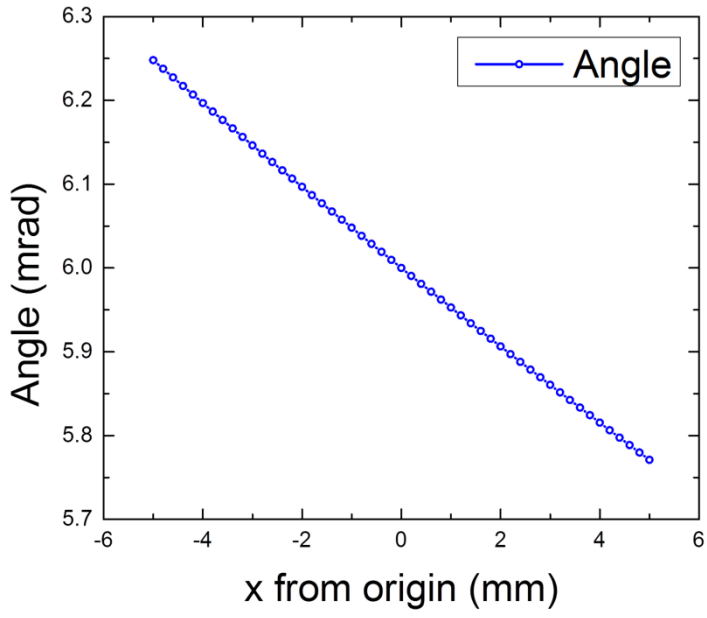


FIG. 7.5 True incident angles of the fan beam impinging on the sample surface plot other than the local positions **(x, y)**. The center is chosen as the origin, where the incident angle is θ = 6 mrad.

## 7.6 Conclusion

In summary, X-ray reflectivity imager utilizing laboratory 15W portable source in the fan beam geometry has been developed. It has been demonstrated that the imager is powerful in visualizing buried layers and interfaces even in a laboratory. X-ray reflectivity imager is based on routine X-ray reflectivity and image reconstruction scheme, so it has high sensitivity along the depth of ultrathin films. By employing a low power and a Ni filter, we are able to suppress high energy bremsstrahlung and remove the Cu Kβ X-rays, thus obtaining a monochromatic beam. By adopting proper collimators and a fan beam, we are capable of utilizing the beam divergence and achieving magnified images. We thereby largely improved the spatial resolution, which is only limited by the source size. We also confirmed the visualization ability of the imager for buried interfaces by a model sample, and then physical meaning of a reconstructed image is the 2D reflectivity distribution of the sample at a specific wavevector transfer.

# Chapter 8 Conclusion

We have explored buried functional interfaces by advanced X-ray scattering techniques, including formation of ultrathin Liesegang pattern and adhesive interface studies by X-ray reflectivity. (1) By controlling rather a low temperature (5.0 ± 1.0°C) and introducing equilibrium water vapor in the sample environment, we successfully obtained LPs in ultrathin films with a thickness down to 65 nm. The thicknesses of the films were measured by X-ray reflectivity technique in a nondestructive manner. At 5.0 ± 1.0 °C, gelatin hydrogel surface shows a hydrophobic nature, which helps prevent the gelatin from being wetted by rapid capillary wetting. This is the clear reason why we succeeded in obtaining LPs. We found that disconnected stain bands between the consecutive rings and/or interconnected patterns exist in ultrathin films in the outermost part of the pattern when enough time is given to let the pattern grow. Fine structures of the pattern in ultrathin gelatin films were also observed by the tapping mode atomic force microscope, and it was found that the Liesegang rings are composed of 300−600 nm laterally coagulated particles. Because of nanoscale scale thicknesses, such self-organized periodic structures will open up new opportunities in nanotechnologies. (2) We have also studied the hardening process of a commercial UV curing adhesives deposited on silicon substrate by XR. We found that the thicknesses of adhesive thin films decrease after curing. Better understanding interfacial structures by XR will aid in the rational design of adhesive interfaces that can withstand harsh stress testing conditions.

Aiming at solving many functional interfaces problems, We have successfully developed a novel X-ray reflectivity imaging technique which can visualize buried functional interfaces in ultrathin films by employing both synchrotron radiation and laboratory portable X-ray source. By collecting a series of reflection projection intensity profiles during an in-plane rotational scan of the sample, under grazing-incidence reflection geometry, we are able to obtain the X-ray reflectivity image by applying mathematical image reconstruction methods. The physical meaning of the reconstructed image is the 2D reflectivity distribution of the sample at specific wavevector transfer. (1) In case of synchrotron radiation, by tuning the grazing angle we have successfully obtained different image contrasts, which indicate that different in-depth structures were enhanced. The different X-ray reflectivities at local in-plane areas of thin films at a specific wavevector transfer correspond to different in-plane structures of the sample. By comparing different images at different incident angles, we not only visualized buried interfaces but also obtained nice contrasts in tiny thickness differences (in the order of Å). We also confirmed that the in-plane spatial resolution is better than 20 μm. This technique provides high in-depth sensitivity (Å) with quite good spatial resolution (20 μm). (2) In addition, by combining in-plane angle scan and grazing incident angle scan, we are able to reconstruct a series of interface sensitive X-ray reflectivity images at different grazing incident angles. The physical meaning of a reconstructed X-ray reflectivity image at specific wavevector transfers is the 2D reflectivity distribution of the sample. Thereby we are able to pick up the micro X-ray reflectivity profiles at different local positions of the sample, where the spatial resolution of the μXR is decided by the pixel size of the reconstructed XRI images. (3) Furthermore, X-ray reflectivity imager utilizing a laboratory 15 W portable X-ray source in fan beam geometry has been developed. It has been demonstrated that

the imager is powerful in visualizing buried layers and interfaces even in a laboratory. By employing a low power and a Ni filter, we are able to suppress high energy bremsstrahlung and remove the Cu Kβ X-rays, thus obtaining a monochromatic beam. By adopting proper collimators and a fan beam, we are capable of utilizing the beam divergence and achieving magnified images. We thereby largely improved the spatial resolution, which is only limited by the source size.

# Appendix Python Computer Programs

Listings are given here of python computer programs which have been used to generate some of the figures and process of the data in this thesis.

## A.1 Computer programs used in Chapter 4

This is Jinxing's Algebraic Reconstruction Simulation software, dealing with forward problem, which is able to simulate the sinograms from images with given number of angles. The original image, generated sinograms and the forward matrix can be plotted and saved as 2D matices.

```
import pandas as pd
import matplotlib.pyplot as plt
import matplotlib.cm as cm
from Tkinter import *
import math
import numpy as np

class LinearSystem():

    def __init__(self, Jin):

        self.lbl_dir = Label(Jin, text='File directory: ')
        self.lbl_dir.grid(row=0, column=0)
        self.ent_dir = Entry(Jin, bd=5)
        self.ent_dir.grid(row=0, column=1)
        self.ent_dir.insert(0, 'Directory of the image')

        self.lbl_file = Label(Jin, text='File Name: ')
        self.lbl_file.grid(row=0, column=2)
        self.ent_file = Entry(Jin, bd=5)
        self.ent_file.grid(row=0, column=3)
        self.ent_file.insert(0, 'The Excel file of the Image.xlsx')

        self.lbl_phi = Label(Jin, text='Num. of Angles: ')
        self.lbl_phi.grid(row=1, column=0)
        self.ent_phi = Entry(Jin, bd=8)
        self.ent_phi.grid(row=1, column=1)
        self.ent_phi.insert(0, '18')

        self.btn_img = Button(Jin, text = 'Plot orginal image', state = 'disabled', command = self.img_plot)
        self.btn_img.grid(row=0, column=4)

        self.btn_mat = Button(Jin, text = 'Obtain the sinogram', state = 'normal', command = self.btn_matrix)
        self.btn_mat.grid(row=1, column=2)

        self.btn_sav = Button(Jin, text = 'Save the matrix', state = 'disabled', command = self.btn_save)
        self.btn_sav.grid(row=1, column=3)

        self.btn_plt = Button(Jin, text = 'Plot Forward matrix', state = 'disabled', command = self.btn_plot)
        self.btn_plt.grid(row=1, column=4)

    def btn_matrix(self):
```

```
# set the other buttons enabled
self.btn_sav['state'] = 'normal'
self.btn_plt['state'] = 'normal'
self.btn_img['state'] = 'normal'

M_Dir = self.ent_dir.get() + self.ent_file.get()

Dataframe = pd.read_excel(M_Dir, header=None)
self.M_mtx = Dataframe.as_matrix()

print 'The model matrix: '
print self.M_mtx
print 'Columns: ' + str(len(self.M_mtx[0])) + ';  rows: ' + str(len(self.M_mtx))

# initiate the matrix dimension of the linear system, K pixels have K + 1 vertexes.
N = int(self.ent_phi.get())
K = int(len(self.M_mtx)) + 1
M = float(K-1)/2

self.G = [[0 for n in range((K-1)*(K-1))] for m in range(N*(K-1))]

for i in range(K-1):
    for j in range(K-1):
        xi0 = (float(i)-M)/M
        yj0 = (float(j)-M)/M
        xi1 = (float(i+1)-M)/M
        yj1 = (float(j+1)-M)/M

        for p in range(N):
            phi = p*(math.pi/N)

            t1, t2, t3, t4 = sorted([ xi0*math.cos(phi) + yj0*math.sin(phi),
                                      xi0*math.cos(phi) + yj1*math.sin(phi),
                                      xi1*math.cos(phi) + yj1*math.sin(phi),
                                      xi1*math.cos(phi) + yj0*math.sin(phi) ])
            if phi == 0:
                for k in range(K-1):
                    t = 2*(k+0.5)/(K-1) - 1
                    if t > t1 and t < t4:
                        self.G[p*(K-1)+k][i*(K-1)+j] = 1/float(M)

            elif phi == 90:
                for k in range(K-1):
                    t = 2*(k+0.5)/(K-1) - 1
                    if t > t1 and t < t4:
                        self.G[p*(K-1)+k][i*(K-1)+j] = 1/float(M)
            else:

                for k in range(K-1):
                    t = 2*(k+0.5)/(K-1) - 1

                    if t > t1 and t < t2:
                        self.G[p*(K-1)+k][i*(K-1)+j] = abs((t-t1)/math.sin(phi)/math.cos(phi))

                    elif t >= t2 and t <= t3:
                        self.G[p*(K-1)+k][i*(K-1)+j] = min(1/abs(math.sin(phi)),1/abs(math.cos(phi)))/M

                    elif t > t3 and t < t4:
                        self.G[p*(K-1)+k][i*(K-1)+j] = abs((t-t4)/math.sin(phi)/math.cos(phi))


self.D = np.dot(self.G, np.reshape(self.M_mtx,((K-1)*(K-1),1)))
self.S = np.reshape(self.D,(N,(K-1)))
```

```
        # plot the sinogram

        plt.title('Sinogram by Forward Equation', fontsize = 18, position = [.5, 1.02])
        plt.ylim(0,len(self.S[0]))
        plt.ylabel('Projection Position (pixels)', fontsize = 18)
        plt.xlabel('Rotation intervals (arb. unit)', fontsize = 18)
        cmap = cm.get_cmap('CMRmap')
        cs = plt.pcolor(self.S.transpose(), cmap = cmap)
        cb = plt.colorbar(cs, orientation = 'vertical', fraction = 0.04, pad = 0.06)
        cb.set_label('Intensity (arb. unit)', fontsize = 18)
        plt.show()

    def btn_save(self):

        # write to xlsx file

        G_mtx = pd.DataFrame(data=self.G)
        writer = pd.ExcelWriter(self.ent_dir.get()+self.ent_file.get()+'-G.xlsx')
        G_mtx.to_excel(writer,'Forward Marix', header=False, index=False)
        D_mtx = pd.DataFrame(data=self.D)
        D_mtx.to_excel(writer,'Data Marix', header=False, index=False)
        S_mtx = pd.DataFrame(data=self.S.transpose())
        S_mtx.to_excel(writer,'Sinogram Marix', header=False, index=False)
        writer.save()

    def img_plot(self):

        # plot the original image

        plt.title('Original image matrix', fontsize = 18, position = [.5, 1.02])
        plt.ylim(0,len(self.M_mtx[0]))
        plt.xlim(0,len(self.M_mtx))
        plt.ylabel('Y Position (pixels)', fontsize = 18)
        plt.xlabel('X Position (pixels)', fontsize = 18)
        cmap = cm.get_cmap('CMRmap')
        cs = plt.pcolor(self.M_mtx, cmap = cmap)
        cb = plt.colorbar(cs, orientation = 'vertical', fraction = 0.04, pad = 0.06)
        cb.set_label('Intensity (arb. unit)', fontsize = 18)
        plt.show()

    def btn_plot(self):

        # plot forward matrix
        plt.title('Forward matrix G', fontsize = 18, position = [.5, 1.02])
        plt.ylim(len(self.G),0)
        plt.ylabel('Varying detector positions [t] and angles [p]', fontsize = 18)
        plt.xlabel('Varying image pixels [i, j]', fontsize = 18)
        cmap = cm.get_cmap('CMRmap')
        cs = plt.imshow(self.G, cmap = cmap)
        cb = plt.colorbar(cs, orientation = 'vertical', fraction = 0.04, pad = 0.06)
        cb.set_label('Weighting (arb. unit)', fontsize = 18)
        plt.show()

Jin = Tk()
Jin.title('Algebraic Reconstruction Simulation software - Forward Projector')
linearsystem = LinearSystem(Jin)
Jin.mainloop()
```

This is Jinxing's Algebraic Reconstruction Simulation software, dealing with inverse problem, which is able to reconstruct images from sinograms stored in Excel files. The original sinogram, reconstructed image and the inverse matrix can be plotted and saved as 2D matices. In this simulation, either the Pseudo Inverse algorithm by singular value decomposition or truncated singular value decomposition is employed.

```
import pandas as pd
import matplotlib.pyplot as plt
import matplotlib.cm as cm
from Tkinter import *
import math
import numpy as np

class LinearSystem():

    def __init__(self, Jin):

        self.lbl_dir = Label(Jin, text='File directory: ')
        self.lbl_dir.grid(row=0, column=0)
        self.ent_dir = Entry(Jin, bd=5)
        self.ent_dir.grid(row=0, column=1)
        self.ent_dir.insert(0, ' Directory of the Sinogram ')

        self.lbl_file = Label(Jin, text='Sinogram Name: ')
        self.lbl_file.grid(row=0, column=2)
        self.ent_file = Entry(Jin, bd=5)
        self.ent_file.grid(row=0, column=3)
        self.ent_file.insert(0, ' The Excel file of the Sinogram.xlsx ')

        self.lbl_phi = Label(Jin, text='Num. of Angles: ')
        self.lbl_phi.grid(row=1, column=0)
        self.ent_phi = Entry(Jin, bd=8)
        self.ent_phi.grid(row=1, column=1)
        self.ent_phi.insert(0, '18')

        self.btn_mat = Button(Jin, text = ' Pseudo Inverse reconstruction', state = 'normal', command = self.btn_matrix)
        self.btn_mat.grid(row=1, column=2)

        self.btn_sav = Button(Jin, text = 'Save the matrix', state = 'disabled', command = self.btn_save)
        self.btn_sav.grid(row=1, column=3)

        self.btn_plt = Button(Jin, text = 'Plot Inverse matrix', state = 'disabled', command = self.btn_plot)
        self.btn_plt.grid(row=1, column=4)

        self.btn_sin = Button(Jin, text = 'Plot orginal sinogram', state = 'disabled', command = self.sin_plot)
        self.btn_sin.grid(row=0, column=4)

        self.btn_SVD = Button(Jin, text = 'SVD matrices of G', state = 'disabled', command = self.SVD_plot)
        self.btn_SVD.grid(row=2, column=0)

        self.lbl_cut = Label(Jin, text='rcond [TSVD]: ')
        self.lbl_cut.grid(row=2, column=1)
        self.ent_cut = Entry(Jin, bd=8)
        self.ent_cut.grid(row=2, column=2)
        self.ent_cut.insert(0, '0.2')

        self.btn_Tsv = Button(Jin, text = 'Apply the TSVD', state = 'disabled', command = self.btn_TSVD)
        self.btn_Tsv.grid(row=2, column=3)

    def btn_matrix(self):

        # set the other buttons enabled
        self.btn_sav['state'] = 'normal'
        self.btn_plt['state'] = 'normal'
```

```
self.btn_sin['state'] = 'normal'
self.btn_SVD['state'] = 'normal'
self.btn_Tsv['state'] = 'normal'

D_Dir = self.ent_dir.get() + self.ent_file.get()

Dataframe = pd.read_excel(D_Dir, sheetname='Sinogram Marix', header=None)
self.D_mtx = Dataframe.as_matrix().transpose()

print 'The data matrix: '
print self.D_mtx
print 'Columns: ' + str(len(self.D_mtx[0])) + ';  rows: ' + str(len(self.D_mtx))

# initiate the matrix dimension of the linear system, K pixels have K + 1 vertexes.
N = int(len(self.D_mtx))
K = int(len(self.D_mtx[0])) + 1
M = float(K-1)/2

self.G = [[0 for n in range((K-1)*(K-1))] for m in range(N*(K-1))]

for i in range(K-1):
    for j in range(K-1):
        xi0 = (float(i)-M)/M
        yj0 = (float(j)-M)/M
        xi1 = (float(i+1)-M)/M
        yj1 = (float(j+1)-M)/M

        for p in range(N):
            phi = p*(math.pi/N)

            t1, t2, t3, t4 = sorted([ xi0*math.cos(phi) + yj0*math.sin(phi),
                                      xi0*math.cos(phi) + yj1*math.sin(phi),
                                      xi1*math.cos(phi) + yj1*math.sin(phi),
                                      xi1*math.cos(phi) + yj0*math.sin(phi) ])
            if phi == 0:
                for k in range(K-1):
                    t = 2*(k+0.5)/(K-1) - 1
                    if t > t1 and t < t4:
                        self.G[p*(K-1)+k][i*(K-1)+j] = 1/float(M)


            elif phi == 90:
                for k in range(K-1):
                    t = 2*(k+0.5)/(K-1) - 1
                    if t > t1 and t < t4:
                        self.G[p*(K-1)+k][i*(K-1)+j] = 1/float(M)
            else:
                for k in range(K-1):
                    t = 2*(k+0.5)/(K-1) - 1

                    if t > t1 and t < t2:
                        self.G[p*(K-1)+k][i*(K-1)+j] = abs((t-t1)/math.sin(phi)/math.cos(phi))

                    elif t >= t2 and t <= t3:
                        self.G[p*(K-1)+k][i*(K-1)+j] = min(1/abs(math.sin(phi)),1/abs(math.cos(phi)))/M

                    elif t > t3 and t < t4:
                        self.G[p*(K-1)+k][i*(K-1)+j] = abs((t-t4)/math.sin(phi)/math.cos(phi))

# obtain the pseudo inverse of G, rcond is the TSVD point.

self.G_inv = np.linalg.pinv(self.G, rcond=1e-2)
```

```
        self.M = np.dot(self.G_inv, np.reshape(self.D_mtx,(N*(K-1),1)))

        self.Img = np.reshape(self.M,((K-1),(K-1))).transpose()

        # plot the image

        plt.title('Image by Pseudo Inverse', fontsize = 18, position = [.5, 1.02])
        plt.ylim(0,len(self.Img))
        plt.xlim(0,len(self.Img[0]))
        plt.ylabel('Y Position (pixels)', fontsize = 18)
        plt.xlabel('X Position (pixels)', fontsize = 18)
        cmap = cm.get_cmap('CMRmap')
        cs = plt.pcolor(self.Img.transpose(), cmap = cmap)
        cb = plt.colorbar(cs, orientation = 'vertical', fraction = 0.04, pad = 0.06)
        cb.set_label('Intensity (arb. unit)', fontsize = 18)
        # plt.axes().set_aspect('1.0')
        plt.show()

    def btn_save(self):

        # write to xlsx file

        G_mtx = pd.DataFrame(data=self.G)
        writer = pd.ExcelWriter(self.ent_dir.get()+self.ent_file.get()+'-G.xlsx')
        G_mtx.to_excel(writer,'Forward Marix')
        D_mtx = pd.DataFrame(data=self.D)
        D_mtx.to_excel(writer,'Data Marix')
        S_mtx = pd.DataFrame(data=self.S)
        S_mtx.to_excel(writer,'Sinogram Marix')
        writer.save()

    def sin_plot(self):

        # plot the original sinogram

        plt.title('Original Sinogram matrix', fontsize = 18, position = [.5, 1.02])
        plt.ylim(0,len(self.D_mtx[0]))
        plt.ylabel('Projection Position (pixels)', fontsize = 18)
        plt.xlabel('Rotation intervals (arb. unit)', fontsize = 18)
        cmap = cm.get_cmap('CMRmap')
        cs = plt.pcolor(self.D_mtx.transpose(), cmap = cmap)
        cb = plt.colorbar(cs, orientation = 'vertical', fraction = 0.04, pad = 0.06)
        cb.set_label('Intensity (arb. unit)', fontsize = 18)
        plt.show()

    def btn_plot(self):

        # plot forward matrix

        plt.title('Inverse matrix G', fontsize = 18, position = [.5, 1.02])
        plt.xlabel('Varying detector positions [t] and angles [p]', fontsize = 18)
        plt.ylabel('Varying image pixels [i, j]', fontsize = 18)
        cmap = cm.get_cmap('CMRmap')
        cs = plt.imshow(self.G_inv, cmap = cmap)
        cb = plt.colorbar(cs, orientation = 'vertical', fraction = 0.04, pad = 0.06)
        cb.set_label('Weighting (arb. unit)', fontsize = 18)
        plt.show()

    def SVD_plot(self):

        U, S, VT = np.linalg.svd(self.G, full_matrices=1, compute_uv=1)
```

```
        # plot singular values
        plt.title('Singular values of G', fontsize = 18, position = [.5, 1.02])
        plt.plot(S)
        plt.show()


    def btn_TSVD(self):

        # initiate the matrix dimension of the linear system, K pixels have K + 1 vertexes.
        N = int(len(self.D_mtx))
        K = int(len(self.D_mtx[0])) + 1
        M = float(K-1)/2

        # obtain the pseudo inverse of G, rcond is the truncate point.

        self.G_inv = np.linalg.pinv(self.G, rcond=float(self.ent_cut.get()))

        self.M = np.dot(self.G_inv, np.reshape(self.D_mtx,(N*(K-1),1)))

        self.Img = np.reshape(self.M,((K-1),(K-1))).transpose()

        # plot the image

        plt.title('Image by Pseudo Inverse', fontsize = 18, position = [.5, 1.02])
        plt.ylim(0,len(self.Img))
        plt.xlim(0,len(self.Img[0]))
        plt.ylabel('Y Position (pixels)', fontsize = 18)
        plt.xlabel('X Position (pixels)', fontsize = 18)
        cmap = cm.get_cmap('CMRmap')
        cs = plt.pcolor(self.Img.transpose(), cmap = cmap)
        cb = plt.colorbar(cs, orientation = 'vertical', fraction = 0.04, pad = 0.06)
        cb.set_label('Intensity (arb. unit)', fontsize = 18)
        plt.show()

Jin = Tk()
Jin.title(' Algebraic Reconstruction Simulation software - Image Reconstructor')
linearsystem = LinearSystem(Jin)
Jin.mainloop()
```

## A.2 Computer programs used in Chapter 5

This is Jinxing's Convolution Back Projection image reconstruction software, which is able to reconstruct images from sinograms stored in Excel files.

```
import pandas as pd
import matplotlib.pyplot as plt
import matplotlib.cm as cm
from Tkinter import *
import math
import numpy as np

class CBP():

    def __init__(self, Jin):

        self.lbl_dir = Label(Jin, text='File directory: ')
        self.lbl_dir.grid(row=0, column=0)
        self.ent_dir = Entry(Jin, bd=5)
        self.ent_dir.grid(row=0, column=1)
        self.ent_dir.insert(0, ' Directory of the Sinogram ')

        self.lbl_file = Label(Jin, text='Sinogram Name: ')
        self.lbl_file.grid(row=0, column=2)
        self.ent_file = Entry(Jin, bd=5)
        self.ent_file.grid(row=0, column=3)
        self.ent_file.insert(0, ' The Excel file of the Sinogram.xlsx ')

        self.btn_sin = Button(Jin, text = 'Plot orginal sinogram', state = 'disabled', command = self.sin_plot)
        self.btn_sin.grid(row=0, column=4)

        self.lbl_ram = Label(Jin, text='Cutoff frequency: ')
        self.lbl_ram.grid(row=1, column=0)
        self.ent_ram = Entry(Jin, bd=8)
        self.ent_ram.grid(row=1, column=1)
        self.ent_ram.insert(0, '0.5')

        self.btn_mat = Button(Jin, text = 'Ordinary CBP', state = 'normal', command = self.btn_matrix)
        self.btn_mat.grid(row=1, column=2)

        self.btn_sav = Button(Jin, text = 'Save the matrix', state = 'disabled', command = self.btn_save)
        self.btn_sav.grid(row=1, column=3)

    def btn_matrix(self):

        # set the other buttons enabled
        self.btn_sav['state'] = 'normal'
        self.btn_sin['state'] = 'normal'

        D_Dir = self.ent_dir.get() + self.ent_file.get()

        Dataframe = pd.read_excel(D_Dir, sheetname='Sinogram Marix')
        self.D_mtx = Dataframe.as_matrix().transpose()

        print 'The data matrix: '
        print self.D_mtx
        print 'Columns: ' + str(len(self.D_mtx[0])) + ';  rows: ' + str(len(self.D_mtx))

        # initiate the matrix dimension, S angles, N pixels.
        S = int(len(self.D_mtx))
        N = int(len(self.D_mtx[0]))
```

```
        # initiate ramp in real domain
        ramp = np.zeros(N)
        fc = float(self.ent_ram.get())
        for n in range(N):
            m = (n-N/2)
            if m == 0:
                ramp[n] = fc**2
            else:
                ramp[n] = fc*math.sin(2*math.pi*m*fc)/(math.pi*m)-(math.sin(math.pi*m*fc)/(math.pi*m))**2

        plt.figure()
        plt.title('Ramp Filter in real domain, Cutoff freq. = '+self.ent_ram.get(), fontsize = 18)
        plt.plot(ramp)
        plt.show()

        # convolve projections with the ramp, notice size doubled by convolution
        conv = np.zeros((S,2*N-1))
        self.g = np.zeros((S,N))

        for s in range(S):
            conv[s] = np.convolve(self.D_mtx[s], ramp)

        for s in range(S):
            for n in range(N):
                self.g[s][n] = conv[s][n+N/2]

        # Final back projecting all the reflection projections
        self.f = np.zeros((N,N))
        for i in range(N):
            for j in range(N):
                for s in range(S):
                    x = (i-N/2)
                    y = (j-N/2)
                    h = x*math.cos(s*math.pi/S)+y*math.sin(s*math.pi/S)
                    d = int(math.floor(h)+N/2)
                    if d >= 0 and (d+1) < N:
                        self.f[i,j] = self.f[i,j] + self.g[s, d]*(math.floor(h)+1-h) + self.g[s, d+1]*(h-math.floor(h))

        # plot the image

        plt.figure()
        plt.title('Image by CBP, Cutoff freq. = '+self.ent_ram.get(), fontsize = 18, position = [.5, 1.02])

        plt.ylim(0,len(self.f))
        plt.xlim(0,len(self.f[0]))
        plt.ylabel('Y Position (pixels)', fontsize = 18)
        plt.xlabel('X Position (pixels)', fontsize = 18)
        cmap = cm.get_cmap('CMRmap')
        cs = plt.pcolor(self.f, cmap = cmap)
        cb = plt.colorbar(cs, orientation = 'vertical', fraction = 0.04, pad = 0.06)
        cb.set_label('Intensity (arb. unit)', fontsize = 18)
        plt.axes().set_aspect('1.0')
        plt.show()


    def btn_save(self):

        # write to xlsx file
        f_mtx = pd.DataFrame(data=self.f)
        writer = pd.ExcelWriter(self.ent_dir.get()+self.ent_file.get()+'_CBP_Cutoff_'+self.ent_ram.get()+'.xlsx')
        f_mtx.to_excel(writer,'CBP reflectivity Marix')
        writer.save()
```

```
    def sin_plot(self):

        # plot the original sinogram

        plt.title('Original Sinogram matrix', fontsize = 18, position = [.5, 1.02])
        plt.ylim(0,len(self.D_mtx[0]))
        plt.ylabel('Projection Position (pixels)', fontsize = 18)
        plt.xlabel('Rotation intervals (arb. unit)', fontsize = 18)
        cmap = cm.get_cmap('CMRmap')
        cs = plt.pcolor(self.D_mtx.transpose(), cmap = cmap)
        cb = plt.colorbar(cs, orientation = 'vertical', fraction = 0.04, pad = 0.06)
        cb.set_label('Intensity (arb. unit)', fontsize = 18)
        plt.show()

Jin = Tk()
Jin.title('Convolution Back Projection Image Reconstructor')
cBP = CBP(Jin)
Jin.mainloop()
```

## A.3 Computer programs used in Chapter 6

This is Jinxing's XRR Profiling, reading XRR profiles from a series of X-ray Reflectivity Images, as shown in FIG. 6.7. The software plot the micro X-ray reflectivity profiles at the point of interest and/or region of interest specified.

```
import pandas as pd
import matplotlib.pyplot as plt
import matplotlib.cm as cm
from Tkinter import *
import math
import numpy as np
from shapely.geometry import Point
from shapely.geometry.polygon import Polygon

class LinearSystem():
    def __init__(self, Jin):

        self.lbl_dir = Label(Jin, text='File directory: ')
        self.lbl_dir.grid(row=0, column=0)
        self.ent_dir = Entry(Jin, bd=5)
        self.ent_dir.grid(row=0, column=1)
        self.ent_dir.insert(0, ' Directory of the Sinogram ')

        self.lbl_file = Label(Jin, text='Data file name: ')
        self.lbl_file.grid(row=0, column=2)
        self.ent_file = Entry(Jin, bd=5)
        self.ent_file.grid(row=0, column=3)
        self.ent_file.insert(0, ' The Excel file of the XRI images (column – pixels, row – incident angles).xlsx ')

        self.lbl_xpos = Label(Jin, text='X position: ')
        self.lbl_xpos.grid(row=1, column=0)
        self.ent_xpos = Entry(Jin, bd=5)
        self.ent_xpos.grid(row=1, column=1)
        self.ent_xpos.insert(0, '70')

        self.lbl_ypos = Label(Jin, text='Y position: ')
        self.lbl_ypos.grid(row=1, column=2)
        self.ent_ypos = Entry(Jin, bd=5)
        self.ent_ypos.grid(row=1, column=3)
        self.ent_ypos.insert(0, '30')

        self.lbl_size = Label(Jin, text='Image size: ')
        self.lbl_size.grid(row=2, column=2)
        self.ent_size = Entry(Jin, bd=5)
        self.ent_size.grid(row=2, column=3)
        self.ent_size.insert(0, '90')

        self.lbl_xpos = Label(Jin, text='LeftUp point (1st line_X): ')
        self.lbl_xpos.grid(row=3, column=0)
        self.lbl_ypos = Label(Jin, text='LeftDown point: ')
        self.lbl_ypos.grid(row=3, column=1)
        self.lbl_xpos = Label(Jin, text='RightUp point: ')
        self.lbl_xpos.grid(row=3, column=2)
        self.lbl_ypos = Label(Jin, text='RightDown point: ')
        self.lbl_ypos.grid(row=3, column=3)

        self.ent_x0pos = Entry(Jin, bd=5)
        self.ent_x0pos.grid(row=4, column=0)
        self.ent_x0pos.insert(0, '55')
        self.ent_y0pos = Entry(Jin, bd=5)
        self.ent_y0pos.grid(row=5, column=0)
        self.ent_y0pos.insert(0, '25')
```

```
        self.ent_x1pos = Entry(Jin, bd=5)
        self.ent_x1pos.grid(row=4, column=1)
        self.ent_x1pos.insert(0, '55')
        self.ent_y1pos = Entry(Jin, bd=5)
        self.ent_y1pos.grid(row=5, column=1)
        self.ent_y1pos.insert(0, '45')

        self.ent_x2pos = Entry(Jin, bd=5)
        self.ent_x2pos.grid(row=4, column=2)
        self.ent_x2pos.insert(0, '75')
        self.ent_y2pos = Entry(Jin, bd=5)
        self.ent_y2pos.grid(row=5, column=2)
        self.ent_y2pos.insert(0, '25')

        self.ent_x3pos = Entry(Jin, bd=5)
        self.ent_x3pos.grid(row=4, column=3)
        self.ent_x3pos.insert(0, '75')
        self.ent_y3pos = Entry(Jin, bd=5)
        self.ent_y3pos.grid(row=5, column=3)
        self.ent_y3pos.insert(0, '45')

        self.btn_load = Button(Jin, text = 'Load X-ray reflectivity images', state = 'normal', command = self.load_xri)
        self.btn_load.grid(row=2, column=0)

        self.btn_xrr = Button(Jin, text = 'X-ray reflectivity at the position', state = 'disabled', command = self.plt_xrr)
        self.btn_xrr.grid(row=2, column=1)

        self.btn_ixr = Button(Jin, text = 'X-ray reflectivity at the area', state = 'disabled', command = self.plt_ixr)
        self.btn_ixr.grid(row=6, column=1)

    def load_xri(self):

        # set the other buttons enabled
        self.btn_xrr['state'] = 'normal'
        self.btn_ixr['state'] = 'normal'

        Dataframe = pd.read_excel(self.ent_dir.get()+self.ent_file.get())
        self.xri_mtx = Dataframe.as_matrix()

        # import the normalization factor
        N_Dir = self.ent_dir.get() + 'Norm Factor.xlsx'
        N_frame = pd.read_excel(N_Dir, header=None)
        self.N_fac = N_frame.as_matrix()

    def plt_xrr(self):

        cln = int(self.ent_size.get())*int(self.ent_ypos.get())+int(self.ent_xpos.get())

        fig, axarr = plt.subplots(1, 2, figsize=(12,6.5))

        fig.suptitle('X-ray reflectivity at pixel ('+str(self.ent_xpos.get())+', '+str(self.ent_ypos.get())+')', fontsize = 18)

        axarr[0].set_title('Linear Scale', position = [.5, 0.9], fontsize = 18)
        axarr[0].plot(self.xri_mtx[:,cln], 'ro--', markersize=8)
        plt.grid(True)

        axarr[1].set_title('Semilog Scale', position = [.5, 0.9], fontsize = 18)
        axarr[1].semilogy(self.xri_mtx[:,cln], 'b*-', markersize=8)
        axarr[1].set_ylabel('X-ray reflectivity (a. u.)', fontsize = 16)
        axarr[1].set_xlabel('Incident angle (mrad)', fontsize = 16, position = [.5, 0.04])
        axarr[1].set_xticks(np.arange(0,len(self.xri_mtx),len(self.xri_mtx)/10), minor=False)
```

```
        axarr[1].set_xticklabels([str((t*20+700)/286.0)[:3] for t in np.arange(0,len(self.xri_mtx), len(self.xri_mtx)/10)])

        plt.grid(True)

        plt.figure()
        plt.title('X-ray reflectivity at pixel ('+str(self.ent_xpos.get())+', '+str(self.ent_ypos.get())+')', fontsize = 18)
        plt.semilogy(np.multiply(self.xri_mtx[:,cln],self.N_fac[:,1]), 'cp-', markersize=8)
        plt.ylabel('X-ray reflectivity (a. u.)', fontsize = 18)
        plt.xlabel('Wavevector transfer $Q_z$ (${\AA}^{-1}$)', fontsize = 18)
        plt.axes().set_xticks(np.arange(0,len(self.xri_mtx[:,cln])+1,10), minor=False)
        Qz = ['%06.4f'%4*math.pi*math.sin(float(p*20+540)/286)/770 for p in np.arange(0,len(self.xri_mtx[:,cln])+1,10)]
        plt.axes().set_xticklabels(Qz, rotation='vertical', fontsize = 14)
        plt.show()

    def plt_ixr(self):

        # obtain area of interest

        x0 = int(self.ent_x0pos.get())
        y0 = int(self.ent_y0pos.get())

        x1 = int(self.ent_x1pos.get())
        y1 = int(self.ent_y1pos.get())

        x2 = int(self.ent_x2pos.get())
        y2 = int(self.ent_y2pos.get())

        x3 = int(self.ent_x3pos.get())
        y3 = int(self.ent_y3pos.get())

        xmin = min(x0,x1,x2,x3)
        xmax = max(x0,x1,x2,x3)
        ymin = min(y0,y1,y2,y3)
        ymax = max(y0,y1,y2,y3)

        polygon = Polygon([(x0,y0),(x1,y1),(x3,y3),(x2,y2)])

        self.ixr = [0 for i in range(len(self.xri_mtx[:,0]))]

        for y in range(ymin,ymax+1):
            for x in range(xmin,xmax+1):
                point = Point(x, y)
                cln = int(self.ent_size.get())*y+x
                if polygon.contains(point):
                    self.ixr = self.ixr + self.xri_mtx[:,cln]

        plt.figure()
        plt.title('X-ray reflectivity at area of interest', position = [.5, 1.04], fontsize = 18)
        plt.semilogy(np.multiply(self.ixr, self.N_fac[:,1]), 'cp-', markersize=8)
        plt.ylabel('X-ray reflectivity (a. u.)', fontsize = 18)
        plt.xlabel('Wavevector transfer $Q_z$ (${\AA}^{-1}$)', fontsize = 18)
        plt.axes().set_xticks(np.arange(0,len(self.ixr)+1,10), minor=False)
        Qz = ['%06.4f'%4*math.pi*math.sin(float(p*20+540)/286)/770 for p in np.arange(0,len(self.xri_mtx[:,cln])+1,10)]
        plt.axes().set_xticklabels(Qz, rotation='vertical', fontsize = 14)

Jin = Tk()
Jin.title('X-ray reflectivity profile reader')
linearsystem = LinearSystem(Jin)
Jin.mainloop()
```

## A.4 Computer programs used in Chapter 7

This is Jinxing's X-ray reflectivity imager control GUI software for reflectivity scan. The software gets communication with PM16C-4 motor controller, accepts the motion comments and sends the comments to the controller. Each time a log file is also generated to record the experimental parameters.

```
from Tkinter import *
import tkSimpleDialog
import datetime
import time
import visa

class Reflectivity_Scan():

    def __init__(self, Jin):

        self.rm = visa.ResourceManager()
        self.rm.list_resources()
        self.inst = self.rm.open_resource('GPIB::7::INSTR')
        print(self.inst.query('*IDN?'))
        self.inst.write('S1R')
        self.inst.write('S160')
        self.inst.write('S126')

        self.lbl_sam = Label(Jin, text='The sample name: ')
        self.lbl_sam.grid(row=0, column=0)
        self.lbl_ch0 = Label(Jin, text='Ch0 move pulses: ')
        self.lbl_ch0.grid(row=0, column=1)
        self.lbl_ch6 = Label(Jin, text='Ch6 move pulses: ')
        self.lbl_ch6.grid(row=0, column=2)
        self.lbl_num = Label(Jin, text='Repeatition number: ')
        self.lbl_num.grid(row=0, column=3)
        self.lbl_mea = Label(Jin, text='Measure time(sec): ')
        self.lbl_mea.grid(row=0, column=4)
        self.lbl_coo = Label(Jin, text='cooling time(sec): ')
        self.lbl_coo.grid(row=0, column=5)

        self.ent_sam = Entry(Jin, bd=5)
        self.ent_sam.insert(0,'Sample')
        self.ent_sam.grid(row=1, column=0)

        self.ent_ch0 = Entry(Jin, bd=5)
        self.ent_ch0.insert(0,'5')
        self.ent_ch0.grid(row=1, column=1)

        self.ent_ch6 = Entry(Jin, bd=5)
        self.ent_ch6.insert(0,'2500')
        self.ent_ch6.grid(row=1, column=2)

        self.ent_num = Entry(Jin, bd=5)
        self.ent_num.insert(0,'30')
        self.ent_num.grid(row=1, column=3)

        self.ent_mea = Entry(Jin, bd=5)
        self.ent_mea.insert(0,'60')
        self.ent_mea.grid(row=1, column=4)

        self.ent_coo = Entry(Jin, bd=5)
        self.ent_coo.insert(0,'60')
        self.ent_coo.grid(row=1, column=5)

        self.btn_scan = Button(Jin, text = 'Reflectivity Scan', command = self.btn_scan)
        self.btn_scan.grid(row=1, column=6)
```

```
    def btn_scan(self):

        # Specify interval angle in deg. Channel moving step, measuring time and waiting time (sec)

        num = int(self.ent_num.get())
        Ch0Pulse = int(self.ent_ch0.get())
        Ch6Pulse = int(self.ent_ch6.get())
        MeasTime = int(self.ent_mea.get())
        WaitTime = int(self.ent_coo.get())
        Sample = str(self.ent_sam.get())

        # Initiate the Log File to start record
        now = datetime.datetime.now()
        log_file = ' Directory '+Sample+'_ReflectivityScan_' + now.strftime("%I %M%p on %B %d, %Y") + '.txt'

        s = open(log_file, 'w')


        for n in range(0, num):

            # Transfer pulse value to String, "%07d" % left zero padding

            DPulse = '-' "%07d" % Ch0Pulse
            BPulse = '+' "%07d" % Ch6Pulse
            self.inst.write('WFFFE')
            self.inst.write('WFFFF')
            time.sleep(MeasTime)
            now = datetime.datetime.now()
            s.write('{:6s}'. format(str(n)))
            s.write('{:16s}'. format(now.strftime("%I %M%p on %B %d, %Y")))
            s.write('\n')

            print(str(n) + 'th exposure')
            time.sleep(10)
            self.inst.write('S3BR' + DPulse)
            time.sleep(5)
            self.inst.write('S33R' + BPulse)
            time.sleep(WaitTime)
            print 'Cooling Finished! 5 sec to go'
            time.sleep(5)

        now = datetime.datetime.now()
        s.write('\n')
        s.write('Measurement Finished at' + now.strftime("%I, %M%p on %B %d, %Y") + '!')
        s.close()

        # Go back to zero position
        self.inst.write('B6-0300')
        self.inst.write('S33A+0000000B')

        time.sleep(30)
        print 'Moving back to original position!'

Jin = Tk()
Jin.title('X-ray Reflectivity_Scan, Jinxing Jan. 2016')
reflectivity_scan = Reflectivity_Scan(Jin)
Jin.mainloop()
```

This is Jinxing's X-ray reflectivity imager control GUI software for sinogram scan. The software gets communication with PM16C-4 motor controller, accepts the motion comments and sends the comments to the controller. Each time a log file is also generated to record the experimental parameters.

```
from Tkinter import *
import tkMessageBox
import datetime
import time
import visa

class XRImager_Scan():

    def __init__(self, Jin):

        self.rm = visa.ResourceManager()
        self.rm.list_resources()
        self.inst = self.rm.open_resource('GPIB::7::INSTR')
        print(self.inst.query('*IDN?'))
        self.inst.write('S1R')
        self.inst.write('S113')
        self.inst.write('S126')


        self.lbl_sam = Label(Jin, text='The sample name: ')
        self.lbl_sam.grid(row=0, column=0)
        self.lbl_ang = Label(Jin, text='Angle interval (deg.): ')
        self.lbl_ang.grid(row=0, column=1)
        self.lbl_ch6 = Label(Jin, text='Ch6 move pulses: ')
        self.lbl_ch6.grid(row=0, column=2)
        self.lbl_mea = Label(Jin, text='Measure time(sec): ')
        self.lbl_mea.grid(row=0, column=3)
        self.lbl_coo = Label(Jin, text='cooling time(sec): ')
        self.lbl_coo.grid(row=0, column=4)

        self.ent_sam = Entry(Jin, bd=5)
        self.ent_sam.insert(0,'Sample')
        self.ent_sam.grid(row=1, column=0)

        self.ent_ang = Entry(Jin, bd=5)
        self.ent_ang.insert(0,'5')
        self.ent_ang.grid(row=1, column=1)

        self.ent_ch6 = Entry(Jin, bd=5)
        self.ent_ch6.insert(0,'2500')
        self.ent_ch6.grid(row=1, column=2)

        self.ent_mea = Entry(Jin, bd=5)
        self.ent_mea.insert(0,'120')
        self.ent_mea.grid(row=1, column=3)

        self.ent_coo = Entry(Jin, bd=5)
        self.ent_coo.insert(0,'120')
        self.ent_coo.grid(row=1, column=4)

        self.btn_scan = Button(Jin, text = 'XRImager Scan', command = self.btn_scan)
        self.btn_scan.grid(row=1, column=6)

    def btn_scan(self):

        # Specify interval angle phi in degree. Channel moving step, measuring time and waiting time (sec)

        Phi = float(self.ent_ang.get())
        Ch6Pulse = int(self.ent_ch6.get())
```

```
        MeasTime = int(self.ent_mea.get())
        WaitTime = int(self.ent_coo.get())
        Sample = str(self.ent_sam.get())

        # Log File
        now = datetime.datetime.now()
        log_file = ' Directory '+Sample+'_XRImager_Scan' + now.strftime("%I %M%p on %B %d, %Y") + '.txt'

        s = open(log_file, 'w')
        s.write('Interval angle:' + str(Phi) + '; Exposure time:' + str(MeasTime))

        num = int((180/Phi))
        for n in range(0, num):
            # Transfer pulse value to String, "%07d" % left zero padding

            APulse = '+' "%07d" % int(Phi*400)
            BPulse = '+' "%07d" % Ch6Pulse
            self.inst.write('WFFFE')
            self.inst.write('WFFFF')
            time.sleep(MeasTime)
            now = datetime.datetime.now()
            s.write('{:6s}'. format(str(n)))
            s.write('{:16s}'. format(now.strftime("%I %M%p on %B %d, %Y")))
            s.write('\n')

            print(str(n) + 'th exposure')
            time.sleep(10)
            self.inst.write('S32R' + APulse)
            time.sleep(5)
            self.inst.write('S33R' + BPulse)
            time.sleep(5)
            time.sleep(WaitTime)
            print 'Move and wait Finished!'

            if int(n/36.0) – n/36.0 == 0 :
                tkMessageBox.ShowInfo('Warning!', 'Change new image plate!')

        now = datetime.datetime.now()
        s.write('\n')
        s.write('Measurement Finished at' + now.strftime("%I, %M%p on %B %d, %Y") + '!')
        s.close()

        # Go back to zero position
        self.inst.write('B3-0300')
        self.inst.write('B6-0300')
        self.inst.write('S32A-0036000B')
        self.inst.write('S33A+0000000B')

        time.sleep(30)
        print 'Moving back to original position!'

Jin = Tk()
Jin.title(' X-ray Reflectivity Imager _Scan, Jinxing Jan. 2016')
xrimager _scan = XRImager _Scan(Jin)
Jin.mainloop()
```

# References


(1) Allara, D. L. A Perspective on Surfaces and Interfaces. *Nature* **2005**, *437* (7059), 638–639.

(2) Chandler, D. Interfaces and the Driving Force of Hydrophobic Assembly. *Nature* **2005**, *437* (7059), 640–647.

(3) Yin, Y.; Alivisatos, A. P. Colloidal Nanocrystal Synthesis and the Organic-Inorganic Interface. *Nature* **2005**, *437* (7059), 664–670.

(4) Daillant, J.; Gibaud, A. *X-Ray and Neutron Reflectivity: Principles and Applications*, 1st ed.; Springer: Berlin, 1999.

(5) Holý, V.; Pietsch, U.; Baumbach, T. High-Resolution X-Ray Scattering from Thin Films and Multilayers. *High-Resolution X-Ray Scatt. from Thin Film. Multilayers* **1999**, *149*, 81–112.

(6) Parratt, L. G. Surface Studies of Solids by Total Reflection of X-Rays. *Phys. Rev.* **1954**, *95* (2), 359.

(7) Sinha, S. K.; Sirota, E. B.; Garoff, S.; Stanley, H. B. X-Ray and Neutron Scattering from Rough Surfaces. *Phys. Rev. B* **1988**, *38* (4), 2297–2311.

(8) Holý, V.; Baumbach, T. Nonspecular X-Ray Reflection from Rough Multilayers. *Phys. Rev. B* **1994**, *49* (15), 10668–10676.

(9) Fenter, P.; Park, C.; Zhang, Z.; Wang, S. Observation of Subnanometre-High Surface Topography with X-Ray Reflection Phase-Contrast Microscopy. *Nat. Phys.* **2006**, *2* (10), 700–704.

(10) Roy, S.; Parks, D.; Seu, K. A.; Su, R.; Turner, J. J.; Chao, W.; Anderson, H. E.; Cabrini, S.; Kevan, S. D. Lensless X-Ray Imaging in Reflection Geometry. *Nat. Photonics* **2011**, *5* (4), 243–245.

(11) Sun, T.; Jiang, Z.; Strzalka, J.; Ocola, L.; Wang, J. Three-Dimensional Coherent X-Ray Surface Scattering Imaging near Total External Reflection. *Nat. Photonics* **2012**, *6* (9), 586–590.

(12) Liesegang, R. E. Über einige Eigenschaften von Gallerten. In *Naturwissenschaftliche Wochenschrift*; G. Fischer [etc.], 1896; Vol. 11, pp 353–362.

(13) Henisch, H. K. *Crystals in Gels and Liesegang Rings*; Cambridge University Press: Cambridge, 1988.

(14) Grzybowski, B. A. *Chemistry in Motion: Reaction-Diffusion Systems for Micro- and Nanotechnology*, First.; John Wiley and Sons: West Sussex, U.K., 2009.

(15) Sadek, S.; Sultan, R. Liesegang Patterns in Nature: A Diverse Scenery across the Sciences. In *Precipitation Patterns in Reaction-Diffusion Systems*; Lagzi, I., Ed.; Research Signpost: Trivandrum, India, 2010; Vol. 661, pp 1–43.

(16) Whitesides, G. M.; Grzybowski, B. Self-Assembly at All Scales. *Science (80-. ).* **2002**, *295* (5564), 2418–2421.

(17) Matalon, R.; Packter, A. The Liesegang Phenomenon. I. Sol Protection and Diffusion. *J. Colloid Sci.* **1955**, *10* (1), 46–62.

(18) Antal, T.; Droz, M.; Magnin, J.; Rácz, Z.; Zrinyi, M. Derivation of the Matalon-Packter Law for Liesegang Patterns. *J. Chem. Phys.* **1998**, *109* (21), 9479–9486.

(19) Shreif, Z.; Mandalian, L.; Abi-Haydar, A.; Sultan, R. Taming Ring Morphology in 2D Co(OH)2 Liesegang Patterns. *Phys. Chem. Chem. Phys.* **2004**, *6* (13), 3461.

(20) Lagzi, I.; Ueyama, D. Pattern Transition between Periodic Liesegang Pattern and Crystal Growth Regime in Reaction-Diffusion Systems. *Chem. Phys. Lett.* **2009**, *468* (4–6), 188–192.

(21) Lagzi, I. Controlling and Engineering Precipitation Patterns. *Langmuir* **2012**, *28* (7), 3350–3354.

(22) Toramaru, A.; Harada, T.; Okamura, T. Experimental Pattern Transitions in a Liesegang System. *Phys. D Nonlinear Phenom.* **2003**, *183* (1–2), 133–140.

(23) Matsuzawa, S.; Hondo, Y.; Kawauchi, Y.; Kume, M.; Yamaura, K.; Tanigami, T.; Ogasawara, K. Crystal Growth in Syndiotactic Poly(vinyl Alcohol) Hydrogels. *Colloid Polym. Sci.* **1987**, *265* (9), 810–814.

(24) Kárpáti-Smidróczki, É.; Büki, A.; Zrínyi, M. Pattern Forming Precipitation in Gels due to Coupling of Chemical Reactions with Diffusion. *Colloid Polym. Sci.* **1995**, *273* (9), 857–865.

(25) Smoukov, S. K.; Bitner, A.; Campbell, C. J.; Kandere-Grzybowska, K.; Grzybowski, B. A. Nano- and Microscopic Surface Wrinkles of Linearly Increasing Heights Prepared by Periodic Precipitation. *J. Am. Chem. Soc.* **2005**, *127* (50), 17803–17807.

(26) Bena, I.; Droz, M.; Rácz, Z. Formation of Liesegang Patterns in the Presence of an Electric Field. *J. Chem. Phys.* **2005**, *122* (20), 204502.

(27) Lagzi, I.; Izsak, F. Stochastic Description of Precipitate Pattern Formation in an Electric Field. *Phys. Chem. Chem. Phys.* **2003**, *5* (19), 4144–4148.

(28) Sultan, R.; Halabieh, R. Effect of an Electric Field on Propagating Co(OH)2 Liesegang Patterns. *Chem. Phys. Lett.* **2000**, *332* (3–4), 331–338.

(29) Al-Ghoul, M.; Sultan, R. Front Propagation in Patterned Precipitation. 2. Electric Effects in Precipitation−Dissolution Patterning Schemes. *J. Phys. Chem. A* **2003**, *107* (8), 1095–1101.

(30) Lagzi, I.; Kowalczyk, B.; Grzybowski, B. A. Liesegang Rings Engineered from Charged Nanoparticles. *J. Am. Chem. Soc.* **2010**, *132* (1), 58–60.

(31) El-Batlouni, H.; El-Rassy, H.; Al-Ghoul, M. Cosynthesis, Coexistence, and Self-Organization of Alpha- and Beta-Cobalt Hydroxide Based on Diffusion and Reaction in Organic Gels. *J. Phys. Chem. A* **2008**, *112* (34), 7755–7757.

(32) Magonov, S. N.; Elings, V.; Whangbo, M.-H. Phase Imaging and Stiffness in Tapping-Mode Atomic Force Microscopy. *Surf. Sci.* **1997**, *375* (2–3), L385–L391.

(33) Sakurai, K. Total-Reflection X-Ray Fluorescence Imaging. *Spectrochim. Acta Part B At. Spectrosc.* **1999**, *54* (10), 1497–1503.

(34) Sakurai, K.; Eba, H. Micro X-Ray Fluorescence Imaging without Scans: Toward an Element-Selective Movie. *Anal. Chem.* **2003**, *75* (2), 355–359.

(35) Lin, Y.; Boker, A.; He, J.; Sill, K.; Xiang, H.; Abetz, C.; Li, X.; Wang, J.; Emrick, T.; Long, S.; et al. Self-Directed Self-Assembly of Nanoparticle/copolymer Mixtures. *Nature* **2005**, *434* (7029), 55–59.

(36) Campbell, C. J.; Baker, E.; Fialkowski, M.; Bitner, A.; Smoukov, S. K.; Grzybowski, B. A. Self-Organization of Planar Microlenses by Periodic Precipitation. *J. Appl. Phys.* **2005**, *97* (12), 126102.

(37) Bishop, K. J. M.; Fiałkowski, M.; Grzybowski, B. A. Micropatterning Chemical Oscillations: Waves, Autofocusing, and Symmetry Breaking. *J. Am. Chem. Soc.* **2005**, *127* (45), 15943–15948.

(38) Bishop, K. J. M.; Gray, T. P.; Fialkowski, M.; Grzybowski, B. A. Microchameleons: Nonlinear Chemical Microsystems for Amplification and Sensing. *Chaos* **2006**, *16* (3), 37102.

(39) Walliser, R. M.; Boudoire, F.; Orosz, E.; Tóth, R.; Braun, A.; Constable, E. C.; Rácz, Z.; Lagzi, I. Growth of Nanoparticles and Microparticles by Controlled Reaction-Diffusion Processes. *Langmuir* **2015**, *31* (5), 1828–1834.

(40) Nabika, H.; Sato, M.; Unoura, K. Liesegang Patterns Engineered by a Chemical Reaction Assisted by Complex Formation. *Langmuir* **2014**, *30* (18), 5047–5051.

(41) Bensemann, I. T.; Fialkowski, M.; Grzybowski, B. A. Wet Stamping of Microscale Periodic Precipitation Patterns. *J. Phys. Chem. B* **2005**, *109* (7), 2774–2778.

(42) Tolan, M. *X-Ray Scattering from Soft-Matter Thin Films - Materials Science and Basic Research*; Springer: Berlin, 1999.

(43) Sakurai, K.; Iida, A. Fourier Analysis of Interference Structure in X-Ray Specular Reflection from Thin Films. *Japanese Journal of Applied Physics*. 1992, pp L113–L115.

(44) Als-Nielsen, J.; McMorrow, D. *Elements of Modern X-Ray Physics: Second Edition*; John Wiley and Sons: West Sussex, U.K., 2011.

(45) Despotopoulou, M. M.; Miller, R. D.; Rabolt, J. F.; Frank, C. W. Polymer Chain Organization and Orientation in Ultrathin Films: A Spectroscopic Investigation. *J. Polym. Sci. Part B-Polymer Phys.* **1996**, *34*, 2335–2349.

(46) Domke, J.; Radmacher, M. Measuring the Elastic Properties of Thin Polymer Films with the Atomic Force Microscope. *Langmuir* **1998**, *14* (12), 3320–3325.

(47) Fialkowski, M.; Campbell, C. J.; Bensemann, I. T.; Grzybowski, B. A. Absorption of Water by Thin, Ionic Films of Gelatin. *Langmuir* **2004**, *20* (9), 3513–3516.

(48) Klajn, R.; Fialkowski, M.; Bensemann, I. T.; Bitner, A.; Campbell, C. J.; Bishop, K.; Smoukov, S.; Grzybowski, B. A. Multicolour Micropatterning of Thin Films of Dry Gels. *Nat. Mater.* **2004**, *3* (10), 729–735.

(49) Campbell, C. J.; Smoukov, S. K.; Bishop, K. J. M.; Grzybowski, B. A. Reactive Surface Micropatterning by Wet Stamping. *Langmuir* **2005**, *21* (7), 2637–2640.

(50) Hantz, P. Pattern Formation in a New Class of Precipitation Reactions, University of Geneva, 2006.

(51) Ostwald, W. A-Linien von R. E. Liesegang (Review). *Z. phys. Chem.* **1897**, *23*, 356.

(52) Wagner, C. Mathematical Analysis of the Formation of Periodic Precipitations. *J. Colloid Sci.* **1950**, *5* (1), 85–97.

(53) Prager, S. Periodic Precipitation. *J. Chem. Phys.* **1956**, *25* (2), 279–283.

(54) Kai, S. Measurements of Temporal and Spatial Sequences of Events in Periodic Precipitation Processes. *J. Chem. Phys.* **1982**, *76* (3), 1392–1406.

(55) Mueller, S. C.; Kai, S.; Ross, J. Periodic Precipitation Patterns in the Presence of Concentration Gradients. 1. Dependence on Ion Product and Concentration Difference. *J. Phys. Chem.* **1982**, *86* (20), 4078–4087.

(56) Flicker, M.; Ross, J. Mechanism of Chemical Instability for Periodic Precipitation Phenomena. *J. Chem. Phys.* **1974**, *60* (9), 3458–3465.

(57) Sultan, R.; Ortoleva, P. Periodic and Aperiodic Macroscopic Patterning in Two Precipitate Post-Nucleation Systems. *Phys. D Nonlinear Phenom.* **1993**, *63* (1–2), 202–212.

(58) Feinn, D.; Ortoleva, P.; Scalf, W.; Schmidt, S.; Wolff, M. Spontaneous Pattern Formation in Precipitating Systems. *J. Chem. Phys.* **1978**, *69* (1), 27–39.

(59) Feeney, R.; Schmidt, S. L.; Strickholm, P.; Chadam, J.; P. Ortoleva. Periodic Precipitation and Coarsening Waves: Applications of the Competitive Particle Growth Model. *J. Chem. Phys.* **1983**, *78* (3), 1293–1311.

(60) Antal, T.; Droz, M.; Magnin, J.; Rácz, Z. Formation of Liesegang Patterns: A Spinodal Decomposition Scenario. *Phys. Rev. Lett.* **1999**, *83* (15), 2880–2883.

(61) Droz, M. Recent Theoretical Developments on the Formation of Liesegang Patterns. *J. Stat. Phys.* **2000**, *101* (1), 509–519.

(62) Xing, Q.; Yates, K.; Vogt, C.; Qian, Z.; Frost, M. C.; Zhao, F. Increasing Mechanical Strength of Gelatin Hydrogels by Divalent Metal Ion Removal. *Sci. Rep.* **2014**, *4*, 4706.

(63) Jiang, J. Supporting Experiment. 2016.

(64) Njuguna, J.; Pielichowski, K. Polymer Nanocomposites for Aerospace Applications: Properties. *Adv. Eng. Mater.* **2003**, *5* (11), 769–778.

(65) Bekyarova, E.; Thostenson, E. T.; Yu, A.; Kim, H.; Gao, J.; Tang, J.; Hahn, H. T.; Chou, T.-W.; Itkis, M. E.; Haddon, R. C. Multiscale Carbon Nanotube-Carbon Fiber Reinforcement for Advanced Epoxy Composites. *Langmuir* **2007**, *23* (7), 3970–3974.

(66) Chen, B.; Guizar-Sicairos, M.; Xiong, G.; Shemilt, L.; Diaz, A.; Nutter, J.; Burdet, N.; Huo, S.; Mancuso, J.; Monteith, A.; et al. Three-Dimensional Structure Analysis and Percolation Properties of a Barrier Marine Coating. *Sci. Rep.* **2013**, *3*, 1177.

(67) Li, Q.; Guo, Y.; Li, W.; Qiu, S.; Zhu, C.; Wei, X.; Chen, M.; Liu, C.; Liao, S.; Gong, Y.; et al. Ultrahigh Thermal Conductivity of Assembled Aligned Multilayer Graphene/Epoxy Composite. *Chem. Mater.* **2014**, *26* (15), 4459–4465.

(68) Zhang, C.; Hankett, J.; Chen, Z. Molecular Level Understanding of Adhesion Mechanisms at the Epoxy/polymer Interfaces. *ACS Appl. Mater. Interfaces* **2012**, *4* (7), 3730–3737.

(69) Björck, M.; Andersson, G. GenX： an Extensible X-Ray Reflectivity Refinement Program Utilizing Differential Evolution. *J. Appl. Cryst.* **2007**, *40*, 1174–1178.

(70) Herman, G. T. *Fundamentals of Computerized Tomography: Image Reconstruction from Projections*, 2nd ed.; Springer: London, 2009.

(71) Kak, A. C.; Slaney, M. *Principles of Computerized Tomographic Imaging*; IEEE Press: New York, 1999.

(72) Natterer, F. *The Mathematics of Computerized Tomography*; Society for Industrial and Applied Mathematics: Philadelphia, 2001.

(73) Aster, R. C.; Borchers, B.; Thurber, C. H. *Parameter Estimation and Inverse Problems*; Elsevier: Oxford, U.K., 2011; Vol. 90.

(74) Sakurai, K.; Mizusawa, M.; Ishii, M.; Kobayashi, S.; Imai, Y. Instrumentation for X-Ray Reflectivity in Micro Area: Present Status and Future Outlook. *J. Phys. Conf. Ser.* **2007**, *83*, 12001.

(75) Fenter, P.; Lee, S. S.; Zhang, Z.; Sturchio, N. C. In Situ Imaging of Orthoclase – Aqueous Solution Interfaces with X-Ray Reflection Interface Microscopy. *J. Appl. Phys.* **2011**, *110*, 102211.

(76) Fenter, P.; Park, C.; Kohli, V.; Zhang, Z. Image Contrast in X-Ray Reflection Interface Microscopy: Comparison of Data with Model Calculations and Simulations Research Papers. *J. Synchrotron Radiat.* **2008**, *15*, 558–571.

(77) Highland, M. J.; Fenter, P. Full-Field X-Ray Reflection Microscopy of Epitaxial Research Papers. *J. Synchrotron Radiat.* **2014**, *21*, 1252–1261.

(78) Zhu, C.; Harder, R.; Diaz, A.; Komanicky, V.; Barbour, A.; Xu, R.; Huang, X.; Pierce, M. S.; Menzel, A.; You, H.; et al. Ptychographic X-Ray Imaging of Surfaces on Crystal Truncation Rod. *Appl. Phys. Lett.* **2015**, *106*, 101604.

(79) Innis-Samson, V. A.; Mizusawa, M.; Sakurai, K. X-Ray Reflection Tomography: A New Tool for Surface Imaging. *Anal. Chem.* **2011**, *83* (20), 7600–7602.

(80) Innis-Samson, V. A.; Mizusawa, M.; Sakurai, K. X-Ray Reflection Tomography Reconstruction for Surface Imaging: Simulation versus Experiment. *Adv. X-Ray Chem. Anal. Jpn.* **2012**, *43*, 391–400.

(81) Jiang, J.; Sakurai, K. X-Ray Reflectivity Imager with 15 W Power X-Ray Source. *Rev. Sci. Instrum.* **2016**, *87* (9), 93709.

(82) Ando, M.; Satow, Y.; Kawata, H.; Ishikawa, T.; Spieker, P.; Suzuki, S. Design of Beamline 14 for the PF Vertical Wiggler and Its Operation. *Nucl. Instruments Methods Phys. Res.* **1986**, *A246*, 144–148.

(83) Gann, E.; Watson, A.; Tumbleston, J. R.; Cochran, J.; Yan, H.; Wang, C.; Seok, J.; Chabinyc, M.; Ade, H. Topographic Measurement of Buried Thin-Film Interfaces Using a Grazing Resonant Soft X-Ray Scattering Technique. *Phys. Rev. B* **2014**, *90*, 245421.

(84) Jiang, J.; Hirano, K.; Sakurai, K. Micro-Imaging of Buried Layers and Interfaces in Ultrathin Films by X-Ray Reflectivity. *J. Appl. Phys.* **2016**, *120* (11), 115301.

(85) Jiang, J.; Sakurai, K. X-Ray Reflectivity Imager with 15 W Power X-Ray Source. *Rev. Sci. Instrum.* **2016**, *87* (9), 93709.

(86) Strang, G.; Borre, K. Linear Algebra, Geodesy, and Gps. *Linear Algebra, Geodesy, and GPS*. 1997, p 624.

(87) Hansen, P. C. Rank-Deficient and Discrete Ill-Posed Problems: Numerical Aspects of Linear Inversion. In *Society for Industrial and Applied Mathematics*; Society for Industrial and Applied Mathematics: Philadelphia, 1997; pp 19–66.

(88) Hansen, P. C. Discrete Inverse Problems: Insight and Algorithms. In *Fundamentals of Algorithms*; Society for Industrial and Applied Mathematics: Philadelphia, 2010; pp 53–79.

(89) Ice, G. E.; Budai, J. D.; Pang, J. W. L. The Race to X-Ray Microbeam and Nanobeam Science. *Science (80-. ).* **2011**, *334* (6060), 1234–1239.

(90) Stangl, J.; Mocuta, C.; Chamard, V.; Carbone, D. *Nanobeam X-Ray Scattering*; WILEY-VCH: Weinheim, Germany, 2013.

(91) Jiang, J.; Sakurai, K. Micro-Imaging of Buried Layers and Interfaces in Ultrathin Films by X-Ray Reflectivity. *J. Appl. Phys.* **2016**, *120* (11), 115301.

(92) Sakurai, K.; Iida, A. Analysis of Specific Interfaces in Thin Films by X-Ray Fluorescence Using Interference Effect in X-Ray Total Reflection. In *Advances in X-Ray Analysis*; Plenum Press: New York, U.S., 1997; Vol. 39, pp 695–700.

# List of achievements

## 1. Publications

[1] **Jinxing Jiang**, Keiichi Hirano, and Kenji Sakurai, **Micro-imaging of buried layers and interfaces in ultrathin films by X-ray reflectivity**, Journal of Applied Physics 2016, 120, 115301. **[Featured Article]**

[2] **Jinxing Jiang** and Kenji Sakurai, **X-ray reflectivity imager with 15 W power X-ray source**, Review of Scientific Instruments 2016, 87, 093709.

[3] **Jinxing Jiang** and Kenji Sakurai, **Formation of ultrathin Liesegang patterns**, Langmuir 2016, 32, 9126−9134.

[4] **Jinxing Jiang**, Keiichi Hirano, and Kenji Sakurai, **Interface sensitive imaging by image-reconstruction aided X-ray reflectivity technique**. [submitted to Journal of Applied Crystallography]

## 2. Conference presentations

[1] **Poster Presentations:** Visualization of inhomogeneous layers and interfaces in ultrathin films by X-ray reflectivity**;** Structure of self-organized periodic silver dichromate rings in ultrathin film, The 13th Biennial Conference on High Resolution X-ray Diffraction and Imaging, Masaryk University, Brno, Czech Republic, September 2016.

[2] **Oral Presentation:** Visualization of surfaces and buried interfaces: Tomographic imaging based on X-ray reflectivity; **Poster Presentation:** Formation and observation of periodic ring structures in ultrathin films, The 72nd Japanese Society of Microscopy Meeting, Sendai International Center, Sendai, June 2016.

[3] **Oral Presentation:** Visualization of buried layers and interfaces in thin films, Japan-Thailand Joint Meeting on Functional Nanomaterials, Nanotec Auditorium, Bangkok, Thailand, May 2016.

[4] **Oral / Poster Presentation:** Liesegang Pattern engineered in ultrathin films, The 96th Chemical Society of Japan Annual Meeting, Doshisha University, Kyoto, Japan, March, 2016.

[5] **Poster Presentation:** 3D imaging of layered thin films by TOF neutron reflectivity, Quantum Beam Science Festa 2015. International Congress Center Epochal Tsukuba, Japan, March 2016.

[6] **Oral Presentation:** Imaging of surfaces and buried interfaces in layered thin films by X-ray reflectivity, The 29th Japan Society for Synchrotron Radiation Conference, University of Tokyo, Kashiwanoha campus, January. 2016.

[7] **Poster Presentation:** Non-destructive imaging of surfaces and buried interfaces of thin films by X-ray reflection tomography, The 51th X-ray Analysis Conference, Himeji, Japan, October, 2015.

[8] **Poster Presentation:** Instrumentation of X-ray reflection tomography technique - towards visualization of

buried inhomogeneous interfaces of layered thin films. The 71th Japanese Society of Microscopy Meeting, Kyoto International Conference Center, Kyoto, Japan, May, 2015.

[9] **Oral Presentation:** X-ray Tomographic Imaging of Surfaces and Buried Interfaces. The 50th X-ray Analysis Conference. Tohoku University, Sendai, Japan, October, 2014.

[10] **Oral Presentation:** Tomographic Micro-Imaging of Buried Layers and Interfaces with 15W X-ray Power. The 75th JSAP Autumn Meeting. Hokkaido University, Sapporo. Japan, September 2014.

## 3. Awards

September 8th, 2016, the Student Poster Award (IUCr Journals Poster Prize) at the 13th Biennial Conference on High-Resolution X-Ray Diffraction and Imaging.

## 4. Press release

ナノ粒子、同心円状に配列

物材機構、薄膜の内部に

物質・材料研究機構の桜井健次グループリーダーらは、薄膜の内部に微細な粒子を同心円状に配列する技術を開発した。ナノレベルの微小領域で配列を制御する技術として、光学デバイスや電子・磁気の機能を使ったセンサー部品などの開発に応用できるという。

ゼラチンのゼリーに金属イオンを含む水溶液を滴下すると自然に拡散し、ゼリー中の物質と反応して同心円状に析出する。19世紀から知られていた現象だが、従来の研究では一定以上の厚みのあるゼリー状のシートにしか適用できなかった。

研究グループは周囲の温度や水蒸気量を工夫し、水溶液に含まれる微細な粒子がシート内の空間を適度な速さで拡散する条件を見いだした。0・1㎛（㎛は100万分の1）以下の薄いシート内でも粒子を同心円状に並べることが可能になり、クロム酸銀と呼ぶ物質を析出させることに成功した。

成果は米国の論文誌に掲載された。

微細な粒子を同心円状に配列する（物材機構提供）

再転載禁止

日経産業新聞 8面

2016年9月14日



超薄膜内でナノ粒子を同心円パターン状に配列

EE Times Japan 9月8日(木)13時34分配信

■光学デバイスや電子／磁気センサー部品などに応用

物質・材料研究機構（NIMS）先端材料解析研究拠点高輝度光解析グループの桜井健次グループリーダーと蒋金星ジュニア研究員は2016年9月、超薄ゼリーシート内でナノ粒子を同心円パターン状に配列させる技術を開発したと発表した。研究成果は光学デバイスやセンサー部品などへの応用が期待される。

桜井氏らの研究チームは、0.1μm以下という極めて薄いゼリーシート内に、リーゼガング環のナノ粒子同心円パターンを作成することに成功した 出典：物質・材料研究機構

超薄ゼリーシート内にナノ粒子のパターンを形成させるには、滴下した液滴中の物質が超薄ゼリーシートの狭い空間の中を、適切な速度で拡散させることが必要だ。研究チームは、作業時の温度環境と水蒸気量を適切に制御することで、0.1μm以下という極めて薄い膜内に、リーゼガング環のナノ粒子同心円パターンを作成することに成功した。これまでは、少なくとも数ミクロン程度の膜厚がないと、リーゼガング環を作製することは難しいといわれてきた。

研究チームは、精密に温度制御ができる冷蔵庫を用い、低温環境で研究を行った。その中に試料を入れておく密閉容器があり、容器内の水蒸気量も制御できるようにした。ゼラチンのゼリー表面は温度によって性質が変化する。低温環境では適度の撥水性を維持しており、滴下した液滴の中央から拡散していく物質の量を、適